Forschungszentrum Karlsruhe
in der Helmholtz-Gemeinschaft

Wissenschaftliche Berichte

FZKA 7496

Tokamak Code TOKES
Models and Implementation

I. S. Landman

Institut für Hochleistungsimpuls- und Mikrowellentechnik
Programm FUSION
Association EURATOM/Forschungszentrum Karlsruhe

Tokamak Code TOKES
Models and Implementation

I.S. Landman

Institut für Hochleistungsimpuls- und Mikrowellentechnik

Programm Fusion

Association EURATOM-FZK

Abstract

During a few past years the code TOKES was developed aiming at an integrated simulation of plasma equilibrium states and surface processes in tokamaks. The code calculates multi-fluid plasma processes in the core plasma and the scrape-off layer (SOL), and atomic processes at the vessel surface and in the vessel volume, by a sequence of time steps for the whole discharge. The dynamics of the magnetic field and the currents in the plasma and the poloidal field coils are accounted for. The models include fuelling by spreading cold atoms in the confined plasma volume and heating by neutral beams, transport of radiation and neutrons in the whole vessel and the hot plasma in the core, and plasma fluxes through the separatrix or the limiter magnetic surface into SOL towards the wall. Surface response to the load such as sputtering and vaporization are considered, and also the propagation of emitted material atoms in the vessel and their ionization and charge-exchanges in SOL and the confined plasma.

At the current stage some components possibly represent only temporary solutions and may in future be further elaborated or even fully replaced with different models. Nevertheless, the code already offers a rather self-consistent approach of tokamak simulation for engineers and scientists with background knowledge of tokamak physics, and also a convenient user interface. Usually one simulation takes a few hours on a conventional personal computer and provides many data for a deep insight into tokamak operation.

So far there are several publications that shortly describe the features of TOKES and its capabilities of applications for the future tokamak ITER. However, the present TOKES needs validations against experimental results on existing big tokamaks; only then predictive simulations for ITER and the DEMO concept can gain confidence.

This document comprises the intermediate state of the code, including the physical and mathematical background of incorporated models and design details, in order to promote further elaboration and development of this tokamak simulator, and to provide detailed background material for referencing, including material not mentioned in the available publications.

Der Tokamak Code TOKES - Modelle und Implementation

Zusammenfassung

Seit ein paar Jahren wird das Rechenprogramm TOKES entwickelt mit dem Ziel einer integrierten Simulation von Plasmagleichgewichtzuständen und Oberflächenprozessen in Tokamaks. Der Code berechnet multifluidale Plasmaprozesse im Kernplasma und der Abschälschicht (SOL), und atomare Prozesse an den inneren Oberflächen und im Volumen des Vakuumbehälters mit einer Folge von Zeitschritten über die gesamte Entladung. Die Dynamik des Magnetfeldes und die Ströme im Plasma und den poloidalen Feldspulen sind berücksichtigt. Die Modelle beinhalten die Brennstoffnachfüllung durch Verteilen von kalten Atomen im eingeschlossenen Plasma und die Heizung durch Neutralteilcheninjektion, den Transport von Strahlung und Neutronen im gesamten Behälter und im heißen Kernplasma, und den Plasmaabfluss durch die Separatrix oder die letzte geschlossene Magnetoberfläche in das SOL und zu den Wänden. Reaktionen der Wandoberfläche auf diese Belastung, wie Verspritzen und Verdampfung, werden ebenso betrachtet wie auch die Propagation von emittierten Materialatomen im Vakuumbehälter und deren Ionisation und Ladungsaustauschprozesse im SOL und eingeschlossenen Plasma.

Gegenwärtig stellen einige Komponenten möglicherweise nur temporäre Lösungen dar und werden in Zukunft weiter ausgearbeitet oder auch durch andere Modelle ersetzt. Trotzdem bietet der Code bereits jetzt eine ziemliche selbst konsistente Methode zur Tokamaksimulation für Ingeneure und Wissenschaftler mit Hintergrundwissen in Tokamakphysik, und auch eine angemessene Benutzereingabe. Gewöhnlich benötigt eine Simulationsrechnung einige wenige Stunden auf einem konventionellen Rechner und liefert viele Daten für tiefere Einsichten in den Tokamakbetrieb.

Es existieren bislang mehrere Publikationen mit kurzen Beschreibungen der Eigenschaften von TOKES und seiner Anwendungsmöglichkeiten für den zukünftigen Tokamak ITER. Jedoch muss der gegenwärtig vorliegende TOKES gegen experimentelle Ergebnisse bei existierenden Tokamaks validiert werden; nur dann kann Zutrauen in Vorhersagen aus Rechnungen für ITER und dem DEMO Konzept entstehen.

Dieses Dokument umfasst den gegenwärtigen intermediären Zustand des Codes einschließlich der physikalischen und mathematischen Inhalte der Modelle und Details zum Codedesign, mit dem Ziel, die weitere Verbesserung und Entwicklung dieses Tokamaksimulators zu fördern, und ausführliches Hintergrundmaterial zur Referenzierung zu liefern, insbesondere solches, das in den vorhandene Publikationen nicht enthalten ist.

Contents

1. Introduction

Urgent necessity of a compact code that consistently reproduces tokamak behaviour naturally follows from the human need for abundant energy sources. Indeed, responding the demand, the parliaments worldwide increase investments in fusion research, which employs educated people. New engineers and scientific workers should at first learn and then further develop the complex technology of building thermonuclear reactors. So far, the most advanced fusion concept bases on the tokamak magnetic trap in which the hydrogen isotopes deuterium and tritium (DT) burn. The development of very efficient personal computers during the last two decades made possible to install a virtual tokamak on many working desks of the people involved in this constructive endeavour, in order to facilitate the search for design elaborations of real tokamaks. That would accelerate and consolidate the overall effort to overcome the energy problem.

One very important feature of such an integrated code that can really make it attractive for a creative person should be openness to the user. The code should not be a black box that offers buttons and menus only. It is necessary to provide a feeling that one can really penetrate into the models and, if not fully satisfied with some of them, contribute himself to their elaboration. This approach is aimed in the code TOKES, which this work is devoted to and therefore as much as are of TOKES details are described.

The concept of sharing tokamak code development is not new. For example with the code ASTRA Ref.[1], one pursued also the idea of creating a joint platform, at least in investigations of the confined tokamak plasma itself. The development of the code TOKES follows this way, too, trying to expand the modelling means for the whole tokamak vessel.

The abbreviation 'TOKES' means 'Tokamak Equilibrium (or Evolution) and Surface processes (or Stability)'. The toroidal symmetry is assumed, which TOKES models keep as a basic feature of tokamak principle. The code simulates plasma evolution in time t. The plasma stays in some slowly changing equilibrium with the confining magnetic field. The evolution of the confinement equilibrium occurs due to internal dissipative processes in the plasma, such as the diffusion across the field lines, and variations of external parameters, such as the DT inflow. The intermediate states are described with diverse functions of cylindrical coordinates, r and z, where z is the coordinate along the axis of toroidal symmetry and r the distance from the z-axis. Another important frame in TOKES is magnetic flux coordinates. At

$t \rightarrow \infty$ this two-dimensional system may eventually reach a steady equilibrium state. Such final state is not essential, and TOKES can simulate in many details non-steady tokamak processes. The simulation involves dynamical changes of plasma shape and actual electric currents as in plasma as in external coils of poloidal magnetic field (PF coils) that control the stability of the whole configuration in respect to toroidally symmetric modes.

Describing the virtual tokamak of TOKES, the lexicon of real physical processes can naturally be used. In this context, TOKES steadily 'creates' hot DT plasma by fuelling a confinement region (the core) inside the tokamak vessel with DT atoms. The fusion reaction produces helium ions, fast neutrons, and the heat. Impurities from the vessel wall contaminate the plasma. The code simulates impurity ions in the whole vessel as it does for the main plasma components, with a common multi-fluid plasma model for all species. The plasma diffuses across nested magnetic surfaces of the trap to the periphery of the core. Then it passes a narrow scrape-off layer (SOL) that is the core's shell, and dumps along magnetic field lines onto vessel walls. The wall surface absorbs also the electromagnetic radiation from the plasma and the neutrons as well. The surface responses to the impact, backscattering impacting ions and emitting sputtered atoms and, if the load is very large, the vapour of wall material. The erosion products, which are emitted atoms of wall materials, freely propagate in the vessel before having ionized in SOL and the core. The code calculates the evolution until reaching a steady state or a collapse of the plasma.

In the manuscript TOKES models of these processes are explained, with the hope that this can help the reader also to develop own insight. Perhaps during the reading, one will soon challenge some implemented ideas and solutions. Okay, that would be the best news that somebody tries improving the concept. Anyway, the reader is assumed to be well educated as physicist and numerical mathematician, and familiar with basic equations and formulas of plasma physics.

This detailed description of many underground features may emerge questions and critique that can be answered with taking responsibility for possible errors by me only. As the developer of the code during the period described in this technical document, I gratefully acknowledge contributions of my colleagues for the development of the concept itself. The very important influence came from Dr. G. Janeschitz, who was the initiator and enthusiastic supporter of this work. Dr. S. Pestchanyi has improved my work due to numerous fruitful discussions about particular models. Dr. R. Kochergov contributed to the validation of TOKES' algorithms of plasma diffusion. Furthermore, I used in some part the algorithms of the code FOREV-2D, the predecessor of TOKES.

The purpose of this work is to give the insight into the code itself. The whole text consists of the sections that deal with various models and features of this integrated two-dimensional tokamak code. Up to date, there are several our publications (the first Ref.[2] and last one Ref.[3]) that shortly describe the features of TOKES available at that times and reveal its capabilities of applications for the future tokamak ITER. In order to avoid too bulky manuscript, in deducing model equations many details of mathematical manipulations are omitted. However, if the reader needs deeper interpretation of basic material, detailed descriptions of analytical transformations are available in a draft document that may be transferred as a part of code's source files, which are written with the programming language Delphi. The formulas of magneto-hydrodynamics (MHD), radiation transport and gyro-motion models intended for the implementation are deduced there 'from scratch', because it is necessary that we are accustomed of the origins of main formulas.

It can be so that the references are missed for the investigations where similar approaches have been earlier developed. In such cases it should be clear that I do not challenge what was already done, and the calculations or descriptions aim only for *in situ* substantiations of particular details of TOKES. Finally it is to mention that the extensive parameters (such as volumes and particles numbers) are reduced to 1 radian of the toroidal angle ζ (so that in the internal statements of the code, e.g. plasma volume means the volume divided by 2π). The Gaussian system of units (CGS) is internally used, but the input and output data of TOKES are provided in the unit system SI (and plasma temperatures in eV).

Part I   MHD plasma model

2. Toroidally symmetric magnetic and electric fields

The base frame of TOKES is the cylindrical coordinates $\mathbf{r} = (r, z, \zeta)$ with the axis z the symmetry axis, r the distance from the axis z, and ζ the toroidal angle around the axis z ($0 \leq \zeta < 2\pi$) (see Fig.1). In toroidally symmetric configurations, any scalar function $f(\mathbf{r})$ describing the system does not depend on ζ: $\partial f / \partial \zeta = 0$. The plasma in a tokamak cannot fast escape due to toroidal magnetic surfaces that are nested around a circular 'magnetic axis' situated at some position $\mathbf{p}_0 = (r_0, z_0)$ of the poloidal cross-section Ref.[4].

We assume that the toroidal rotation of plasma occurs with negligible velocity. In this case plasma equilibrium states are described with the equation:

$$\nabla p = \frac{1}{c} \mathbf{J} \times \mathbf{B} \tag{2.1}$$
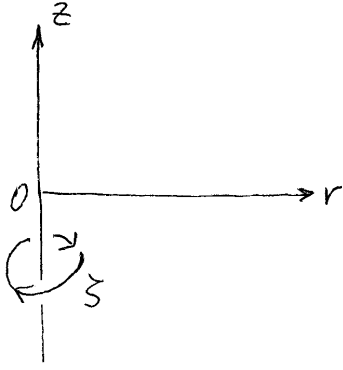
Fig.2.1 The toroidal coordinates

Given the plasma pressure p and the magnetic induction $\mathbf{B}$, this is the equation for the electric current density $\mathbf{J}$. For slow processes, such as collisional plasma transport across the magnetic field (diffusion and thermal conductivity) the configuration evolves temporarily through a sequence of equilibriums satisfying Eq.(1).

The magnetic field is described with the Maxwell's equations:

$$\nabla \mathbf{B} = 0, \qquad \nabla \times \mathbf{B} = \frac{4\pi}{c} \mathbf{J} \tag{2.2}$$

Unless the plasma transport across the magnetic surfaces is involved, the pressure as a function of r and z can be chosen rather arbitrarily however the choice of p is limited by the fact that from Eq.(1) the conditions follow

$$\mathbf{B} \nabla p = 0, \qquad \mathbf{J} \nabla p = 0 \tag{2.3}$$

Thus, p keeps constant along the magnetic field lines and along the current lines. We assume each magnetic surface to correspond to a magnetic field line that covers the whole surface by

winding. The magnetic surfaces and current surfaces are identical and p is constant at each such surface (i.e. p is a surface function).

To describe $\mathbf{B} = (B_r, B_z, B_\zeta)$ meeting Eq.(2), B_r and B_z are expressed in terms of a one-component vector potential $\mathbf{A} = (0, 0, A_\zeta(r,z))$ as $(B_r, B_z, 0) = \nabla \times \mathbf{A}$. The r- and z-components give the poloidal field. Introducing then the function $w = rA_\zeta$ (the poloidal magnetic flux divided by 2π) we obtain:

$$B_r = \frac{1}{r}\frac{\partial w}{\partial z}, \qquad\qquad B_z = -\frac{1}{r}\frac{\partial w}{\partial r} \qquad\qquad (2.4)$$

Similarly, J_r and J_z are expressed in accordance with Eq.(2) using the function $\omega = rB_\zeta$:

$$J_r = \frac{c}{4\pi}\frac{1}{r}\frac{\partial \omega}{\partial z}, \qquad\qquad J_z = -\frac{c}{4\pi}\frac{1}{r}\frac{\partial \omega}{\partial r} \qquad\qquad (2.5)$$

Thus, the toroidal field B_ζ plays for $\mathbf{J}$ the role of a vector potential that provides $\nabla \mathbf{J} = 0$. From Eq.(1) and Eq.(2) the identities $\mathbf{B}\nabla w \equiv 0$ and $\mathbf{J}\nabla\omega = 0$ follow, so that $w(r,z)$ and $\omega(r,z)$ are surface functions.

From the above equations, we obtain the toroidal current density:

$$J_\zeta = \frac{c}{r}\frac{d}{dw}\left(\frac{\omega^2}{8\pi}\right) + cr\frac{dp}{dw} \qquad\qquad (2.6)$$

Then from the ζ–component of Eq.(2)$_2$ the Grad-Shafranov equation follows Ref.[5]:

$$r\frac{\partial}{\partial r}\left(\frac{1}{r}\frac{\partial w}{\partial r}\right) + \frac{\partial^2 w}{\partial z^2} = -\frac{1}{2}\frac{d\omega^2}{dw} - 4\pi r^2\frac{dp}{dw} \qquad\qquad (2.7)$$

Eq.(7) describes the poloidal magnetic field at given functions $\omega(w)$ and $p(w)$. The obtaining of ω and p needs additional equations (they are deduced in Sec.5).

In TOKES the poloidal magnetic field is calculated using the Green function $G(\mathbf{p},\mathbf{P})$ of the differential elliptic operator in the left side of Eq.(7):

$$G(\mathbf{p};\mathbf{P}) = 4\frac{\sqrt{rR}}{ck}\left(\left(1 - \frac{k^2}{2}\right)K(k) - E(k)\right), \qquad \mathbf{P} = (R,Z) \qquad\qquad (2.8)$$

The function G gives the magnetic flux at a position $\mathbf{p} = (r,z)$ for unit current in a circular ring of a radius R centred on the z-axis at $z = Z$ and oriented perpendicularly to the z-axis Ref.[6]. The parameter k is given by

$$k^2 = \frac{4rR}{(r+R)^2 + (z-Z)^2} \qquad\qquad (2.9)$$

The functions $K(k)$ and $E(k)$ are the complete elliptic integrals. Given toroidal currents I_n flowing inside the coils n of external poloidal magnetic field which are situated at some

positions $\mathbf{P}_n = (R_n, Z_n)$ ($n = 0..N-1$), as well as the current density $J_\zeta(\mathbf{p})$ in the plasma, the poloidal magnetic flux is calculated as

$$w(\mathbf{p}) = \sum_n I_n G(\mathbf{p}, \mathbf{P}_n) + \int_\Omega J_\zeta(\mathbf{p}') G(\mathbf{p}, \mathbf{p}') dr' dz' \tag{2.10}$$

The cross-transport of plasma is described with the magnetic flux coordinates (x,y) on the poloidal plane, thus r and z depend on x and y. Here x is some surface function, e.g. $x \equiv w - w(\mathbf{p}_0)$, and y a periodical poloidal coordinate that varies as $0 \leq y \leq Y$ at $x = $ const (e.g. y is a poloidal angle with $Y = 2\pi$). The magnetic axis can correspond to $x = 0$, and the plasma boundary to some $x = X$. The magnetic metrics is defined by the contravariant vectors $\mathbf{e}_1 = (\partial r/\partial x, \partial z/\partial x)$ and $\mathbf{e}_2 = (\partial r/\partial y, \partial z/\partial y)$. The Jacoby's poloidal coefficient g is given by:

$$\sqrt{g} = \frac{\partial r}{\partial x}\frac{\partial z}{\partial y} - \frac{\partial z}{\partial x}\frac{\partial r}{\partial y}, \qquad g_{12}^2 = g_{11}g_{22} - g \tag{2.11}$$

The covariant metric tensor components are $g_{11} = |\mathbf{e}_1|^2$, $g_{22} = |\mathbf{e}_2|^2$ and $g_{12} = \mathbf{e}_1\mathbf{e}_2$ (and the Lame coefficients are $h_x = |\mathbf{e}_1|$ and $h_y = |\mathbf{e}_2|$).

The electric field $\mathbf{E}$ is described with the Maxwell's equations:

$$\nabla\mathbf{E} = 4\pi\rho \tag{2.12}$$

$$\frac{\partial \mathbf{B}}{\partial t} + c\nabla\times\mathbf{E} = 0 \tag{2.13}$$

In accordance with the Kelvin-Helmholtz theorem the electric field splits into its vortex and potential parts: $\mathbf{E} = \mathbf{E}_v - \nabla\varphi$. As we have the equalities $\nabla\mathbf{E}_v = 0$ and $\nabla\times(\nabla\varphi) \equiv 0$, Eq.(12) describes the electric potential φ formed by the electric charge density ρ, and Eq.(13) the vortex electric field $\mathbf{E}_v$ that appears due to evolution of magnetic field $\mathbf{B}$ in the time t.

The field $\mathbf{E}_v$ splits into its poloidal- $\mathbf{E}_{vp}$ and toroidal $\mathbf{E}_{v\zeta}$ components: $\mathbf{E}_v = \mathbf{E}_{vp} + \mathbf{E}_{v\zeta}$. Accordingly, in the vector equation Eq.(13) $\partial B_\zeta/\partial t$ generates $\mathbf{E}_{vp}$ and $\partial \mathbf{B}_p/\partial t$ generates $\mathbf{E}_{v\zeta}$. As $(\nabla\varphi)_\zeta = 0$, we have $\mathbf{E}_{v\zeta} = \mathbf{E}_\zeta$. As the poloidal magnetic field $\mathbf{B}_p$ is described with the vector potential $\mathbf{A} = (0,0,A_\zeta)$, the substitution $\mathbf{B}_p = \nabla\times\mathbf{A}$ into Eq.(13) gives

$$\frac{\partial \mathbf{A}}{\partial t} + c\mathbf{E}_\zeta = \nabla U \tag{2.14}$$

By definition of $\mathbf{A}$ and $\mathbf{E}_\zeta$, Eq.(14) has only a toroidal component therefore U is arbitrary scalar function: $U(t,\zeta)$. This function can be multi-valued provided that ∇U remains single-valued, which restricts U by a linear form in respect to ζ: $U = -\zeta\phi(t)$. The substitution $A_\zeta = w/r$ yields

$$\frac{\partial w}{\partial t} + crE_\zeta = -\phi(t) \tag{2.15}$$

12

The function $\phi(t)$ is proportional to the 'loop voltage' of tokamak transformer $U_0 = 2\pi\phi/c$.

Eq.(13) and Eq.(15) are transformed to moving magnetic flux coordinates described with some functions $r = r(t,x,y)$ and $z = z(t,x,y)$. The coordinates move with a local velocity $\mathbf{u} = (u_r,u_z,u_\zeta) = (\partial r/\partial t, \partial z/\partial t, 0)$ in the poloidal plane, where the time derivatives at fixed x and y are implied. For any scalar f the transformation of time derivative reads:

$$\left.\frac{\partial f}{\partial t}\right|_{rz=\text{const}} = \left.\frac{\partial f}{\partial t}\right|_{xy=\text{const}} - \mathbf{u}\nabla f \tag{2.16}$$

It is convenient to change also the field $\mathbf{E}$ in the moving frame, and the new field $\mathbf{E}'$ reads

$$\mathbf{E} = \mathbf{E}' + \frac{1}{c}\mathbf{B}\times\mathbf{u} \tag{2.17}$$

Introducing the relative velocity $\mathbf{v} = \mathbf{V} - \mathbf{u}$ the equations are changed as

$$\frac{\partial w}{\partial t} + crE'_\zeta = -\phi(t) \tag{2.18}$$

$$\frac{\partial B_\zeta}{\partial t} - ((\mathbf{B}\nabla)\mathbf{u})_\zeta + B_\zeta(\nabla\mathbf{u}) + \frac{c}{\sqrt{g}}\left(\frac{\partial E'_2}{\partial x} - \frac{\partial E'_1}{\partial y}\right) = 0 \tag{2.19}$$

Using a standard formula, $\nabla\mathbf{u}$ of Eq.(19) can be reduced as

$$\nabla\mathbf{u} = \frac{1}{r\sqrt{g}}\frac{\partial}{\partial t}\left(r\sqrt{g}\right) \tag{2.20}$$

To get the operator $((\mathbf{B}\nabla)\mathbf{u})_\zeta$ of Eq.(19) we are using the analogy with the operator $(\mathbf{v}\nabla)\mathbf{v}$ that appears in fluid mechanics in the Euler's equation for the fluid velocity $\mathbf{v}$. The ζ-component of $(\mathbf{v}\nabla)\mathbf{v}$ describes the Coriolis' acceleration: $((\mathbf{v}\nabla)\mathbf{v})_\zeta = v_\zeta v_r/r$. Therefore the equality $((\mathbf{B}\nabla)\mathbf{u})_\zeta = B_\zeta u_r/r$ follows. Finally Eq.(19) acquires the form:

$$\frac{\partial}{\partial t}\left(B_\zeta\sqrt{g}\right) + c\frac{\partial E'_2}{\partial x} - c\frac{\partial E'_1}{\partial y} = 0 \tag{2.21}$$

3. MHD model for multi-fluid plasma

In substances the electric field causes electric currents and thus according to Eq.$(2.2)_2$ influences the magnetic field, generally in complex ways. In TOKES a simplified magneto-hydrodynamic approach for tokamak plasma is implemented, basing on Ref.[7]

The quasineutrality condition $\rho = \rho_{\text{ion}} - \rho_{\text{eln}} = 0$ appears as a consequence of large ion- and electron charge densities, ρ_{ion} and ρ_{eln} respectively, when $\nabla\mathbf{E}$ in Eq.(2.12) is a small term.

13

Therefore the equality $\rho_{ion} \approx \rho_{eln}$ (the quasineutrality equation) replaces the Maxwell's equation. The plasma contains different ions specified with the indices m (atom isotope index) and z (ion charge state). The species density n_m and electron density n_e are the sums over the ion densities n_{mz}:

$$n_m = \sum_z n_{mz} , \qquad\qquad n_e = \sum_{mz} z n_{mz} \qquad\qquad (3.1)$$

The densities and the temperatures are assumed to be some surface functions: $n_g(t,x)$ and $T_g(t,x)$ ($g = e,mz$); $T_{mz} \equiv T_m$ is assumed the same for different z. The plasma pressure $p = \sum_g p_g$ accumulates the partial pressures $p_g = n_g T_g$ of plasma components. Averaged and 'mean' charges are $z_m = (1/n_m)\sum_z z n_{mz}$ and $<z_m> = (1/n_e)\sum_z z^2 n_{mz}$, respectively.

The equations of evolution of these fluids moving with the velocities $\mathbf{V}_g(t,x,y)$ read:

$$\frac{\partial n_g}{\partial t} + \nabla\left(n_g \mathbf{V}_g\right) = s_g , \qquad\qquad \nabla p_g = \mathbf{f}_g \qquad\qquad (3.2)$$

$$\frac{\partial}{\partial t}\left(\frac{3}{2} n_g T_g\right) + \nabla\left(\frac{3}{2} T_g n_g \mathbf{V}_g\right) + p_g \nabla \mathbf{V}_g = Q_g \qquad\qquad (3.3)$$

In Eq.(2)$_2$ we omitted the contributions of the inertial term $m_g n_g d\mathbf{V}_g/dt$ and the viscosity (m_g is the particle mass, don't confuse masses with the atom kind index m and the Jacoby's coefficient $\sqrt{g}$ with the gas index g). The terms s_g, $\mathbf{f}_g$, and Q_g describe the processes caused by interactions of the species g with the fields $\mathbf{B}$ and $\mathbf{E}$, with the other species, and due to the external influences. The term s_g is the rate of the change of n_g due to conversions from the other species including the ionizations of neutral atoms coming into the plasma. $\mathbf{f}_g$ is the force applied to the unit volume of the gas g, and Q_g is the energy density deposition into the gas g. The interaction of a species g with the magnetic field is described by the Lorentz force $\mathbf{f}_{Lg} = \mathbf{J}_g \times \mathbf{B}/c$, with $\mathbf{J}_g = e z n_g \mathbf{V}_g$ the current density due to the species g ($z_e = -1$), and the interaction with the electric field is described by the electric force $\mathbf{f}_{Eg} = e z n_g \mathbf{E}$.

The external force due to the momentum of particles sources is not accounted for in Eq.(2)$_2$. We simply imply that this force is being driven aiming at some minimum of plasma velocity (for instance optimizing the direction of the fuelling beam), because then maximal power is transferred into the heat, which increases the fusion gain. Moreover, the longitudinal velocities are assumed be zeroed: $V_{i\parallel} = \mathbf{V}_i \mathbf{b} = 0$ ($\mathbf{b} = \mathbf{B}/B$ is unit vector along magnetic field). As the consequences of absence the centrifugal force, the longitudinal electric field $E_\parallel$ is negligibly small compared to T_g/r_0 (with r_0 the magnetic axis radius), which can explain why we assume n_g and p_g as surface functions at good longitudinal thermal conductivity of plasma.

The other terms in Eq.(2)$_2$ are the friction forces $\mathbf{f}_{gg'f}$ between electrons and ions due to collisions between the particles of different gases g and g'; in TOKES model they are given by $\mathbf{f}_{gg'f} = q_{gg'}(\mathbf{V}_{g'} - \mathbf{V}_g)$ per unit volume, with the coefficient $q_{gg'} = m_g n_g \nu_{gg'}$. The $\nu_{gg'}$ is collision frequency of one particle of the gas g with the particles of the gas g'. In a strong magnetic field the difference $\mathbf{u}_{g'g} = \mathbf{V}_{g'} - \mathbf{V}_g$ influences the friction force dependently on the direction of $\mathbf{B}$: $\mathbf{f}_{gg'f} = q_{gg'}(\alpha_{g'g}\mathbf{u}_{g'g\parallel} + \mathbf{u}_{g'g\perp})$, with the factor $\alpha_{g'g}$ of 0.3−0.5. Due to the requirement of momentum conservation for the system of two fluids, we have the equality $\mathbf{f}_{gg'f} = -\mathbf{f}_{g'gf}$ therefore the collision frequencies and the coefficients α are symmetric on g-g':

$$q_{gg'} = m_g n_g \nu_{gg'} = m_{g'} n_{g'} \nu_{g'g} = q_{g'g}, \qquad \alpha_{g'g} = \alpha_{gg'} \tag{3.4}$$

We assume that the frequencies depend on n_g, $n_{g'}$ T_g and $T_{g'}$. Thus $\nu_{gg'}$ are surface functions.

The most important process in the confined plasmas is the thermal transport across the magnetic surfaces. One essential contribution to Q_g, described by the term $Q_{g\mathrm{th}} = -\nabla \mathbf{q}_{g\mathrm{th}}$, is due to the thermal flux $\mathbf{q}_{g\mathrm{th}} = -\kappa_{g\perp}\nabla_\perp T_g$ caused by the temperature gradient, with $\kappa_{g\perp}$ the thermal cross-conductivity. The values of $\kappa_{g\perp}$ are crucially important for energy confinement.

There are also some other sources and sinks in the equations: for instance due to heat exchange between the fluids, the Joule heating, fusion power and radiation loss. Those terms are considered in later sections. (Thermoforce contributions are not implemented.)

4. The Ohm's law and the Joule heating

The plasma equilibrium equation Eq.(2.1) is the sum of equations Eq.(3.2)$_2$ over electrons and ions, which allows elimination of the electron equation. For ions we have:

$$\begin{aligned}
\mathbf{n}\frac{\partial p_i}{\partial n} &= \frac{e}{c}z_i n_i \mathbf{V}_i \times \mathbf{B} + e z_i n_i \mathbf{E} - m_e n_e \nu_{ei}\left(\alpha_{ei}u_{eib}\mathbf{b} + \mathbf{u}_{ei\perp}\right) \\
&+ m_i n_i \sum_{j \neq i}\nu_{ij}\left(\alpha_{ji}\left(u_{ejb} - u_{eib}\right)\mathbf{b} + \mathbf{u}_{ej\perp} - \mathbf{u}_{ei\perp}\right)
\end{aligned} \tag{4.1}$$

The unit vectors $\mathbf{n}$ and $\mathbf{b}$ are directed normally to the local magnetic surface and along the local magnetic field, respectively, and $\mathbf{w} = \mathbf{b}\times\mathbf{n}$. The relative velocities $\mathbf{u}_{ei} = \mathbf{V}_i - \mathbf{V}_e$, with $i \equiv mz$ (alternatively j and k are in use like i). The current in quasineutral plasma reads:

$$\mathbf{J} = e\sum_i z_i n_i \mathbf{u}_{ei} \tag{4.2}$$

From Eq.(1) the velocities $\mathbf{u}_{ei}$ are obtained in terms of $\mathbf{E}$ and $\mathbf{V}_i$. Substitution of $\mathbf{u}_{ei}$ into Eq.(2) gives the Ohm's law that expresses $\mathbf{J}$ in terms of $\mathbf{E}$ and a plasma velocity $\mathbf{V}_c$ which is introduced later. The calculations are performed introducing the following designations:

$$q_{ei} = q_{ie} = m_e n_e v_{ei} = m_i n_i v_{ie}, \qquad q_{ij} = q_{ji} = m_i n_i v_{ij} = m_j n_j v_{ji} \qquad (4.3)$$

$$f_i = \frac{z_i n_i}{n_e}, \qquad q_e = m_e v_e n_e, \qquad (4.4)$$

Electron-electron collision frequency $v_e \sim v_{ei}$ and thus $q_{ei} \sim q_e$, but $q_{ij} \gg q_e$ because of large ratio m_i/m_e (typically $q_{ij}/q_e \sim (m_i/m_e)^{1/2} \gg 1$ can be obtained). The charge density fractions f_i satisfy the equality $\sum_i f_i = 1$. In new form Eq.(1) reads:

$$
\begin{aligned}
\mathbf{n}\frac{\partial p_i}{\partial n} &= \frac{q_e f_i}{\varepsilon_e}\mathbf{V}_i \times \mathbf{b} + e n_e f_i \mathbf{E} - q_{ei}\left(\alpha_{ei} u_{eib}\mathbf{b} + \mathbf{u}_{ei\perp}\right) \\
&+ \sum_{j \neq i} q_{ij}\left(\alpha_{ji}\left(u_{ejb} - u_{eib}\right)\mathbf{b} + \mathbf{u}_{ej\perp} - \mathbf{u}_{ei\perp}\right)
\end{aligned}
\qquad (4.5)
$$

The frequency ratio $\varepsilon_e = v_e/\omega_e$ is a small parameter ($\varepsilon_e \ll 1$). In respect to $\mathbf{u}_{ei}$, Eq.(5) is a system of linear algebraic equations. We project it on the orts $\mathbf{b}$, $\mathbf{n}$ and $\mathbf{w}$:

$$\sum_j A_{ij} u_{ejb} = \frac{e f_i}{m_e v_e} E_b, \qquad \sum_j C_{ij} u_{ejn} = \frac{e f_i}{m_e v_e} E_n + \frac{f_i}{\varepsilon_e} V_{iw} - \frac{1}{q_e}\frac{\partial p_i}{\partial n} \qquad (4.6)$$

$$\sum_j C_{ij} u_{ejw} = \frac{e f_i}{m_e v_e} E_w - \frac{f_i}{\varepsilon_e} V_{in} \qquad (4.7)$$

$$A_{ij} = \left(\alpha_{ei}\frac{q_{ei}}{q_e} + \sum_k \alpha_{ik}\frac{q_{ik}}{q_e}\right)\delta_{ij} - \alpha_{ij}\frac{q_{ij}}{q_e}, \qquad C_{ij} = A_{ij}\big|_{\alpha=1} \qquad (4.8)$$

The matrices $[A_{ij}]$ and $[C_{ij}]$ are symmetric ($A_{ij} = A_{ji}$ and $C_{ij} = C_{ji}$) and dimensionless, with typical matrix elements of the order of $(m_i/m_e)^{1/2} \gg 1$. The values of α_{ii} and q_{ii} which appear in Eq.(8)$_1$ cancel therefore we do not need them. The subscript $\alpha = 1$ in Eq.(8)$_2$ means 'at $\alpha_{ei} = 1$ and $\alpha_{ij} = 1$'. Solving of the problem includes obtaining the reciprocal matrices $[A_{ij}]^{-1}$ ($\sum_k A_{ik}^{(-1)} A_{kj} = \delta_{ij}$) and $[C_{ij}]^{-1}$ (their matrix elements are of order of 1), which calculates the code. As the result, the ion relative velocities are obtained:

$$\mathbf{u}_{ei} = -\mathbf{n}\sum_j C_{ij}^{(-1)}\frac{1}{q_e}\frac{\partial p_j}{\partial n} + \frac{e}{m_e v_e}\left(\begin{array}{c} E_b \mathbf{b}\sum_j A_{ij}^{(-1)} f_j + \mathbf{E}_\perp \lambda_i \\ +\sum_j C_{ij}^{(-1)} f_j \frac{1}{c}\mathbf{V}_j \times \mathbf{B} \end{array}\right), \quad \lambda_i = \sum_j f_j C_{ij}^{(-1)} \quad (4.9)$$

Substitution of $\mathbf{u}_{ei}$ into Eq.(2) gives the Ohm's law:

$$\mathbf{J} = \sigma_\parallel E_b \mathbf{b} + \sigma_\perp\left(\mathbf{E}_\perp + \frac{1}{c}\mathbf{V}_c \times \mathbf{B}\right) - \frac{e n_e}{q_e}\sum_j \lambda_j \frac{\partial p_j}{\partial n}\mathbf{n} \qquad (4.10)$$

16

Longitudinal, $\sigma_\parallel$, and transversal, $\sigma_\perp$, conductivities and the plasma velocity $\mathbf{V}_c$ are given by

$$\sigma_\parallel = \frac{e^2 n_e}{m_e \nu_e} \sum_i f_i \sum_j f_j A_{ij}^{(-1)}, \quad \sigma_\perp = \frac{e^2 n_e}{m_e \nu_e} \lambda \qquad (4.11)$$

$$\mathbf{V}_c = \frac{1}{\lambda} \sum_j f_j \lambda_j \mathbf{V}_j, \qquad \lambda = \sum_j f_j \lambda_j \qquad (4.12)$$

The quantities $D_\perp = c^2/(4\pi\sigma_\perp)$ and $D_\parallel = c^2/(4\pi\sigma_\parallel)$ are the transversal and longitudinal magnetic diffusivity, respectively, and we have $D_\parallel = D_\perp/\eta_\sigma$, with the ratio $\eta_\sigma = \sigma_\parallel/\sigma_\perp$. Being some functions of the densities and the temperatures, $\sigma_\parallel$, $\sigma_\perp$, $D_\parallel$, $D_\perp$ and the dimensionless coefficients λ_j and λ are surface functions.

With $\mathbf{u}$ the local coordinate velocity Eq.(2.16), the relative velocities $\mathbf{v}_g = \mathbf{V}_g - \mathbf{u}$ and the relative plasma velocity $\mathbf{v}_c = \mathbf{V}_c - \mathbf{u}$ are introduced. Eq.(10) shows that both the electric field in the plasma frame $\mathbf{E}'' = \mathbf{E}' + (1/c)\mathbf{v}_c \times \mathbf{B}$ and the pressure gradient drive the plasma current. We invert Eq.(10) and obtain:

$$E_b = \frac{J_b}{\sigma_\parallel}, \qquad \mathbf{E}'_\perp = \mathbf{E}^{(p)} + \frac{1}{en_e}\frac{1}{\lambda}\sum_j \lambda_j \frac{\partial p_j}{\partial n}\mathbf{n}, \quad \mathbf{E}^{(p)} = \mathbf{w}\frac{J_w}{\sigma_\perp} - \frac{1}{c}\mathbf{v}_c \times \mathbf{B} \quad (4.13)$$

The field part $\mathbf{E}^{(p)}$ does not account for the contribution of pressure gradient.

One important process in the plasma is the Joule heating $W_J = \mathbf{J}\mathbf{E}^{(p)}$, which is the work of electric charges against the electric field part $\mathbf{E}^{(p)}$. Expressing W_J in terms of $\mathbf{J}$ we get

$$W_J = J_b E_b + J_w E_w^{(p)} = \frac{J_b^2}{\sigma_\parallel} + \frac{J_w^2}{\sigma_\perp} \qquad (4.14)$$

In TOKES model whole Joule heating is applied to electron fluid.

As a simplified example, let's consider only one ion species of charge state $z = 1$, without volumetric sources such as fusion power and radiation losses, with x a Cartesian coordinate x. Steady state is assumed: $(\partial/\partial t = 0)$. The magnetic field has two components, B_z and B_y ($B_x = 0$). The electric field has a potential therefore $E_y = 0$ and $E_z = 0$. The longitudinal ion velocity equals also zero: $V_{i\parallel} = 0$. The friction force factor $\alpha_{ie} = 1$. The current $\mathbf{J} = en(\mathbf{V}_i - \mathbf{V}_e)$ flows perpendicularly to the axis x: $J_x = 0$ therefore $V_{ix} = V_{ex} \equiv V_x$. The continuity equation is immediately integrated: $nV_x = \text{const}$, and other equations take the form:

$$\frac{\partial p_i}{\partial x} = enE_x + \frac{e}{c}n(V_{iy}B_z - V_{iz}B_y), \qquad \frac{\partial p_e}{\partial x} = -enE_x - \frac{e}{c}n(V_{ey}B_z - V_{ez}B_y) \quad (4.15)$$

$$\frac{\partial}{\partial x}\left(\frac{3}{2}T_e n V_x\right) + p_e\frac{\partial V_x}{\partial x} = \frac{\partial}{\partial x}\left(\kappa_{e\perp}\frac{\partial T_e}{\partial x}\right) + 3\frac{m_e}{m_i}n\nu_{ei}(T_i - T_e) + \frac{J_y^2 + J_z^2}{\sigma} \quad (4.16)$$

$$\frac{\partial}{\partial x}\left(\frac{3}{2}T_i n V_x\right) + p_i \frac{\partial V_x}{\partial x} = \frac{\partial}{\partial x}\left(\kappa_{i\perp}\frac{\partial T_i}{\partial x}\right) + 3\frac{m_e}{m_i}n\nu_{ei}(T_e - T_i) \tag{4.17}$$

The conductivity $\sigma = e^2 n / m_e \nu_{ei}$. Eq.(2.1) and the expression for E_x follow as

$$\frac{\partial p}{\partial x} = \frac{1}{c}\left(J_y B_z - J_z B_y\right) \qquad E_x = -\frac{1}{c}\left(V_{ey}B_z - V_{ez}B_y\right) - \frac{1}{en}\frac{\partial p_e}{\partial x} \tag{4.18}$$

Zeroed projections of Eq.(1) onto y- and z-axes give the expressions for zeroed E_y and E_z:

$$E_y = 0 = \frac{1}{c}V_x B_z + \frac{J_y}{\sigma} \qquad E_z = 0 = -\frac{1}{c}V_x B_y + \frac{J_z}{\sigma} \tag{4.19}$$

From Eq.(2.2) we express $\mathbf{J}$ in terms of $\mathbf{B}$:

$$J_y = -\frac{c}{4\pi}\frac{\partial B_z}{\partial x}, \qquad J_z = \frac{c}{4\pi}\frac{\partial B_y}{\partial x} \tag{4.20}$$

Eliminating J_y and J_z we transform the sum of Eq.(16) with Eq.(18)$_1$ and Eq.(19) as

$$\frac{\partial}{\partial x}\left(\frac{3}{2}p V_x\right) + p\frac{\partial V_x}{\partial x} = \frac{\partial}{\partial x}\left(\kappa_{e\perp}\frac{\partial T_e}{\partial x} + \kappa_{i\perp}\frac{\partial T_i}{\partial x}\right) + \frac{c^2}{(4\pi)^2\sigma}\left(\left(\frac{\partial B_z}{\partial x}\right)^2 + \left(\frac{\partial B_y}{\partial x}\right)^2\right) \tag{4.21}$$

$$p + \frac{B_y^2 + B_z^2}{8\pi} = C, \qquad \frac{\partial B_z}{\partial x} = \frac{B_z V_x}{D}, \qquad \frac{\partial B_y}{\partial x} = \frac{B_y V_x}{D}, \qquad D = \frac{c^2}{4\pi\sigma} \tag{4.22}$$

Eliminating magnetic field in Eq.(21) we get:

$$\frac{\partial}{\partial x}\left(\frac{3}{2}p V_x\right) + p\frac{\partial V_x}{\partial x} = \frac{\partial}{\partial x}\left(\kappa_{e\perp}\frac{\partial T_e}{\partial x} + \kappa_{i\perp}\frac{\partial T_i}{\partial x}\right) + \frac{V_x^2}{D}\frac{B_y^2 + B_z^2}{4\pi} \tag{4.23}$$

The flux $j = nV_x$ is given constant. From Eq.(18), Eq.(20) and Eq.(22) we get V_x:

$$V_x = -\frac{4\pi D}{B_z^2 + B_y^2}\frac{\partial p}{\partial x} \tag{4.24}$$

Substituting V_x in Eq.(23) we obtain:

$$\frac{\partial}{\partial x}\left(\frac{3}{2}p V_x\right) + p\frac{\partial V_x}{\partial x} + V_x\frac{\partial p}{\partial x} = \frac{\partial}{\partial x}\left(\kappa_{e\perp}\frac{\partial T_e}{\partial x} + \kappa_{i\perp}\frac{\partial T_i}{\partial x}\right) \tag{4.25}$$

Hence the thermal equation takes the form:

$$\frac{\partial}{\partial x}\left(\frac{5}{2}(T_e + T_i)nV_x\right) = \frac{\partial}{\partial x}\left(\kappa_{e\perp}\frac{\partial T_e}{\partial x} + \kappa_{i\perp}\frac{\partial T_i}{\partial x}\right) \tag{4.26}$$

At constant flux $j = nV_x$ and neglecting the thermal conductivity we see that the sum of temperatures, $T_e + T_i$, remains constant in the flux. Each electron-ion pair carries through the imposed magnetic field not only the kinetic energy but it acquires also the work the plasma performs expanding through the field (the Joule heating). Thus the plasma expansion cooling described by the term $p\partial V_x/\partial x$ in Eq.(25) is fully compensated by the Joule heating. The electrons are heated by the Joule heating and the ions tend to cool due to the term $p_i\partial V_x/\partial x$ in

Eq.(17). The term of electron-ion energy exchange describes the transfer of the gained thermal energy to the ions, which limits their cooling in the course of plasma percolation through the magnetic field. Hence the Joule heating is included in the factor 5/2 of Eq.(26).

5. Pfirsch-Schlüter cross-transport

The following variables are introduced:

$$G_m(t,x) = \int_0^Y r^{m-2} \sqrt{g}\, dy, \qquad \Lambda_m(t,x) = \int_0^Y r^{m-2} \frac{g_{22}}{\sqrt{g}}\, dy \quad (m = 0, 1, \ldots) \quad (5.1)$$

Generally we term G_m the m-area and Λ_m the m-elongation. This is because G_2 is the area on the poloidal cross-section of the plasma slice between $x \pm \frac{1}{2}$, and Λ_2 averaged ratio of slice's length to its thickness. G_3 is the slice's volume (per 1 radian of ζ) so that the multiplication by different powers of r in the integrands changes meanings of G_m and Λ_m.

Toroidal magnetic field diffusion: Integrating Eq.(2.21) over y, we obtain the diffusion type equation for the toroidal magnetic field $\omega = rB_\zeta$:

$$\frac{\partial}{\partial t}(G_1 \omega) + \frac{\partial}{\partial x}(\upsilon_x G_1 \omega) = \frac{\partial}{\partial x}\left(D_\parallel \Lambda_1 \frac{\partial \omega}{\partial x}\right) \tag{5.2}$$

$$\upsilon_x = \left(\frac{\partial w}{\partial x}\right)^{-1}\left(\frac{D_\parallel}{G_1} \frac{\partial}{\partial x}\left(\Lambda_1 \frac{\partial w}{\partial x}\right) - \phi_w\right), \qquad \varphi_w = \varphi(t) + \frac{\partial w}{\partial t} \tag{5.3}$$

The function $\upsilon_x(t,x)$ expresses surface averaged convective velocity of toroidal magnetic field across the poloidal magnetic field. Being a parabolic differential equation, Eq.(2) needs an initial condition at $t = t_0$, where t_0 is some starting moment, and some boundary conditions. At $x = X$ we can use the vacuum value: $\omega(X) = \omega_{\text{vac}}$. At $x = 0$ the boundary condition is not needed, because the parabolic type of the equation degenerates at the magnetic axis due to vanishing diffusion coefficient (we can prove $\Lambda_1|_{x \to 0} \to 0$).

Plasma diffusion and ion-ion mixing: The ion continuity equation Eq.(3.2)$_1$ is transformed to the moving frame (x, y, ζ):

$$\frac{\partial}{\partial t}\left(r\sqrt{g}\, n_g\right) + \frac{\partial}{\partial x}\left(r\sqrt{g}\, \upsilon_g^1 n_g\right) + \frac{\partial}{\partial y}\left(r\sqrt{g}\, \upsilon_g^2 n_g\right) = s_g r\sqrt{g} \tag{5.4}$$

Integrating over y we obtain the ion species cross-transport equations:

$$\frac{\partial}{\partial t}(G_3 n_i) + \frac{\partial}{\partial x}\left(n_i \int_0^Y r\sqrt{g}\, \upsilon_i^1 dy\right) = S_i, \qquad S_i(t,x) = \int_0^Y s_i r\sqrt{g}\, dy \tag{5.5}$$

19

Then this equation is reduced to the form:

$$\frac{\partial}{\partial t}\left(G_3 n_i\right) + \frac{\partial}{\partial x}\left(G_3 n_i v_x\right) = \frac{\partial}{\partial x}\left(A\Pi_i\right) + S_i, \qquad A = G_3 \frac{4\pi D_\parallel}{\omega^2} \tag{5.6}$$

$$\Pi_i = n_i L \frac{\partial p}{\partial x} + \frac{C}{z_i}\left(\sum_{j\neq i}\frac{a_{ij}}{a_e}\left(\frac{n_j}{z_i}\frac{\partial p_i}{\partial x} - \frac{n_i}{z_j}\frac{\partial p_j}{\partial x}\right) + \frac{a_{ei}}{a_e}\left(\frac{n_e}{z_i}\frac{\partial p_i}{\partial x} + n_i\frac{\partial p_e}{\partial x}\right)\right) \tag{5.7}$$

$$L = \left(2\pi q\right)^2 \frac{\mathrm{H}}{G_1^2} - \frac{\Lambda_5'}{G_3}, \qquad C = \frac{\sigma_\parallel}{\sigma_\perp}\lambda\frac{\Lambda_5'}{G_3}, \qquad q = -\frac{\omega}{2\pi}\left(\frac{\partial w}{\partial x}\right)^{-1} G_1 \tag{5.8}$$

$$\Lambda_5' = \int_0^Y \left(1 + \frac{g^{11}}{\omega^2}\left(\frac{\partial w}{\partial x}\right)^2\right)^{-1} r^3 \frac{g_{22}}{\sqrt{g}}\,dy \approx \Lambda_5, \qquad , \qquad \mathrm{H} = \frac{G_5}{G_3} - \frac{G_3}{G_1} \tag{5.9}$$

Here the parameter q is the safety factor. The dimensionless factors L and C comprise main influence of the magnetic configuration shape upon the plasma diffusion. The parameters $q_{gg'}$ include the product $n_g n_{g'}$ which we extract now as $q_{gg'} = n_g n_{g'} a_{gg'}$, and we do similarly as $q_e = n_e^2 a_e$. The coefficients $a_{gg'}$ and a_e do not substantially depend on the densities, however they remain symmetric like $q_{gg'}$: $a_{gg'} = a_{g'g}$.

The coefficients at the derivatives in Eq.(7) are of order of 1 but the ratio $a_{ij}/a_e \sim (m_i/m_e)^{1/2} \gg 1$. This inequality means fast mutual diffusive mixing among the ion species in comparison with the plasma diffusion. Indeed, in the equation for the electron density n_e (which follows from Eq.(6) multiplying it by z_i and summing over i) the ion mixing terms mutually cancel:

$$\Pi_e = \sum_i z_i \Pi_i = n_e L \frac{\partial p}{\partial x} + C\sum_i \frac{a_{ei}}{a_e}\left(\frac{n_e}{z_i}\frac{\partial p_i}{\partial x} + n_i\frac{\partial p_e}{\partial x}\right) \tag{5.10}$$

Thus the electron equation (which is the plasma diffusion equation) reads

$$\frac{\partial}{\partial t}\left(G_3 n_e\right) + \frac{\partial}{\partial x}\left(G_3 n_e v_x\right) = \frac{\partial}{\partial x}\left(A\Pi_e\right) + S_e, \qquad S_e = \sum_i z_i S_i \tag{5.11}$$

As we see, the driving force of plasma transport is the gradient of partial pressures.

The number of diffusion equations (with $i = (mz)$ describing one atomic kind m can be reduced to one equation (averaged charge approximation). After summing on z Eq.(6) reads:

$$\frac{\partial}{\partial t}\left(G_3 n_m\right) + \frac{\partial}{\partial x}\left(G_3 n_m v_x\right) = \frac{\partial}{\partial x}\left(A\sum_z \Pi_{mz}\right) + S_m, \qquad S_m = \sum_z S_{mz} \tag{5.12}$$

The summing of Π_i is simplified reasonably assuming that the distribution of ions of the kind m has a profile on z significantly peaked at the averaged charge $z = z_m(t,x)$. Therefore z_i, a_{ei} and a_{ij} are replaced by their averaged values z_m, a_{em} and $a_{mm'}$, respectively (a_{em} and $a_{mm'}$ are a_{ei} and a_{ij} calculated at $z = z_m$). In the terms that contain only the summation on z, the densities n_i

in the coefficients before the derivatives are replaced by the averaged ion densities n_m. Then the sum is approximated as

$$\Pi_m = \sum_z \Pi_{mz} = \frac{1}{z_m} \sum_{m' \neq m} \begin{pmatrix} C\dfrac{a_{mm'}}{a_e}\left(\dfrac{n_{m'}}{z_m}\dfrac{\partial p_m}{\partial x} - \dfrac{n_m}{z_{m'}}\dfrac{\partial p_{m'}}{\partial x}\right) \\ +z_m n_m \left(L\dfrac{\partial p_{m'}}{\partial x} + z_{m'}\left(L + \dfrac{C}{z_m}\dfrac{a_{em}}{a_e}\right)\dfrac{\partial}{\partial x}(T_e n_{m'})\right) \end{pmatrix}$$

$$+\left(n_m L + \frac{C}{z_m}\frac{a_{em}}{a_e}\frac{n_e}{z_m}\right)\frac{\partial p_m}{\partial x} + n_m \left(L z_m + C\frac{a_{em}}{a_e}\right)\frac{\partial}{\partial x}(T_e n_m) \qquad (5.13)$$

The total ion species pressure $p_m = T_m n_m$. Thus, the averaged equation Eq.(12) looks rather similar to the original equation Eq.(6), but with z_m depending on t and x. Eq.(13) for all but main ion species and Eq.(11) are solved numerically with the code TOKES, which is explained in later sections.

Thermal energy transport: The thermal energy equation Eq.(3.3) is transformed to the moving frame:

$$\frac{\partial}{\partial t}\left(r\sqrt{g}\,\frac{3}{2}n_g T_g\right) + p_g \frac{\partial}{\partial t}\left(r\sqrt{g}\right) + \frac{\partial}{\partial x}\left(r\sqrt{g}\,\frac{3}{2}T_g n_g v_g^1\right)$$

$$+p_g \frac{\partial}{\partial x}\left(r\sqrt{g}\,v_g^1\right) + \frac{\partial}{\partial y}\left(r\sqrt{g}\,\frac{5}{2}T_g n_g v_g^2\right) = r\sqrt{g}Q_g \qquad (5.14)$$

Integrating over y and after some transformations we obtain:

$$\frac{\partial}{\partial t}\left(G_3 \frac{3}{2}p_g\right) + p_g \frac{\partial G_3}{\partial t} + \frac{\partial}{\partial x}\left(v_x G_3 \frac{3}{2}p_g\right) + p_g \frac{\partial}{\partial x}(v_x G_3) =$$

$$= \frac{\partial}{\partial x}\left(\frac{3}{2}p_g \frac{A\Pi_g}{n_g}\right) + p_g \frac{\partial}{\partial x}\left(\frac{A\Pi_g}{n_g}\right) + \int_0^Y r\sqrt{g}Q_g\,dy \qquad (5.15)$$

As one important term contributing to Q_g we consider the thermal conduction $Q_{g\nabla\perp}$:

$$Q_{g\nabla\perp} = \nabla\left(\kappa_{g\perp}\nabla_\perp T_g\right) \qquad (5.16)$$

The vector $\kappa_{g\perp}\nabla_\perp T_g$ has only one non-zeroed covariant component (along the normal to the magnetic surface) which is equal to $\kappa_{g\perp}\partial T_g/\partial x$. Its contravariant components along x- and y-axes needed in Eq.(16) follow as $g^{11}\kappa_{g\perp}\partial T_g/\partial x$ and $g^{12}\kappa_{g\perp}\partial T_g/\partial x$, respectively. Then the thermal conduction term of Eq.(15) takes the form

$$\int_0^Y r\sqrt{g}Q_{g\nabla\perp}\,dy = \frac{\partial}{\partial x}\left(\frac{\partial T_g}{\partial x}\int_0^Y \kappa_{g\perp}r\frac{g_{22}}{\sqrt{g}}\,dy\right) \qquad (5.17)$$

Finally we replace the index g by the index m, assuming the summing on the charge states z.

The cross thermal conductivity $\kappa_{g\perp}$ depends on y, in some models it depends on y via the magnetic field B. It is to note that realistic plasma diffusion and thermal transport models

are rather uncertain. They cannot provide the accuracy sufficient to demand discrimination of the different variations of $\kappa_\perp$ along y, which justifies rather rough simplifications of dependence of $\kappa_\perp$ on y. In TOKES we assume that in $\kappa_\perp$ the value of only toroidal magnetic field is used. After that we can prove that the classical $\kappa_\perp$ becomes to be proportional to r^2 and that by Bohm to r. In case of the gyro-Bohm transport, for which the proportionality to $r^2 g_{22}/g$ follows, for simplicity the ratio g_{22}/g is approximated by its averaged value along the integration contour of Eq.(17). Finally the value of $\kappa_{g\perp}$ with $B = B_0$ at the magnetic axis of the contour multiplied by the factor $(r/r_0)^2$ is used for the classical (and neoclassical) transport and the Bohm's transport, and in the case of gyro-Bohm transport additional constant factor c_{GB} replaces the factor g_{22}/g. For instance, the gyro-Bohm constant thermal conductivity takes the form:

$$\kappa_{e\perp}^{GB} \approx \frac{1}{32}\frac{c_{GB}\upsilon_{Te}^{3/2}}{\omega_e^2(B_0)}\frac{\partial n_e}{\partial x}\,, \qquad\qquad c_{GB} = \frac{1}{Y}\int_0^Y \frac{g_{22}}{g}\,dy \qquad\qquad (5.18)$$

Thus, Eq.(17) acquires the form:

$$\int_0^Y r\sqrt{g}\,Q_{g\nabla\perp}\,dy = \frac{\partial}{\partial x}\left(\kappa_{g\perp}\,\frac{\Lambda_5}{r_0^2}\frac{\partial T_g}{\partial x}\right) \qquad\qquad (5.19)$$

Internal energy transport: Internal energy of an atomic component of plasma consists of internal energies of single atoms which can be in different ionization states, and each ionization state can be at different excitation levels of bound electrons. The internal energy of an atom of a kind m is assumed be equal to zero if the atom's charge state z is equal to zero ($z = 0$) and the electron levels (indexed with k) are unpopulated but the ground state ($k = 0$). The atom in the charge state $z > 0$ and ground state of the ion ($k = 0$) acquires the internal energy that is the sum of ionization potentials I_z: $E_{mz0} = \sum_{z'} I_{z'}$ ($0 \le z' < z$). For instance, for helium we have $I_0 = 24.6$ eV and $I_1 = 54.4$ eV. Thus the fully ionized He-atom ($z = Z_m = 2$) has the internal energy $E_{(He)2,0} = 79$ eV. Fully ionized atoms do not have excited levels ($k = 0$ is the only possible index at $z = Z_m$). At $z < Z_m$ we assume some finite number $K_{mz} > 0$ of excited levels ($0 \le k \le K_{mz}$) with some internal energies E_{mzk} exceeding E_{mz0} by the values of excitation energy of bound electrons.

We assume that at the transport sub-step the internal energy is calculated without changing level populations. Each population diffuses equally on z and k, which is described by the transport equation for the ionized atoms of kind m in the averaged charge approximation. E.g. ion transport equation Eq.(12) provides some velocity υ'_m which allows the calculation of transport of internal energy using the convective equations for each n_{mzk}:

$$\frac{\partial}{\partial t}\left(G_3 n_{mzk}\right) + \frac{\partial}{\partial x}\left(G_3 \upsilon_m' n_{mzk}\right) = 0, \qquad \upsilon_m' = \upsilon_x + \upsilon_{xm}, \quad \upsilon_{xm} = -\frac{A\Pi_m}{G_3 n_m} \qquad (5.20)$$

Strong magnetic field: If the vacuum value of $rB_\zeta = \omega_{vac}$ tries to infinity (thus $\omega \to \infty$), we put $\upsilon_x = 0$, which provides a regular solution to Eq.(2) for finite variable $\omega - \omega_{vac}$. TOKES can simulate only this limiting case so far. At $\upsilon_x = 0$ the function $\Lambda_1(x)$ follows as

$$\Lambda_1 = \left(\frac{\partial w}{\partial x}\right)^{-1} \int_0^x \frac{G_1}{D_\parallel}\left(\varphi(t) + \frac{\partial w}{\partial t}\right) dx \qquad (5.21)$$

The Grad-Shafranov equation Eq.(2.7) is integrated over y:

$$\frac{\partial w}{\partial x}\frac{\partial}{\partial x}\left(\Lambda_1 \frac{\partial w}{\partial x}\right) + G_1 \frac{\partial}{\partial x}\left(\frac{\omega^2}{2}\right) + 4\pi G_3 \frac{\partial p}{\partial x} = 0 \qquad (5.22)$$

Substituting Eq.(21) into Eq.(22) gives the equation on ω:

$$\frac{\partial}{\partial x}\left(\frac{\omega^2}{2}\right) = -4\pi\frac{G_3}{G_1}\frac{\partial p}{\partial x} - \frac{1}{D_\parallel}\frac{\partial w}{\partial x}\left(\varphi(t) + \frac{\partial w}{\partial t}\right), \qquad \omega(X) = \omega_{vac} \qquad (5.23)$$

Using Eq.(23) in Eq.(2.7) enables to calculate the metric coefficients G_m. To calculate J_ζ in Eq.(2.6), ω is eliminated using Eq.(23) and we get:

$$J_\zeta = \frac{c}{r}\left(\left(\frac{\partial w}{\partial x}\right)^{-1}\frac{\partial p}{\partial x}\left(r^2 - \frac{G_3}{G_1}\right) - \frac{1}{4\pi D_\parallel}\left(\varphi + \frac{\partial w}{\partial t}\right)\right) \qquad (5.24)$$

Thus, the large variable ω^2 is eliminated.

The bootstrap current: Let's calculate the derivative of the full toroidal current through a magnetic surface, or dI/dx, using Eq.(24). We have

$$\frac{dI}{dx} = \oiint J_\zeta \sqrt{g}\, dy = c\oiint\left(\left(\frac{\partial w}{\partial x}\right)^{-1}\frac{\partial p}{\partial x}\left(r^2 - \frac{G_3}{G_1}\right) - \frac{1}{4\pi D_\parallel}\left(\varphi + \frac{\partial w}{\partial t}\right)\right)\sqrt{g}\,\frac{dy}{r} \qquad (5.25)$$

The term proportional to $\partial p/\partial x$ is equal to zero, which follows from the calculation:

$$\oint\left(r^2 - \frac{G_3}{G_1}\right)\frac{\sqrt{g}}{r}\,dy = \oint r\sqrt{g}\,dy - \frac{G_3}{G_1}\oint\frac{\sqrt{g}}{r}\,dy = G_3 - \frac{G_3}{G_1}G_1 \equiv 0 \qquad (5.26)$$

The non-zero contribution to the toroidal current that does not depend on ϕ can come due to the flow υ_x of the toroidal magnetic flux W across the poloidal flux w. In the initial approximation on the strong magnetic field υ_x equals zero. Calculating the next approximation we obtained a contribution to the current that does not vanish at $\phi = 0$ and $\partial/\partial t = 0$. Such current is called the bootstrap current I_{BC}, and we obtained:

$$\frac{dI_{BC}}{dx} = c \frac{G_3}{G_1} \Lambda_1 \left(\frac{1}{\omega} \frac{\partial w}{\partial x} \right)^2 \frac{\partial p}{\partial w} \tag{5.27}$$

In Ref.[8] the following expression for the bootstrap current density is given:

$$J_{BC}^W = -\frac{c}{B_y} \frac{dp}{dr} \qquad \Rightarrow \qquad \frac{dJ_{BC}^W}{dx} = -c \frac{\partial p}{\partial x} \oint \frac{\sqrt{g}}{B_y \sqrt{g_{11}}} dy \tag{5.28}$$

Comparing Eq.(27) and Eq.(28) we obtained:

$$\frac{dI_{BC}}{dI_{BC}^W} \approx \frac{1}{2\pi} \left(\frac{\varepsilon}{q} \right)^2 \tag{5.29}$$

Thus, the generally accepted bootstrap current is much larger than one obtained here. In the code TOKES both contributions are summed.

6. Realistic plasma transport coefficients

We have to assign the collision frequencies mentioned in Eq.(3.4). It is to note that the validity of transport simulation with the Pfirsch-Schlüter (PS) model is questionable, even if we try to fit the classical Spitzer's frequencies $\nu_{gg'}$ of PS model to the reality with some factors $f_{gg'}$. However, the realistic transport in tokamaks isn't so far sufficiently described therefore such a heuristic approach can be initially used. The PS MHD approach implies the collisions between plasma particles being so frequent that the particle's free path λ_g is small: $\lambda_g \ll a$ (with a poloidal plasma size). This is far of modern tokamaks conditions, even when the drastic decrease of λ_g due to plasma turbulence is accounted for.

The neoclassical theory for realistic ratio $(\lambda_g \gg r_0)$ Ref.[9] suggests the 'banana' regime transport that yields significant increase of plasma diffusivity $D_\perp = c^2/4\pi\sigma_\perp$ compared to the PS model. Without discussing the details of rare collisions at the inverted aspect ratio $a/r_0 = \varepsilon \ll 1$, we used the fitting factor $f = \varepsilon^{-3/2} \gg 1$ to account for the bananas, multiplying by f the Spitzer's plasma diffusivity. For instance, in the current ITER design the following parameters are accepted: $r_0 = 6.2$ m and $a = 2.0$ m. Thus we have $\varepsilon \approx 0.32$ and $f \approx 5.5$. The frequency enhancement is relevant to plasma transport but electron-electron and electron-ion energy exchange may keep the Spitzer's frequencies.

Increasing at fixed ε the ratio r_0/λ_g from zero, initially the banana regime $(f \sim \varepsilon^{-3/2})$ and finally the PS regime $(f = 1)$ occur. There is also an intermediate case with weakly varying conductivity $\sigma_\perp$ (the 'plateau' regime) at which the factor f drops from $\varepsilon^{-3/2}$ down to 1. The

safety factor q influences the regime's ranges. In TOKES the actual fitting factor is postulated by the simple approximation formula which the equality $q_{g'g} = q_{gg'}$:

$$f_{g'g} = \left[1 - \left(1 - \varepsilon^{-3/2}\right)\frac{\ln\xi}{\ln\varepsilon^{3/2}}, \quad \begin{array}{l} \varepsilon^{-3/2}, \quad \xi < \varepsilon^{3/2} \\ \varepsilon^{3/2} < \xi < 1, \quad \xi = 2q\left(\frac{r_0}{\lambda_{g'g}} + \frac{r_0}{\lambda_{gg'}}\right) \\ 1, \quad \xi > 1 \end{array} \right. \tag{6.1}$$

The ratio $\sigma_\parallel / \sigma_\perp$ becomes also dependent of ε. The longitudinal conductivity $\sigma_\parallel$ does not obey the dependence imposed by Eq.(1) upon $\sigma_\perp$. It weakly depends on ε as $\sigma_\parallel \propto 1 - 2\varepsilon^{1/2}$, which is due to appearance of "trapped" charged particles that don't carry longitudinal current. As the result, we assume the dependence of the factors $\alpha_{gg'}$ defined at Eq.(3.4) as

$$\alpha_{g'g}^{\text{eff}} = \frac{1 - 2\sqrt{\varepsilon}}{f_{g'g}} \alpha_{g'g} \tag{6.2}$$

In practice, the energy confinement time τ_E represents the result of a number of transport processes including anomalous diffusion and convection Ref.[8]. In neoclassical theory the diffusive energy fluxes q_i and the particle fluxes Γ_i of plasma species are driven by radial gradients of all densities n_j and temperatures T_j. In simplest form when the contributions of the terms with $j \neq i$ are omitted the diffusive flux equations read:

$$\Gamma_i = -\alpha_{11}\frac{\partial n_i}{\partial w} - \alpha_{12}\frac{\partial T_i}{\partial w}, \qquad q_i = -\alpha_{21}\frac{\partial n_i}{\partial w} - \alpha_{22}\frac{\partial T_i}{\partial w} \tag{6.3}$$

The convection contribution would result in additional terms proportional to n_j. Usually the theory cannot provide correct values for the transport coefficients α_{mn} therefore experimental information is frequently used to quantify Eq.(3), albeit it relates mainly to the diagonal matrix element which are diffusion coefficient $D = \alpha_{11}$ and the thermal diffusivity $\chi = \alpha_{22}/n$.

Typical neoclassic values $D^n \sim 0.1 \text{ m}^2/\text{s}$ (for mutual diffusion of ions) and $\chi^n \sim 0.3 \text{ m}^2/\text{s}$ are generally accepted. The anomalous diffusivities are usually significantly larger than the neoclassical values, especially for electrons. The real values are $D \sim 0.4 \text{ m}^2/\text{s}$ and $\chi \sim 1 \text{ m/s}$, so that ions related diffusive fluxes are by factor of 3 to 4 larger than the neoclassical ones. The plasma real diffusivities governed essentially by electron transport are of the same order as that of ions, which differs drastically from the plasma neoclassical diffusivities which are smaller than D^n and χ^n by a factor of $(m_e/m_i)^{1/2}$. A general feature of the diffusivities is their increase toward the plasma edge. For ions in the plasma core the difference between neoclassical and real values can be not significant but for electrons the anomalous contributions are usually larger by a factor about 10 to 10^2.

Based on this available information, in TOKES we use Eq.(2) and multiply the plasma diffusivity $D_{PS} = 2q^2 D_\perp$ at first by the factor f given by Eq.(1) in order to take the banana effect into account. Then the modified diffusivities and the ion-ion mixing constants C_{ij} are multiplied by the anomalous factors $f_e = 35$ and $f_i = 3$, respectively.

7. MHD instabilities and beta limit

The stability of tokamak equilibrium can be analysed in terms of ideal or resistive linear modes Ref.[8]. Changes of plasma currents, pressure gradient and magnetic field curvature can produce instabilities and thus destroy the equilibrium, at least in vicinities of the resonance magnetic surfaces at which the safety factor q gets rational. The potentially strongest ideal MHD instability is the kink mode. At low β its driving force comes from $\partial J_\zeta / \partial w$, and $\partial p / \partial w$ contributes at high β. Typical inverted increments are of order of Alfven transit time (~ 0.1 μs). An important example of resistive instability is the tearing mode. It develops in a narrow layer at some resonance magnetic surface, and then the current redistributes by increased Ohm's resistivity there, which provides the saturation of the mode growth. In the resistive layer, for typical values $B_\zeta = 5$ T, $n = 10^{20}$ m^{-3} and $T = 5$ keV an analysis results in the inverted increment $\gamma^{-1} \sim 70$ ms and the layer width less than 1 mm. The kink and tearing modes can be avoided choosing some appropriate behaviour of q across the magnetic surfaces. For example, for the parabolic-like current profiles with the toroidal current density J_ζ vanishing at the plasma boundary, there is a stability window (see Fig.1). For example, the tokamak operation is predicted to be stable with $q_{min} = 1$ (at the magnetic axis) and $q_{max} = 3$ (at the plasma boundary).

Fig. 7.1 The window of stable tokamak operation

The code TOKES draws the profiles of J_ζ and $q(x)$ on the computer display during the calculation, which allows visual control of these scenario conditions. In scenarios with fixed magnetic field, this check should be done once at the start of simulation, and in scenarios with the evolving magnetic field no automatic control is implemented yet but visual control only.

The pressure gradient driven instabilities can be approximately characterized in terms of β limit. Let's assume sufficiently optimized plasma configuration in which most dangerous

current driven modes are avoided (i.e. the confinement occurs in the stability window). Increasing p we reach stability margin at some $\beta = \beta_{max}$ (the Troyon limit):

$$\beta_{max} = 2.8 \times 10^{-2} \frac{I}{aB_\zeta} \tag{7.1}$$

Here plasma current I [MA], the toroidal magnetic field B_ζ [T] and plasma minor radius a [m]. The quantity $\beta_N = 10^2 \beta/(I/aB_\zeta)$ is called the normalized beta, so that the beta limit can also be expressed as $\beta_N < g = 2.8$. Experimentally, peaking of current profile leads to some increase of β_{max} proportionally to the inductivity L as $g \approx 4L$.

In TOKES, the beta limit Eq.(1) is implemented by introducing additional factor f_β at the plasma diffusivity $D_\perp$ and the thermal conductivities $\kappa_\perp$ of deuterium and tritium:

$$f_\beta = \exp\left(\left(\frac{\beta_N}{g}\right)^4\right) \tag{7.2}$$

The local value of β_N is implied here (thus we use $\beta(w)$ in the definition of β_N). Due to the large power in the expression under the exponent of Eq.(2), the transport in the core increases drastically if β_N exceeds g, which automatically limits plasma pressure and thus β.

Part II   Implementation of magnetic configuration

8. Implementation of magnetic surfaces

In the TOKES numerical calculations *r* and *z* are discrete coordinates of the nodes of numerical contours at constant values of poloidal magnetic flux *w* (see Fig.1). The contours cover the whole poloidal cross-section of the tokamak vessel, Ω. To build those approximated magnetic flux coordinates, initially the domain Ω is covered by a triangular grid Fig.2 which is once generated by the code.

The wall surface is a contour of straight segments arbitrarily drawn by engineer-designer with indication of the surface segments as she or he decides. Then the grid generator of TOKES automatically calculates triangular meshes in Ω with providing the sizes of triangles that are comparable with that of other triangles and boundary segments nearby. Thus each triangle represents a toroidal cell of triangular poloidal cross-section. Then at the triangles' corners the values of *w* are calculated of some toroidal currents located as rings at
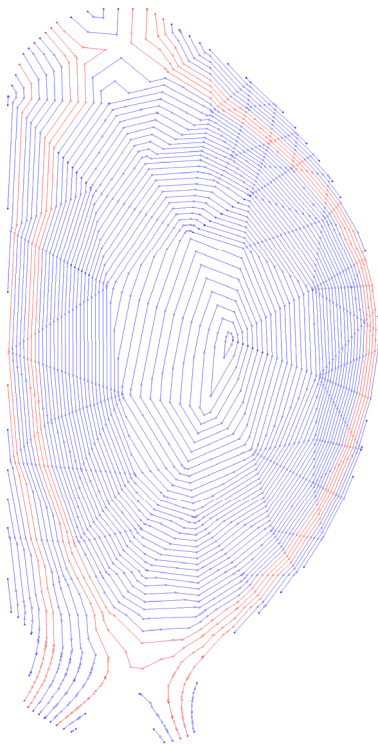

Fig. 8.1 The magnetic layers (vessel of ITER)   *Fig. 8.2 Triangular grid*
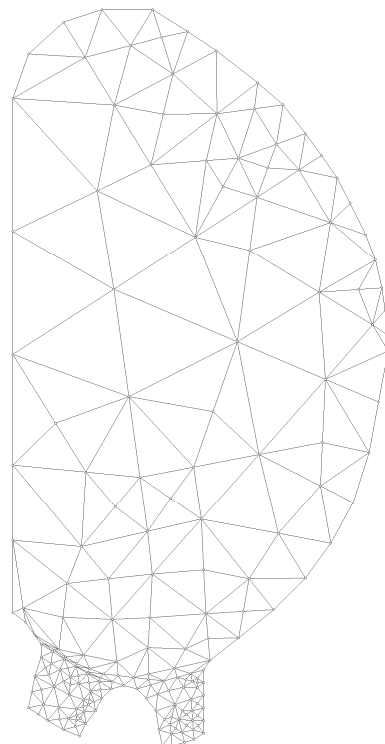
the centres of the triangles. The magnetic surfaces, which we call the 'layers', are assembled of line segments ending at the triangle sides. The function $w(\mathbf{p})$ between the corners is approximated by linear dependences. For example, along a triangle side ending at the positions $\mathbf{p}_a$ and $\mathbf{p}_b$ with $w(\mathbf{p}_a) = w_a$ and $w(\mathbf{p}_b) = w_b$ the positions $\mathbf{p}(w)$ are approximated as

$$\mathbf{p}(w) = \mathbf{p}_a + \frac{w - w_a}{w_b - w_a}(\mathbf{p}_b - \mathbf{p}_a) \tag{8.1}$$

For a given set of monotonically rising contour values $\{w_k\} = (w_0, w_1, w_2, \dots)$ the line segments are built inside each triangle based on Eq.(1) for $w = w_k$ and then the corresponding set of contours created. Fig.1 demonstrates the contours built on the triangles of Fig.2 for some typical currents.

The behaviour of the function $w(\mathbf{p})$ is generally not trivial. Monotonic change of w reproaching the magnetic axis (r_0, z_0) at the central region is not longer valid outside the separatrix where the contours cease to be closed inside the vessel. Due to influence of the poloidal field coils there are several regions of monotonic decrease or increase of $w(\mathbf{p})$ approaching the wall surface. The relations between the neighbour regions are described in TOKES by a graph of layer images Ref.[10], which demonstrates Fig.3 for the contours of Fig.1. The connections between the neighbouring items of the graph (the magnetic layers) are defined according to their mutual locations: one layer can connect as only one or two of its neighbour layers as a larger number of neighbours, like the layer near the separatrix in Fig.1. One advantage of the modelling with the graphs is the natural possibility to calculate configurations with several magnetic islands, which are sub-domains of the confinement plasma around several local magnetic axes, i.e. around local minimums and maximums of $w(\mathbf{p})$ inside the vessel. (In Fig.1 there is only one 'magnetic island', which is the whole confinement region.) The implementation of graph structure is considered in Sec.10.

Fig. 8.3 The graph of magnetic layers

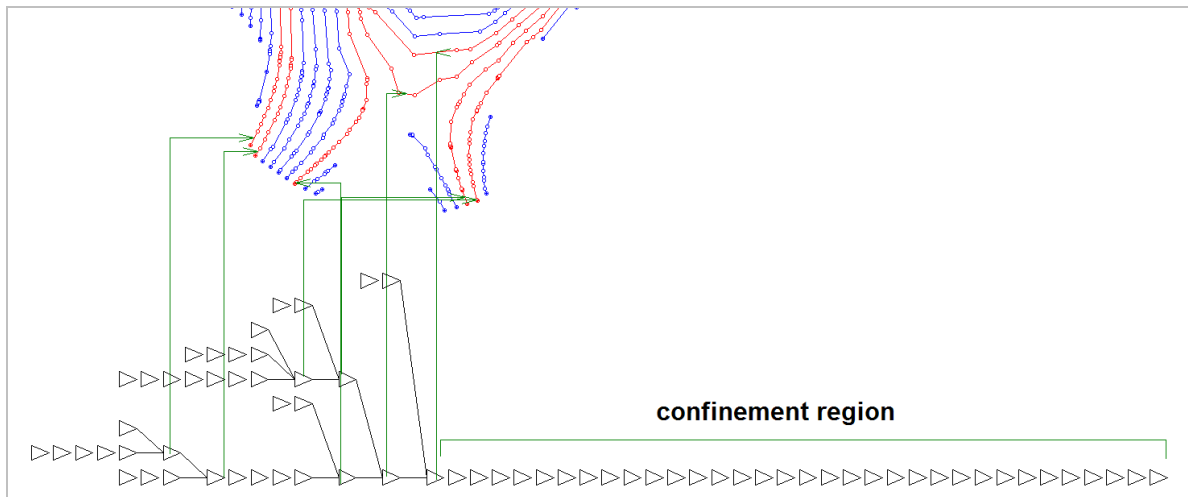The confined hot plasma of central region diffuses into different periphery regions. In a normal confinement regime the main surface exposure by the plasma is localized at the open layers most closed to the separatrix layer, but if some transient processes develop the other layers can transport substantial power to the other parts of the surface. Thus generally the distribution of plasma flux over the vessel surface can get rather complex. Plasma transport algorithms of TOKES are adjusted to the graph structure of layers and these processes are adequately considered in the general configuration.

The magnetic layers are 'homes' for the plasma, both on closed layers and the layers ending at the vessel surface. Therefore we often refer the magnetic layers as plasma layers. In this sense, the 'homes' for neutrals are the triangles (i.e. toroidal cells of triangle cross-section). The neutrals can be emitted from the surface by the sputtering and the vaporization as the consequence of plasma load onto the wall surface. Before coming into the central region the neutral atoms simulated by TOKES cross the periphery regions as toroidally symmetric 'rays' which travel across the vessel, triangle by triangle (the particle-in-cell numerical method) Ref.[11]. In SOL the emitted atoms meet the lost plasma which ionises them, fully or partially. A part of neutrals can cross SOL and reach the confinement region, where they are finally ionized.

Each segment of a magnetic layer is prescribed by its surrounding area s (on the poloidal plane) which is a part of the area of its host triangle calculated to be proportional to the length of the triangle's segments $\mathbf{l}_i$: $s = k|\mathbf{l}_i|$. The total area of all segments $\mathbf{l}_0$, $\mathbf{l}_1$ .. $\mathbf{l}_I$ crossing the triangle is equal to the triangle's area S, so that for the common coefficient k we have $k = S/\sum_i|\mathbf{l}_i|$. Obviously not all small triangles in the bottom part of Fig.1 are crossed by the layers. In those cases with no segment crossing a triangle, the whole area of such 'empty' triangle is prescribed to one nearby layer segment.

Each segment $\mathbf{l}_i$ of a layer is interpreted as a rectangle oriented along the segment, with some sizes a_i and b_i ($a_i b_i = s_i$). The side a_i (parallel to the segment) is initially assumed to be equal to $|\mathbf{l}_i|$. The code keeps it when a_i is obtained (with given s_i) larger than b_i, otherwise $a_i = b_i = \sqrt{s_i}$ is assigned. The layer may be interpreted as a chain of such rectangles. The plasma in the vessel is assumed to fill these rectangles only (i.e. the toroidal cells associated with the rectangles as the poloidal cross-section). The rectangles of the magnetic layer segments are demonstrated in Fig.4. As to the neutral fluxes, they are described most conveniently in terms of the triangular grid, and diverse neutral-plasma interaction rates in a triangle cell are assumed to be proportional to the volumes of the enclosed plasma cells.

The toroidal plasma currents are calculated at each plasma cell centre (e.g. according to the Ohm's law). Then in each triangle crossed by the layer segments the calculated enclosed currents are summed and the result I_t is assumed to be one current ring at the centre of the triangle (the index t counts the triangles). The currents of external PF coils I_n are designated with the index n. The triangle corner poloidal fluxes are calculated with Eq.(2.10) for the current rings at the triangle corner positions $\mathbf{p}_t^{(c)}$:

$$w(\mathbf{p}) = \sum_n I_n G(\mathbf{p}, \mathbf{P}_n) + \sum_t I_t G(\mathbf{p}, \mathbf{p}_t^{(c)}) \qquad (8.2)$$

In analytical form the plasma current density is given by Eq.(2.6). For the numerical implementation the differentiations and integrations of that formula are replaced by the finite-differences and the sums. As the result the current through a plasma cell i reads

$$I_i = \frac{cs_i}{\Delta w}\left(\frac{1}{r_i^{(c)}}\frac{\Delta\omega^2}{8\pi} + r_i^{(c)}\Delta p\right) \qquad (8.3)$$

Here $r_i^{(c)}$ is rectangle centre radius, $\omega = rB_\zeta$ the toroidal magnetic field contravariant component and p plasma pressure in the plasma cell. The difference $\Delta w = \Delta w_k$ (as well as Δp and $\Delta\omega^2$) is calculated taking the mean value (weighted on the connection area) of the difference between the layer and its neighbour layers l and r from its left and right sides as

Fig. 8.4 Rectangles of magnetic layer segments

$$\Delta w_k = \frac{(\Delta w_{kl})^2 + (\Delta w_{rk})^2}{\Delta w_{kl} + \Delta w_{rk}} \qquad (8.4)$$

Here $\Delta w_{kl} = w_k - w_l$ and $\Delta w_{rk} = w_r - w_k$, with w_k, w_l and w_r the values of the set $\{w_k\}$ over the plasma layers. For a layer that has only one neighbour (as one at the magnetic axis or first one at the wall surface), for instance from the left side, Eq.(4) is simplified as $\Delta w_k = w_{kl}$.

Smoothing of plasma currents: The unit current in a point $\mathbf{P} = (R,Z)$ that defines the poloidal magnetic flux at every point $\mathbf{p} = (r,z) \neq \mathbf{P}$ by means of the Green function $G(\mathbf{p},\mathbf{P})$ Eq.(2.8) has a singular current density which is infinite at $\mathbf{p} = \mathbf{P}$ and equals zero at other points (the Dirac's δ-function). Therefore the function $G(\mathbf{p},\mathbf{P})$ tries to infinity at $\mathbf{p} \to \mathbf{P}$, which
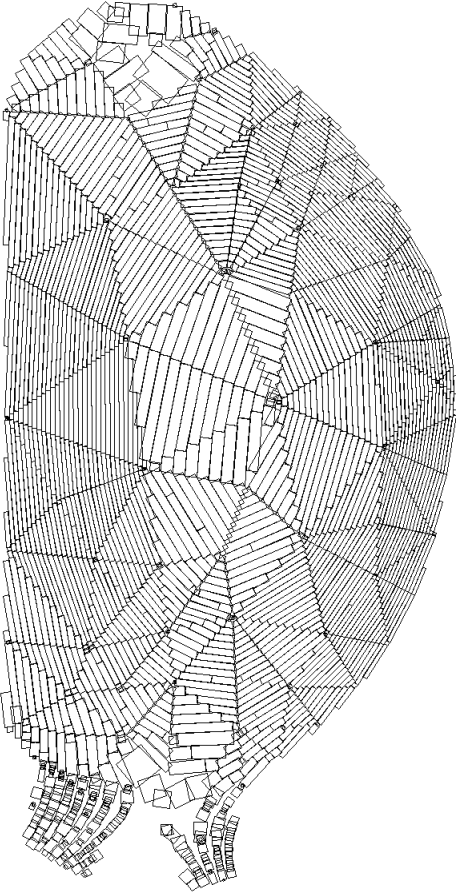
produces some inconveniences. For example, to present the magnetic surfaces we draw contours of poloidal magnetic flux $w(\mathbf{p}) = w_0$ at some constant w_0 that can pass nearby of $\mathbf{P}$. Then one would see a not acceptable numerical effect of bypassing around triangle centres.

Therefore some "smoothing" of $G(\mathbf{p},\mathbf{P})$ in vicinity of $\mathbf{P}$ is desirable. This is achieved by a slight modification of the parameter k given by Eq.(2.9). The singularity appears at $k^2 \to 1$ (at $z \to Z$ and $r \to R$). To avoid the singularity we use the modified parameter

$$k_{\mathrm{mod}}^2 = \frac{4rR}{(r+R)^2 + (z-Z)^2 + 4\varepsilon R^2} \qquad (0 < \varepsilon \ll 1) \qquad (8.5)$$

At $r = R$ and $z = Z$ we have $k_{\mathrm{mod}} = (1+\varepsilon)^{-1/2} < 1$, which eliminates the singularity. The value of the dimensionless parameter ε should be chosen individually for each current. For instance, it can correspond to the poloidal cross-section thickness of PF coil or to the size of a numerical cell's poloidal cross-section. For such a specific size ρ we choose $\varepsilon = \rho/R$, and we assume the inequality $\rho \ll R$, so that ε is small ($\varepsilon \ll 1$). The value of ρ is assumed to depend on the poloidal distance $d = \sqrt{((r-R)^2+(z-Z)^2)}$ between the points $\mathbf{p}$ and $\mathbf{P}$, reaching its maximum at $\mathbf{p} = \mathbf{P}$ and vanishing at $\rho \ll d \ll R$. The dependence on d is defined using the Gaussian function: $\rho(d) = \rho_0 \exp\left(-2d^2/\rho_0^2\right)$, with ρ_0 triangle cell size (for the plasma currents) or the coil thickness. The resulting magnetic field $\mathbf{B}(r,z)$ corresponds to some continuous current distribution $\mathbf{J}(r,z)$ localized near the point $\mathbf{P}$, the calculation of which from the Maxwell's equation $\nabla \times \mathbf{B} = (4\pi/c)\mathbf{J}$ is not necessary. Thus, at the large distances $d \gg \rho_0$ the magnetic field seems being produced by the singular unit current at the point $\mathbf{P}$, and at the small distances $d \sim \rho_0$ the smoothed current distribution becomes conspicuous.

9. Plasma shape control

The configurations of desirable plasma shapes are produced calculating as the plasma currents in each triangle, I_i, as suitable currents in the external PF coils, I_n. To calculate the PF coil currents, one should impose some constraints to the poloidal magnetic field. For example, we can assume that some magnetic field line outside the plasma should cross several given control points $\mathbf{p}_m = (r_m, z_m)$, each of which corresponds to the different coil m. As the magnetic flux w is constant along the field line, expressing $w(\mathbf{p}_m)$ in terms of I_i and I_n with Eq.(8.2) gives the number of equations equal to the number of coil currents, which allows to obtain I_n at fixed I_i. After each calculation of I_n the magnetic field is fixed, which means that I_i and I_n

remain intact until other sub-steps such as the plasma transport sub-step and the heating sub-step are done for the next time step Δt. Those sub-steps allow updating I_i, and then we calculate I_n again.

So far, in TOKES we assume that the full plasma current $I_p = \sum_i I_i$ and the coils positions $\mathbf{P}_n$ are fixed. The coils current I_n for the system of 6 coils of ITER are obtained with the conditions: 1) a given set of plasma currents I_i, 2) two x-points ("a-point" and "b-point") at given positions $\mathbf{p}_a$ and $\mathbf{p}_b = (r_b, z_b)$, 3) the (poloidal) magnetic field $\mathbf{B}$ to be vertical ($B_r = 0$) at some given position $\mathbf{p}_c$, 4) the separatrix through the b-point to cross some given positions $\mathbf{p}_d$ and $\mathbf{p}_e$, and 5) the difference between the poloidal magnetic fluxes w_a and w_b at the points $\mathbf{p}_a$ and $\mathbf{p}_b$ is given: $w_a - w_b = \Delta w$. For instance, the a-point is the x-point of the separatrix bounding the confinement plasma and the b-point the x-point of some outer separatrix. In this case the points $\mathbf{p}_d$ and $\mathbf{p}_e$ may control the crosses of outer separatrix with the main chamber wall in order to keep the plasma at some distance from the wall, and the point $\mathbf{p}_c$ enables to adjust vessel surface to plasma edge at maximum radius r of plasma.

Thus calculating I_n, the plasma currents I_i are assumed known and expressed in terms of total plasma current I_p with the factors f_i normalized on 1 ($\sum_i f_i = 1$), so that Eq.(8.2) reads:

$$w(\mathbf{p}) = \sum_n I_n G(\mathbf{p}, \mathbf{P}_n) + I_p G_p(\mathbf{p}), \qquad G_p(\mathbf{p}) = \sum_i f_i G(\mathbf{p}, \mathbf{p}_i^{(c)}) \qquad (9.1)$$

The coils positions $\mathbf{P}_n$ and I_p are assumed fixed. The mentioned set of constraints produces 8 equations, which allows obtaining all six coil currents I_n and also the b-point coordinates, r_b and z_b. At the a-point and the b-point both components (B_r and B_z) of poloidal magnetic field vanish, and the point $\mathbf{p}_c$ only B_r vanishes:

$$B_r(\mathbf{p}_a) = \sum_n I_n G_r(\mathbf{p}_a, \mathbf{P}_n) + I_p G_{rp}(\mathbf{p}_a) = 0 \qquad (9.2)$$

$$B_z(\mathbf{p}_a) = \sum_n I_n G_z(\mathbf{p}_a, \mathbf{P}_n) + I_p G_{zp}(\mathbf{p}_a) = 0 \qquad (9.3)$$

$$B_r(\mathbf{p}_b) = \sum_n I_n G_r(\mathbf{p}_b, \mathbf{P}_n) + I_p G_{rp}(\mathbf{p}_b) = 0 \qquad (9.4)$$

$$B_z(\mathbf{p}_b) = \sum_n I_n G_z(\mathbf{p}_b, \mathbf{P}_n) + I_p G_{zp}(\mathbf{p}_b) = 0 \qquad (9.5)$$

$$B_r(\mathbf{p}_c) = \sum_n I_n G_r(\mathbf{p}_c, \mathbf{P}_n) + I_p G_{zp}(\mathbf{p}_c) = 0 \qquad (9.6)$$

$$G_{rp}(\mathbf{p}) = \sum_i f_i G_r(\mathbf{p}, \mathbf{p}_i^{(c)}), \qquad G_{zp}(\mathbf{p}) = \sum_i f_i G_z(\mathbf{p}, \mathbf{p}_i^{(c)}) \qquad (9.7)$$

Another way of keeping the plasma at a distance from the walls combined with minimization of maximum current of PF coils is as follows. We fix the x-point position $\mathbf{p}_a$. After each time step a boundary maximum $\mathbf{p}_m$ of minimum difference $\Delta w = w(\mathbf{p}_a) - w(\mathbf{p}_m)$

among the boundary maximums is determined. We require $w(\mathbf{p}_m)$ to be equal to a given value $\Delta w_{\min}$. Thus, 3 of 6 equations for I_n are set. Let's assume the maximum current obtained at the previous step is at $n = l$. The last 3 equations are obtained aiming at minimizing I_i varying the right hand side in the equations:

$$B_r(\mathbf{p}_a) = \sum_n I_n G_r(\mathbf{p}_a, \mathbf{P}_n) + I_p G_{rp}(\mathbf{p}_a) = 0 \tag{9.8}$$

$$B_z(\mathbf{p}_a) = \sum_n I_n G_z(\mathbf{p}_a, \mathbf{P}_n) + I_p G_{zp}(\mathbf{p}_a) = 0 \tag{9.9}$$

$$\sum_n I_n G(\mathbf{p}_j, \mathbf{P}_n) + I_p G_p(\mathbf{p}_j) = \min(w_j, w_a - \Delta w_{\min}), \quad j = 1..4 \tag{9.10}$$

In the code those schemes are implemented in various ways, see also Ref.[12].

10. Graph structure of magnetic layers with the x-points

As mentioned in Sec.8, in TOKES the magnetic layers are produced from the segments enclosed in the triangles. The segments were created independently for a set of contour values $\{w_k\}$. Inside each triangle the enclosed segments are ordered as an array with increasing w_k. Initially the segments are not marked as those belonging to some layers. Cycling over the triangles, the code finds first a not marked segment. This is the starting segment of first layer to be produced. The code marks this segment with the initial layer index $l = 0$ and looks across the triangle sides of segment's ends in the neighbour triangles for the adjoining not marked segments of the same value w_k. If the triangle side is a wall face, then the segment is the end segment of the layer, so that in that direction the building of the layer is finished. Otherwise the segments of the value w_k are found. The new segments are also marked with $l = 0$ and the layer building continues in such way in both direction until meeting the wall faces or again the marked segment, which means looped (i.e. closed) layer. Then the code cycles again over the triangles, finds first not marked segment, indexes it with $l = 1$ and repeats the same procedure building the next layer for the value $w_{k'}$ of its segments (it can be that $w_{k'} = w_k$ at some different l). Finally all segments become organized as the components of the magnetic layers.

Before building the graph structure of the layers, each layer segment looks for its two neighbours in the triangle the segment belongs to. If there are those neighbours from both sides of the segment, their layers become the neighbours of the segment's layer (and vice versa). If the segment is the first or the last one of the array of triangle's segments, the code

tries to recognize its appropriate neighbour in neighbour triangles. If the wall face is met, it means that the segment does not have a neighbour in that direction. Finally all segments get prescribed with two or one, or no one ('nil') neighbours.

By this way each layer acquires the neighbour layers. If a layer did not get neighbour layers ('single' layer) it is excluded from the graph structure (TOKES did not meet this case so far but it can be possible at some complex shape of the vessel boundary and some rare set $\{w_k\}$). Then the code cycles over the layers until finding first layer that has only one neighbour layer; the found layer is considered as a 'childless' layer. The neighbour layer is marked as its parent (the 'dad') and the layer itself is marked as a 'son' of neighbour layer. The 'dad' layer can have a list of one, two or more neighbours (one is the mentioned 'son'). The 'son' is immediately moved from the neighbour list and attached to the dad as the graph item. If only that 'son' was in the list, the 'dad' is classified as the 'origin' layer and is added to a special list of origin layers of the graph (initially that list is empty) and the code starts again cycling over not yet marked layers repeating the procedure.

If (after excluding the 'son') the 'dad' has only one neighbour, that one is in turn considered as its 'dad'. Thus a linear chain of layers starts to be built as a part of the graph under creation, so that the first 'dad' is the 'son' of the second 'dad' etc. If the list of remaining 'dad' neighbours has more than one layer, only one of them may be considered as the next 'dad'. One of them could already be marked as the 'dad' in some earlier cycling over the layers, but if not yet, the first remaining neighbour is marked as the next 'dad' and the other neighbours as the other 'sons' of the previous 'dad'.

This process is organized as a procedure that repeats such finding of not yet excluded sons until the complete building of the graph structure. As the result, all 'dads' and 'sons' find properly each other and finally form a list of graphs each of them starts from different 'origin' layers. It is to note that in our practice we met one origin layer only and thus used to build one graph structures so far.

As the result, the magnetic surfaces in a toroidal vessel are ordered as some regions of monotonic behaviour of poloidal magnetic flux $w(\mathbf{p})$ on the poloidal plane. Those regions are separated by means of either saddle points or some of minimums and maximums of w on the boundaries. In the numerical scheme with triangular meshes the boundary extremes are selected considering each three sequential nodes a, b and c along the boundary: e.g. a boundary node b is a maximum-node if $w(\mathbf{p}_b) > w(\mathbf{p}_a)$ and $w(\mathbf{p}_b) > w(\mathbf{p}_c)$.

For inner extremes: maximums, minimums and saddle points (the latter are called in TOKES the x-points if locate at the edge of a plasma confinement region) the following

definitions are used. An inner node i (see Fig.1) is the maximum node or the minimum node when for all neighbour nodes j ($j = 0..J$) the inequalities $w(\mathbf{p}_i) > w(\mathbf{p}_j)$ or $w(\mathbf{p}_i) < w(\mathbf{p}_j)$ are met, respectively. The 'plateau' centres are excluded (the nodes with $w(\mathbf{p}_i) = w(\mathbf{p}_j)$ for all j)

because we consider them as 'pathological' cases not be met, as well as any plateau triangles.
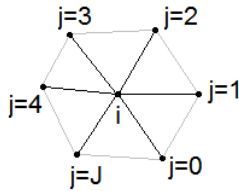
Fig. 10.1 Vicinity of inner triangle node

The saddle nodes are selected as follows, initially excluding the nodes of minimums and the maximums from the consideration. The values of $w(\mathbf{p}_j)$ are compared with $w(\mathbf{p}_i)$ starting from $j = 0$. The node of $j = 0$ and the direction of i-node traversal are chosen so that $w(\mathbf{p}_J) \leq w(\mathbf{p}_i)$ and $w(\mathbf{p}_0) > w(\mathbf{p}_i)$. At $j = 0..j_1$ (j_1 is some index less than J) all $w(\mathbf{p}_j) > w(\mathbf{p}_i)$, then at $j = j_1+1..j_2$ all $w(\mathbf{p}_j) \leq w(\mathbf{p}_i)$. If $j_2 < J$ and $w(\mathbf{p}_j) > w(\mathbf{p}_i)$ at $j = j_2 + 1$, the i-node is the saddle node. If $j_2 = J$, the i-node is a 'simple' node.

The inner minimums and maximums determine the centres of the regions that can confine the plasma (the magnetic axes). A boundary maximum or boundary minimum can be an x-point which separates a confined plasma region from the outer regions when the plasma touches the wall. (In the outer regions the magnetic layers are not looped in the poloidal plane inside the vessel, because they end at the wall surface).

There are evident situations when one can conclude that the boundary extreme cannot be an x-point. For example, in Fig.2 (left) the i−node is a boundary extreme node and the magnetic layer contours "try to surround" it, thus indicating the i-node is the maximum (or minimum) of $w(\mathbf{p})$ in the vicinity determined by the triangles the i-node belongs to. A boundary node can be treated like an inner one imagining a closing side that connects the nodes $j = 0$ and $j = J$ (the dashed line on the left part of Fig.2) and linearly changing $w(l)$ along its length coordinate l from $w(\mathbf{p}_0)$ to $w(\mathbf{p}_J)$.
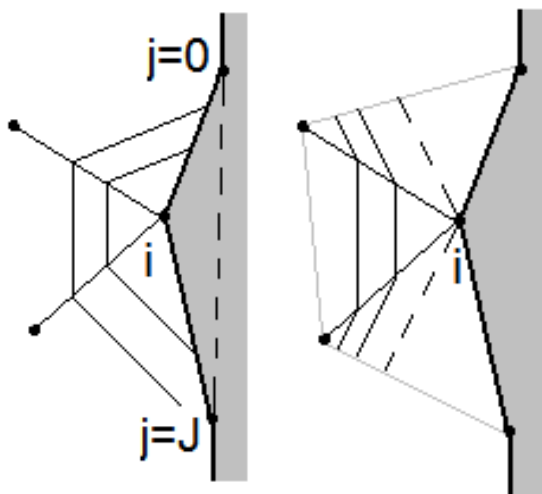
Fig. 10.2. Left: Local maximum at a boundary node. Right: A saddle at a boundary node

To comment another example let the i-node in Fig.2 to be a boundary maximum. Then from the drawn contours w=const it is obvious that all $w(\mathbf{p}_j)$ of the left part are smaller than $w(\mathbf{p}_i)$ and w of the inner nodes of the right part are larger than $w(\mathbf{p}_i)$. The dashed lines on the right part of Fig.2 can belong to the edge of

confinement region if the corresponding contour $w(\mathbf{p}) = w(\mathbf{p}_i)$ is a loop. As the next example produced with TOKES, Fig.3 shows the layer contours $w(\mathbf{p}) = w_k$ on the ITER poloidal plane and the extremes.
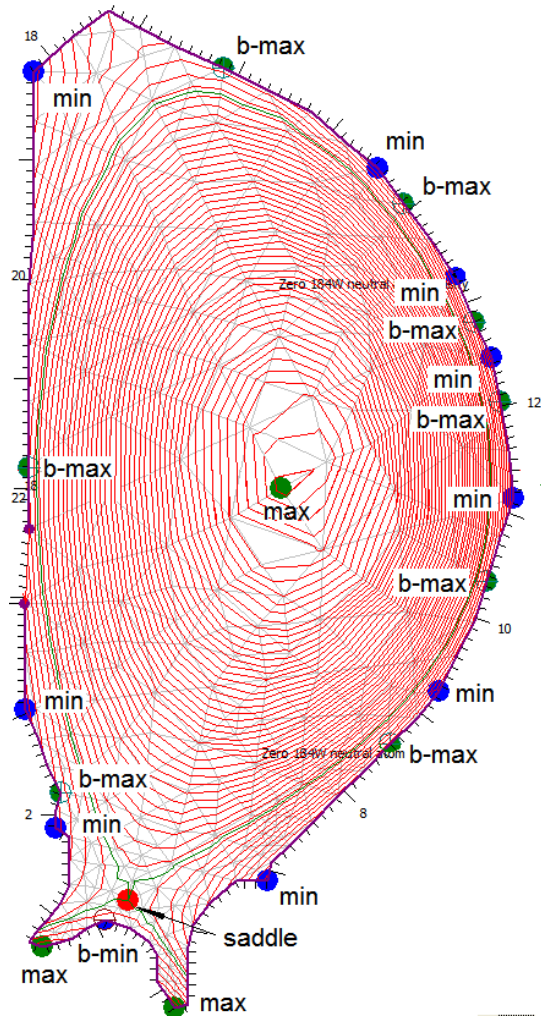
Fig. 10.3 Locations of extreme points in ITER magnetic configuration

The graph structure of discrete magnetic layers of TOKES allows us to separate accurately the last closed layer (the 'c-layer') from one or several unclosed layers (the 'u-layers') for arbitrary magnetic configuration. Up to now TOKES worked only with one confinement region therefore we describe below only this case. After each time step the cross-transport produces the plasma to be dumped across some separatrix into SOL. This plasma is initially accumulated in a special buffer prescribed to the available x-point. Now we explain how the x-point is chosen and how the buffer distributes the dump for SOL.

We assume that the interface between the c-layer (with the magnetic flux $w = w_c$) and the u-layers ($w = w_u$) contains one magnetic surface that separates continuously nested closed contours $w(\mathbf{p}) = \text{const}$ from the unclosed ones. The separatrix crosses either an inner x-point or a boundary extreme which we consider then also as an x-point. Generally many possible cases can be met, in particular with several x-points at one separatrix (for instance the double-null configuration or an inner-and-boundary x-point configuration). To recognize the case, the code chooses among all saddle points only those ones the values w_s of which belong to the interval: $w_u < w_s < w_c$ (here we assumed $w_u < w_c$). If the code found only one such saddle, it is the x-point and nothing to do more. With two saddles inside the interval, the saddle of minimum difference $\Delta w = w_c - w_s$ is considered as the x-point. Larger numbers of saddles inside the interval we did not meet so far.

The obtained w_s allows building the separatrix contour $w(\mathbf{p}) = w_s$. The separatrix consists of the segments like that of the magnetic layers. Thus the triangles crossed by the separatrix become available. Then, the accumulated plasma dump is distributed over these

triangles proportionally to the poloidal length of the triangle's segments of separatrix contour. To save the obtained plasma for further processing, in each triangle a special data structure S containing some buffer $B_S = (N_S, E_S)$ for plasma particles N and their energy E is foreseen, and the value of w_s is also saved in S. If the separatrix has crossed the particular triangle for first time, the structure S is created. If after further processing the buffer B_S got emptied, S is deleted. By this way in the course of tokamak operation only necessary structures S are maintained, which traces the evolving scrape-off layer.

After each time step the value of w_s can change. Also the complete magnetic configuration, including the topology of magnetic surfaces (i.e. the entire graph) can change significantly, even after one time step. However, if the damp after a time step of some duration τ has anyhow repeated into the same triangle, it is added to the buffer and w_s is updated. The previous value of w_s, w_{pred}, is also saved in the structure S. (Having w_{pred} the speed of w_s across the adjoining closed magnetic layer can be estimated as $dw/dt = (w_s - w_{\text{pred}})/\tau$.)

If the difference $|w_c - w_s|$ gets smaller than $|w_c - w_{\text{pred}}|$, the following happens. Due to the movement of separatrix location along the magnetic flux coordinate w a part of plasma is additionally dumped from the last closed layer into the triangle's buffer B_S. This sub-step is introduced in order to distribute the dump over many time steps and thus decrease large perturbations to dumped flux when the closed layer gets unclosed after some time step. The respective dump amount ΔB_S is proportional to the fraction $\varepsilon = \min(1, |w_0 - w_{\text{pred}}|/|\Delta w|)$ where Δw is the difference of magnetic coordinates of the layers c and u: $\Delta B_S = \varepsilon B_p$, with B_p the amount of plasma in the c-layer's fragment located in front of the triangle's segment of the separatrix contour $w(\mathbf{p}) = w_s$.

The calculation of B_p is some fragment of TOKES algorithm not discussed here. It is also to note that the closed layer behaves so as it would not lose the plasma due to the separatrix movement. The amount of lost plasma is nevertheless saved in layer data and if the layer gets unclosed, only the remaining (usually small) plasma amount is dumped onto the wall. Anyway the whole plasma energy and particle number keep constant after those calculation steps.

This way seems promising. For example, when in our simulations the plasma is initially confined having an inner x-point, but during the operation the plasma shape evolves so that at some time moment the inner x-point transforms into a boundary x-point (the latter x-point has a quite different location than the former one) we see that the code 'survives' this transition and continues running, with the plasma contacting the wall (as it does in the limiter

tokamaks). At later time the reversed transition can happen, thus TOKES allows rather realistic simulations of toroidally symmetric tokamak configurations.

11. Modelling of diffusion equation on the graph

One-dimensional plasma transport described with Eq.(5.6), Eq.(5.15) and Eq.(5.20) is simulated for a large number of time steps of duration τ on some discrete set of increasing values of the magnetic flux coordinate x. Generally, in finite-difference equations τ and the coordinates may vary through the sequence of calculation steps. However, in TOKES only the time step τ can vary arbitrarily. Over one region of monotonic increase of w, the x-width of the magnetic layers , $\Delta_k = x_{k+1/2} - x_{k-1/2}$ is fixed ($k = 0..K-1$, with K the number of layers in the region). The integer index k means that the value corresponds to the magnetic layer itself. The half-integer index $k\pm1/2$ means the mean value: for some function, a_k, we have $a_{k+1/2} = (a_{k+1} + a_k)/2$. In particular, x can be the index-coordinate of the layers ($\Delta = 1$). The layer 'width' on the poloidal magnetic flux, $\Delta w_k = w_{k+1/2} - w_{k-1/2}$, can vary.

On one time step, the numerical solving of the equations is split into a number of sub-steps each of which deals with only some different terms of the bulky expressions, using the result of previous sub-step as an initial condition (the splitting method). So that the results after the whole time step is a composition of the results of the sub-steps for the same duration, τ, over all terms of the equations. It is to note that one split-off equation contain some several terms of the original equation, and the time derivative term repeats in all split-off equations.

The sub-steps for the processes of diffusion or thermal conduction can be calculated outgoing from the following generic equation:

$$\frac{\partial}{\partial t}(Gf) = \frac{\partial}{\partial x}\left(D\frac{\partial f}{\partial x}\right) + q - pf \tag{11.1}$$

Eq.(1) describes some diffusion process for the positive functions $f(t,x)$ (the 'density'), $G(t,x)$ (the 'volume'), $D(t,x)$ (the 'diffusivity'), $p(t,x) \geq 0$ (the 'sink frequency') and $q(t,x) \geq 0$ (the 'source'). The particular meaning of terms depends on the context: for example, the coefficient D can have the meaning of thermal conductivity, and f can be a temperature.

Initially we consider only one region of increasing the values of w. In this case the following implicit scheme that is stable at arbitrary τ and Δ is chosen for Eq.(1):

$$\frac{G_k f_k - \widehat{G}_k \widehat{f}_k}{\tau} = \frac{1}{\Delta^2}\left(\widehat{D}_{k+1/2}\left(f_{k+1} - f_k\right) - \widehat{D}_{k-1/2}\left(f_k - f_{k-1}\right)\right) + \widehat{q}_k - \widehat{p}_k f_k \tag{11.2}$$

The values with the up-script '^' are known at the beginning of the sub-step, and f_k should be obtained as the result of sub-step. Eq.(2) is a set of linear algebraic equations for f_k which reduce to the standard system with the three-diagonal matrix:

$$-A_k f_{k-1} + \left(B_k + A_k + C_k\right) f_k - C_k f_{k+1} = F_k \tag{11.3}$$

$$A_k = \frac{\tau}{\Delta^2} \widehat{D}_{k-1/2}, \qquad C_k = \frac{\tau}{\Delta^2} \widehat{D}_{k+1/2}, \qquad A_0 = C_K = 0 \tag{11.4}$$

$$B_k = G_k + \tau \widehat{p}_k, \qquad F_k = \widehat{G}_k \widehat{f}_k + \tau \widehat{q}_k \tag{11.5}$$

Now we want to explain the TOKES algorithm of the solver to Eq.(3), which is some variant of the well known Gauss' method. This demonstration can be useful because it highlights also the TOKES algorithm of calculations on the graph structure of magnetic layers which follows below in this section. Furthermore, in Sec.19 we used a similar procedure for calculations of the populations of bound electron levels.

At first we give a simple example with only four unknown variables f_0, f_1, f_2 and f_3, of which f_0 and f_3 are some known boundary values. This example can convince the reader why the algorithms implemented in TOKES provide the stability and maximally possible accuracy for Eq.(2). Two equations to be solved are:

$$-A_1 f_0 + \left(B_1 + A_1 + C_1\right) f_1 - C_1 f_2 = F_1 \tag{11.6}$$

$$-A_2 f_1 + \left(B_2 + A_2 + C_2\right) f_2 = \overline{F}_2, \qquad \overline{F}_2 = F_2 + C_2 f_3 \tag{11.7}$$

The algorithm starts from Eq.(7). The coefficients B_2, C_2 and F_2 are renamed as $C_2 \equiv \overline{C}_2$. Then we express f_2 in terms of f_1:

$$f_2 = \frac{\overline{F}_2 + A_2 f_1}{\overline{B}_2 + A_2 + \overline{C}_2}, \tag{11.8}$$

It is to note that all terms here are positive and they are involved in the sums (no negative sign). Thus the numerator and the denominator are positive and they cannot be equal to zero. We substitute f_2 Eq.(8) into Eq.(6) and get the equation similar to Eq.(6), however with the smaller index and modified coefficients B_1, C_1 and F_1:

$$-A_1 f_0 + \left(\overline{B}_1 + A_1 + \overline{C}_1\right) f_1 = \overline{F}_1, \qquad \overline{B}_1 = B_1 + \frac{C_1 \overline{B}_2}{\overline{B}_2 + A_2 + \overline{C}_2} \tag{11.9}$$

$$\overline{F}_1 = F_1 + \frac{C_1 \overline{F}_2}{\overline{B}_2 + A_2 + \overline{C}_2}, \qquad \overline{C}_1 = \frac{C_1 \overline{C}_2}{\overline{B}_2 + A_2 + \overline{C}_2}, \tag{11.10}$$

If we would have larger number of those equations, this procedure could also be explained in the same way including obvious obtaining f_1 from Eq.(9). As we see, in this algorithm there is no room for appearance of negative contributions, which guarantees keeping f_k positive, as

well as stability and maximal accuracy of the calculations. After obtaining f_1 we sequentially obtain the other unknown f_k from the expressions like Eq.(8).

In the numerical scheme for magnetic layers described with the graph, each layer is associated generally to several child layers (we say its 'sons') and one parent layer (the 'dad' of the layer). One of the layers (the original layer) doesn't have a parent, and some of layers do not have children. The finite-difference scheme for Eq.(1) for the layer takes the form:

$$\frac{Gf - \widehat{G}\widehat{f}}{\tau} = \widehat{D}_d \left(f_d - f \right) + \sum_s \widehat{D}_s \left(f_s - f \right) + \widehat{q} - \widehat{p}f \tag{11.11}$$

The layer is not indexed and we assume $\Delta = 1$. The system Eq.(11) is rewritten like Eq.(6) as

$$-A_d f_d + \left(B + A_d + \sum_s A_s \right) f - \sum_s A_s f_s = F \tag{11.12}$$

The coefficients look like that of Eq.(4) and Eq.(5).

The solution to Eq.(12) is obtained as follows. Initially a childless layer ('end layer') is considered. For it Eq.(12) simplifies:

$$-A_d f_d + \left(B + A_d \right) f = F \tag{11.13}$$

The value f of the end layer is expressed in terms of f_d:

$$f = \frac{F + A_d f_d}{B + A_d} \tag{11.14}$$

For the next layer, which is the parent of the end layer, Eq.(12) keeps its form. The end layer is one of children and thus its f is one of f_s in the sum. We eliminate it from Eq.(12) using Eq.(14) (with the new designations $f \rightarrow f_s$, $B \rightarrow B_s$, $A_d \rightarrow A_s$, $f_d \rightarrow f$, $F \rightarrow F_s$):

$$f_s = \frac{F_s + A_s f}{B_s + A_s} \tag{11.15}$$

As the result, Eq.(12) acquires the similar form, however with one eliminated 'son' and modified coefficients:

$$-A_d f_d + \left(B + \overline{A}_d + \sum_{s' \neq s} A_{s'} \right) f - \sum_{s' \neq s} A_{s'} f_{s'} = \overline{F} \tag{11.16}$$

$$\overline{A}_d = A_d + \frac{A_s B_s}{B_s + A_s}, \qquad \overline{F} = F + \frac{F_s A_s}{B_s + A_s} \tag{11.17}$$

It is to note that if omitting the sums on s', Eq.(16) becomes similar to Eq.(13). If the sums in Eq.(16) really got empty (the case with only one 'son'), we conclude that the end layer's function f is eliminated and the next layer becomes playing the role of the end layer in the calculation procedure, however with the modified A_d and F. This procedure is then repeated until the layer with several children. As for it the sums on s' are not empty, we can perform

the same process at the ends of its other children's graphs. At each step the equations expressing the child values of f in terms of its parent values of f are obtained. Finally the sums are replaced with the corresponding modified coefficients and the layer which has several children becomes the end layer. The procedure is then repeated further until the original layer. Eq.(16) for it, with the sums replaced, reads

$$\left(B+\overline{A}_d\right)f=\overline{F} \qquad \Rightarrow \qquad f=\frac{\overline{F}}{B+\overline{A}_d} \tag{11.18}$$

Having obtained the last value the process is reversed in order to obtain all values of f using the available expressions for children's f in terms of their parents' f like Eq.(15), however with modified coefficients.

In the programming language Delphi, the algorithm that completes those calculations is rather short, consisting of two recursive procedures, first one (AssignAmSm) for obtaining the modified coefficients and the second (AssignF) for obtaining resulting values of f. (The above introduced names associate with the Delphi names as A → Am, F → Sm and f → F.)

```
procedure TLayer.AssignAmSm;
  var
    I: Integer;
    W: Real;
begin
  Dad.Core.Am := Dad.Core.A;
  Sm := S;
  for I := 0 to High(Son) do
  with Son[I].Core do
  begin
    Son[I].Associate.AssignAmSm;
    W := Son[I].Associate.B + Am;
    Dad.Core.Am := Dad.Core.Am + A * (1 - A / W);
    Sm := Sm + A * Son[I].Associate.Sm / W;
  end;
end;


procedure TLayer.AssignF;
  var
    I: Integer;
    SD: Real;
begin
  with Dad do
  if Associate <> nil then
    SD := Core.A * Associate.F
  else
    SD := 0;
  F := (SD + Sm) / (B + Dad.Core.Am);
  for I := 0 to High(Son) do
    Son[I].Associate.AssignF;
end;
```

The coefficients B, S and Sm (*S* modified) are the fields of a class TLayer. The coefficients A and Am (*A_d* modified) are the fields of a class TCore which represents the interface between a parent and one of its children. The mutual references of these associates (Son and Dad) are organized with a class TPair that has a TLayer field Associate and a TCore field Core. Each layer has an array Son of TPair instances and one TPair instance Dad. Initially the procedure AssignAmSm of the final layer is called, and it calls itself until all Am and Sm are calculated. Then the procedure AssignF of the final layer is called, and it calls also itself until all values of *f* are calculated. It is to note that these fragments of TOKES source file aim only at principal highlighting of implementation technique, and in the development process some of details may be improved.

In the algorithm simple boundary conditions with zeroed fluxes at the external boundaries of end layers (childless layers and the origin layer) are automatically valid. In the case of plasma that occupies the whole vessel this is the right choice. Indeed, the longitudinal outflow along the field lines is much larger than the cross-diffusion flow, and the longitudinal outflow is accounted for with the term *pf* in Eq.(1). Due to this term, *f(x)* drops drastically across the thin scrape-off layer from the value of *f* on the last closed layer. Outside SOL, *f* practically vanishes before approaching the wall surface. Furthermore, in TOKES also there is an option that allows the boundary condition at the edge of confinement region, which means some given value of *f* on the first unclosed layer outside the separatrix. This avoids the transport calculations with this algorithm across the vacuum part of the vessel, and then in SOL some other transport model can be applied, e.g. the kinetic model of Sec.27.

12. Testing for magnetic layers and diffusion algorithm
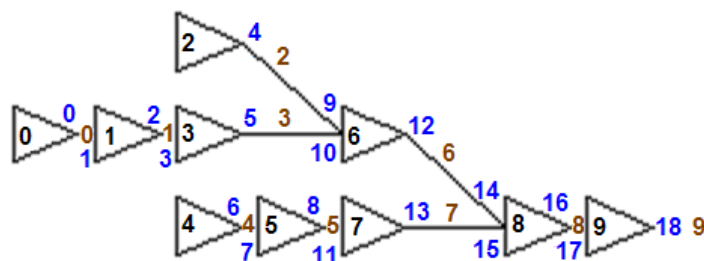
Fig. 12.1 A small graph. The triangles are layer images, with layer indices inside. The integers between the triangles and in the middle of connecting segments are core indices. The other integers near the triangles are pair indices.

The diffusion algorithm described in Sec.11 was tested in several different ways. At first, the function *f* for a small fragment of the graph of Fig.8.3 was calculated using a standard algorithm by Gauss for the system Eq.(11.12) applying some parameters *B*, *A* and *F* and then

compared with the corresponding TOKES calculations. It is to note that the standard solver cannot provide acceptable computation performance for practically needed numbers of magnetic layers, but for a few layers the comparison is also convincing.

Exactly equal results in both cases are obtained. In the test the parameters B for all layers are chosen to be equal to the layer index on Fig.1 plus 1. The parameters $A = 1$ and $F = 1$ for all cores and layers are chosen, but in the core between the final parent and its not existing parent $A = 0$ was assigned. Table 1 represents the matrix of the linear system of equations solved by the Gauss method. In this case, for instance, $f_0 = 0.754220739$ and $f_9 = 0.101503922$ were obtained with both methods.

Table 12.1 The matrix of interactions among the layers (according to Fig. 1). The top row indicates the layer indices and at last denotes the column of coefficient F.

0	1	2	3	4	5	6	7	8	9	S
2	-1	0	0	0	0	0	0	0	0	1
-1	4	0	-1	0	0	0	0	0	0	1
0	0	4	0	0	0	-1	0	0	0	1
0	-1	0	6	0	0	-1	0	0	0	1
0	0	0	0	6	-1	0	0	0	0	1
0	0	0	0	-1	8	0	-1	0	0	1
0	0	-1	-1	0	0	10	0	-1	0	1
0	0	0	0	0	-1	0	10	-1	0	1
0	0	0	0	0	0	-1	-1	12	-1	1
0	0	0	0	0	0	0	0	-1	11	1
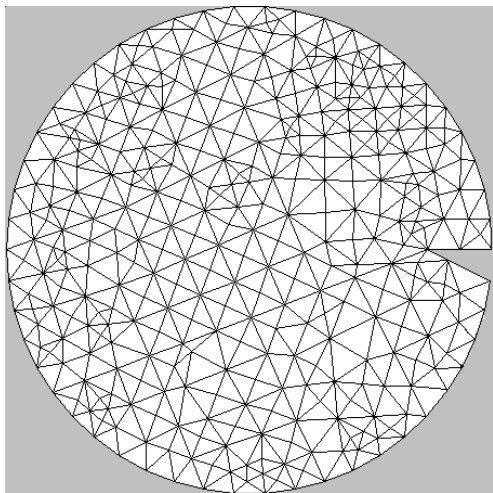
Fig. 12.2 Grid of triangles for testing the TOKES. The limiter ("tooth") is seen at the right side.

As the second test, calculations using the graph diffusion algorithm have been performed for a simple configuration that allows independent analytical check of results. One simple case that TOKES can model without degeneration of its major features is an imaginary tokamak device of approximately circular poloidal vessel's shape and circular magnetic surfaces, which implies a huge major radius. However, other tokamak parameters we keep like those of the project ITER-FEAT.

The toroidal surface minor radius is chosen to be 3 m. The poloidal cross-section of the surface is approximated with many equal linear segments, including a "tooth" that simulates the limiter, and then the triangular grid was automatically produced (see Fig.2). The limiter size of 0.8 m determines the minor plasma radius a be equal 2.2 m. The toroidal currents corresponding to the whole current $I = 15$ MA have been then produced at the centres of triangles over the region where the plasma is expected (and no currents in the other triangles)
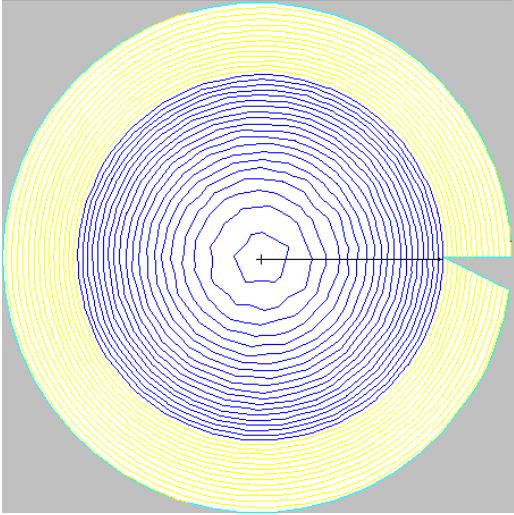
Fig. 12.3 Plasma region on the layers. The plasma occupies 20 of 34 layers

assuming equal current density over the triangles. The huge major radius $r_0 = 1$ km is chosen and the magnetic layers are generated that appeared having approximately circular poloidal shapes (see Fig.3), The large aspect ratio $r_0/a \approx 455$ makes toroidal aberrations in the poloidal plane not visible and allows simplification of Eq.(5.6) to be solved independently of the code and then compared with it. The toroidal magnetic field $B_\zeta = 5.3$ T becomes almost homogeneous over the vessel volume. The deuterium or, alternatively, helium plasma of ion temperature 10 keV and density 10^{20} m^{-3} was created on the closed magnetic layers. The step of poloidal flux Δw, which is fixed across the magnetic layers, was adjusted so that 20 layers contain the plasma.

The analytical diffusion equation for the plasma density n acquires the form:

$$\frac{\partial n}{\partial t} = \frac{1}{r}\frac{\partial}{\partial r}\left(rD\frac{\partial n}{\partial r}\right) + v_0 n(0) \tag{12.1}$$

Here r is the minor radius ($0 \leq r \leq a$) and v_0 fuelling frequency. Three different diffusion coefficients were checked: the 'classical' ($D \propto n$), the Bohm's ($D = $ const) and some artificial one ($D \propto n^2$). Eq.(1) was solved analytically and compared with corresponding TOKES calculations for the function $n(r)$. Here we omit the details of the analytical calculations and present only the comparisons. We assume that the temperature is constant in the plasma volume. The results of comparison are presented on the Fig.4 showing a good agreement of numerical and analytical approaches.
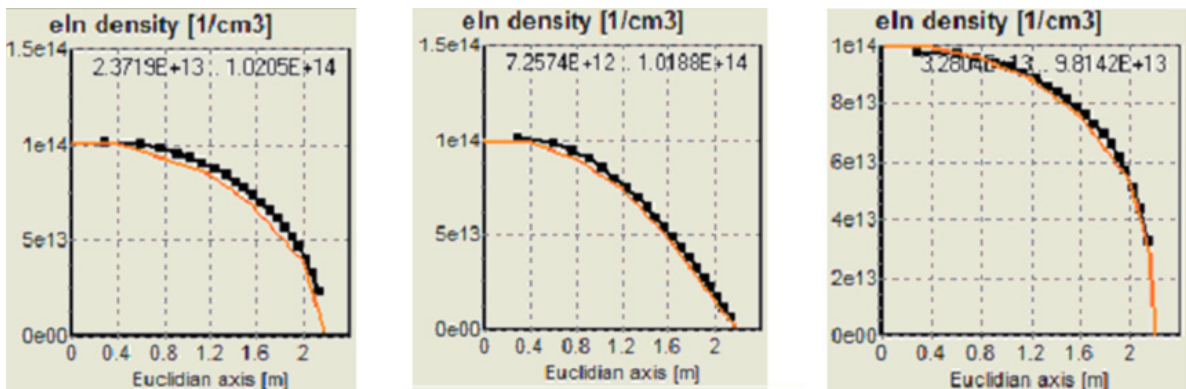
Fig. 12.4 Stationary density for classical, Bohm's and the 'artificial' diffusion coefficients

Finally, these TOKES calculations were compared with that of MHD transport code ASTRA for the same plasma configuration and diffusion coefficients Ref.[13]. The corresponding plasma density profiles calculated by ASTRA are shown on Fig.5. The agreement between TOKES and ASTRA calculations seems good.
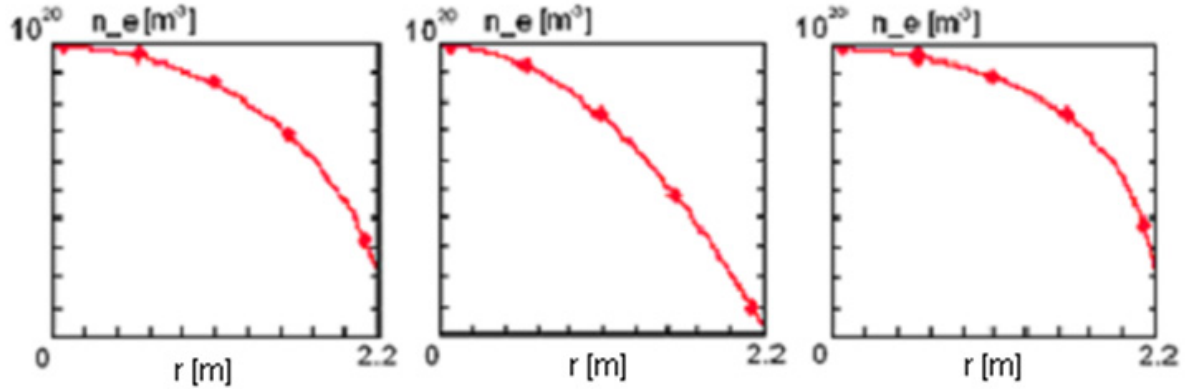
Fig. 12.5 Stationary profiles of density n produced by ASTRA for the classical, Bohm's and artificial diffusivities

Additionally, the geometrical factors G_n Λ_n, H, L, and safety factor q given by Eq.(5.1), Eq.(5.8) and Eq.(5.9) which are produced by TOKES were compared with their values analytically obtained for the configuration Fig.3. The toroidal magnetic flux W depends on a as $W = B_\zeta \pi a^2$. The analytical dependence of poloidal magnetic flux w is $w \approx w_2 r^2$, with $w_2 = \pi r_0 J_\zeta /c$ for the current density $J_\zeta = I/(\pi a^2)$. The poloidal magnetic field $B_y = -(1/r_0)dw/dr$ increases linearly with r inside the plasma and decreases as $1/r$ outside, being continuous at $r = a$. The safety factor q is constant:

$$|q| = \frac{cB_\zeta}{2I} \frac{a^2}{r_0}$$

(12.2)

(In TOKES algorithms, $q < 0$ is defined.) For $B_\zeta = 5.3$ T, $I = 15$ MA, $r_0 = 1$ km and $a = 2.2$ m it follows $|q| = 0.85 \times 10^{-2}$. (At $r_0 = 6.2$ m, as it is assumed for ITER, it would be $|q| \approx 1.4$.)

The poloidal magnetic flux step Δw that provides a number X of magnetic layers inside the plasma follows as

$$\Delta w = \frac{I}{c} \frac{r_0}{X} \qquad \Rightarrow \qquad r = a\sqrt{\frac{x}{X}}$$

(12.3)

The layer index $x = 0..X-1$. For $I = 15$ MA, $r_0 = 1$ km and $X = 20$ it follows $\Delta w = 75$ Weber. The corresponding TOKES calculation with $\Delta w = 75$ Weber resulted in 20 layers occupied with plasma, which fits exactly to the theory.

The m-volume G_m and the m-elongation Λ_m inside a plasma layer x follow as

$$G_m = r_0^{m-2} \pi \frac{a^2}{X}, \qquad \Lambda_m = 4\pi x r_0^{m-2} \qquad (12.4)$$

In particular, all plasma layers have the same volumes and the same poloidal areas, Λ_m are proportional to r^2. For instance, at $a = 2.2$ m and $X = 20$ it follows from Eq.(4) at $x = X$ that $G_2 \approx 0.76$ m^2 and $\Lambda_2 \approx 251$.

Eq.(4) provides the lowest approximation on the small parameter a/r_0, which is not sufficient for calculation of the coefficient H. Therefore an analytical expansion on $a/r_0 \ll 1$ was done and finally $H \approx 2a^2 x/X$ obtained. At $a/r_0 \ll 1$ the factor L acquired the form:

$$L = 4\left(2q^2 - 1\right)\frac{r_0^2}{a^2} xX \qquad (12.5)$$

Thus L is negative at small q and positive at $|q| > 1/\sqrt{2}$. At the plasma boundary $x = X$ we get
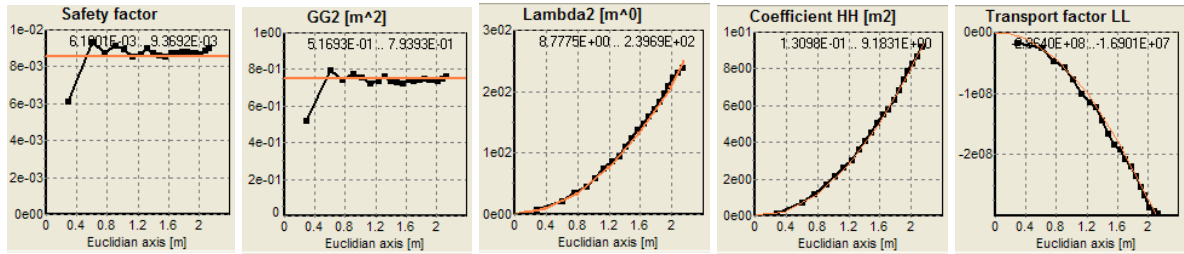
Fig. 12.6 TOKES tests: Theory fits well the calculated geometric factors (shown with squares).
$L \approx -3.3 \times 10^8$ at $r_0 = 1$ km, $a = 2.2$ m and $X = 20$. Fig.6 demonstrates the comparisons of analytically obtained parameters with those produced with TOKES.

13. Modelling of convection equation on the graph

One-dimensional convective processes are described with the 1st order hyperbolic equation using the splitting method. The splitting method for the plasma transport equations is mentioned before Eq.(11.1). Initially we demonstrate the solving of the convection equation for one region of increasing magnetic flux w in a simplified form omitting the sinks and sources and assuming the 'volume' G constant in time:

$$G\frac{\partial S}{\partial t} + \frac{\partial}{\partial x}(vS) = 0 \qquad (13.1)$$

Eq.(1) describes a process determined by the positive functions $S(t,x)$ (the 'density') and $G(x)$. The 'velocity' $v(t,x)$ can get positive or negative depending on t and x. We suggested (see Ref.[14]) and use in TOKES a special numerical technique, in particular for Eq.(1). The advantage of this approach is formally arbitrary time step τ (however, too large τ can result in

either immediate stationary state or rather unphysical behaviour of the numerical values S_k which remain always positive).

Usual approaches (see e.g. Ref.[15]) limit the numerical time step as $\tau < G\Delta/|v|$ (the Courant's stability criterion), so that stable solutions do not permit large values of velocity v. We comment that at too large velocity the flux $F = vS$ flowing into a cell $(x, x+\Delta)$ overloads or empties it of the substance of density S. However, in reality the substance flows farther, into or from the next cells, which we take into consideration aiming at improving numerical stability. Below we assume x the index coordinate (thus $\Delta = 1$). The values of G and v are available at the beginning of the sub-step, but we omit the up-script '^' for them. We employ the implicit scheme that formally does not limit the time step at arbitrary positive velocity:

$$G(x)\frac{S(x)-\hat{S}(x)}{\tau} + \frac{S(x)v(x+1/2)-S(x-1)v(x-1/2)}{\Delta} = 0 \qquad (13.2)$$

The positive influx $F(0) = v(0)S(-1)$ should be known. The solution is obtained by iterations:

$$S(x) = \frac{\hat{S}(x)+S(x-1)\dfrac{v(x-1/2)}{G(x)}\dfrac{\tau}{\Delta}}{1+\dfrac{v(x+1/2)}{G(x)}\dfrac{\tau}{\Delta}} \qquad (13.3)$$

As we see, at integer $x \geq 0$ the positive solution $S(x)$ follows with arbitrary time step $\tau > 0$.

If v depends on x with changing the sign of v, there are several regions margined by zero velocity. Let's consider a cell x from both sides of which the substance flows out (the 'donor' cell, see Fig.1): $v(x-1/2) < 0$ and $v(x+1/2) > 0$. The scheme for this cell reads:

$$G(x)\frac{S(x)-\hat{S}(x)}{\tau} + \frac{S(x)v(x+1/2)-S(x)v(x-1/2)}{\Delta} = 0 \qquad (13.4)$$

Thus we do not need substance densities from the neighbour cells and immediately obtain:

$$S(x) = \frac{\hat{S}(x)}{1+\dfrac{v(x+1/2)-v(x-1/2)}{G(x)}\dfrac{\tau}{\Delta}} \qquad (13.5)$$

The influxes into both neighbour cells follow as

$$F(x-1/2) = S(x)v(x-1/2), \qquad F(x+1/2) = S(x)v(x+1/2) \qquad (13.6)$$
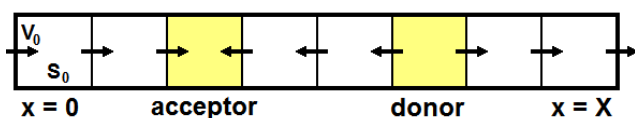
Fig. 13.1 The scheme of plasma flows through the numerical mesh showing the 'donor' and the 'acceptor' cells.

Those donor cells allow employment of the iterations Eq.(3) in both directions, over the regions of constant sign of velocity. Completing

these procedures we get the fluxes at the boundaries of the cells-'acceptors' (see Fig.1) of the substance (inflow from both cell's sides). For an acceptor cell x we have:

$$S(x) = \hat{S}(x) - \frac{\tau}{G(x)\Delta} \left(S(x+1)\upsilon(x+1/2) - S(x-1)\upsilon(x-1/2) \right) \qquad (13.7)$$

(The neighbour substance densities are already known.) As to the boundaries of the whole domain (at $x = -1/2$ and $x = X+1/2$) only the influxes must be given, and outfluxes follow from the described calculation.

In the graph hierarchy of magnetic layers the numerical solution to Eq.(1) is described as follows. Let's start from the origin layer and come throughout the chain of sons (that can be empty) to either the childless layer (which reduces the problem to the considered above one) or to a multiple-son layer. The sons of that layer can all be acceptors, which would also solve the problem, because in this case the information from the sons is not necessary. If some of the sons are not acceptors, the same procedure as for the origin layer is repeated for each such sun in recursive way (i.e. before we process further) and thus in particular the influxes from them become available, which finally solves the whole problem. Furthermore, in the particular algorithm it is not necessary to distinguish the childless, one-son and multiple-son layers. Below they are incorporated in the calculations in a common way therefore the previous simplified algorithm that works with the linear sequence of fluid cells is not needed.

The following hyperbolic equation that generalizes Eq.(1) is solved with TOKES for the graph structure of magnetic layers:

$$\frac{\partial}{\partial t}(GS) + \frac{\partial}{\partial x}(\upsilon S) = q - pS \qquad (13.8)$$

Now we assume the 'volume' $G > 0$ as a function of t and x, $q \geq 0$ is the 'source' and $p \geq 0$ the 'sink frequency'. In the graph, G, q, p and S are attributed to the layers. The velocity υ is implied at the layer-layer interfaces. The finite-difference equation for a layer that has arbitrary number of sons (and one dad) is given by

$$gS - \hat{g}\hat{S} + \upsilon_d^+ S + \upsilon_d^- S_d - \sum_s \left(\upsilon_s^+ S_s + \upsilon_s^- S \right) = q - pS \qquad (13.9)$$

Here $g = G/\tau$. The function υ with '+' is υ itself only if $\upsilon > 0$ (otherwise it equals zero). Similarly, υ with '−' is υ itself only if $\upsilon < 0$. Thus in the corresponding pairs of Eq.(9) one term of the pair is equal to zero.

To solve the system Eq.(9), the code starts from the origin layer. Its dad absents, so that we have $\upsilon_d^+ = \upsilon_d^- = 0$ and $S_d = 0$. Then the code checks for the interfaces with the sons that have positive velocities. If some of sons have $\upsilon_s > 0$ (so that the substance flows from the

son to the dad), the corresponding values of S_s are not yet known. However, the code will get S_s in the recursive way (see below) and substitute them into the formula following Eq.(9):

$$S = \frac{\widehat{g}\widehat{S} + q + \left|v_d^-\right|S_d + \sum_s v_s^+ S_s}{g + p + v_d^+ + \sum_s \left|v_s^-\right|}$$

(13.10)

In fact, the sum on s in the numerator includes only positive velocity interfaces with the sons. The sum in the denominator includes negative velocity interfaces. Then the calculation is similarly repeated for the sons of $v_s \le 0$, however without the recursive processes.

To obtain S_s in the case $v_s > 0$ the code has in advance to solve the equations Eq.(9) for the corresponding son-layers, which is performed as a recursive process just before substituting S_s into Eq.(10). In this process the code does not need to know S, because those sons are the donors of their dad. Therefore, solving Eq.(9) for those sons (if the son would be the origin layer) the code assumes that the numerator term with S_d does not contribute.

The corresponding Delphi algorithm for Eq.(9) is the function SSofDonor:

```
function TLayer.SSofDonor(SSdVd: Real): Real;
  var
    I: Integer;
    W, WS: Real;
begin
  W := G + P;
  WS := G0 * SS0 + QQ;
  with Dad.Core do
  if V > 0 then
    W := W + V
  else
    WS := WS – SSdVd;
  for I := 0 to High(Son) do
  with Son[I].Core do
  if V > 0 then
    WS := WS + V * Son[I].Associate.SSofDonor(0)
  else
    W := W – V;
  SS := WS / W;
  Result := SS;
  for I := 0 to High(Son) do
  if Son[I].Core.V <= 0 then
    Son[I].Associate.SSofDonor(SS * Son[I].Core.V);
end;
```

This function is called from the origin layer as the sentence:

```
OriginLayer.SSofDonor(0); // (the result of this call is not used)
```

Before calling, the values of G0 (i.e. $\hat{g}$), G (g), P (p), SS0 ($\hat{S}$), QQ (q) and V (v) have to be assigned in the layers and the layer interface structures. The results are SS (S). In the algorithm the fluxes at the graph ends are equal to zero, as it was described in Sec.11.

This algorithm was tested with the graph Fig.12.1 comparing the result of the function SSofDonor with a standard solver for the corresponding linear system of equations. The values of v are given as follows, according to the corresponding core indices:

$$v_0 = 1,\ v_1 = 2,\ v_2 = 3,\ v_3 = -2,\ v_4 = -1,\ v_5 = 0,\ v_6 = 1,\ v_7 = -2,\ v_8 = 1,\ v_9 = 0$$

The values of G0 and G are given in terms of the layer index l as G0 = G = l + 1. The values of SS0 are given as SS0 = $10 - l$. The sources are given as $q = l^2$ and the frequencies as $p = (l - 5)^2$. According to Eq.(9), the Gaussian system of equations acquires the form:

$$\left(g_l + p_l + v_d^+ + \sum_s \left| v_s^- \right| \right) S_l - \left| v_d^- \right| S_d - \sum_s v_s^+ S_s = \hat{g}_l \hat{S}_l + q_l \tag{13.11}$$

The test on comparison of the Delphi algorithm with the solution by the Gauss' method of the same problem resulted in completely equal values of SS, for instance SS[0] = 0.37037037037 and SS[9] = 3.6617715618.

Part III   Impurities, fuelling and heating

14. Numerical schemes for thermal exchange among species

For two plasma species, for instance ion species i and j (but one can also be electrons) in the splitting approach explained in Sec.11, the heat exchange sub-step acquires the form of two equations that should be solved independently in each plasma layer:

$$\frac{3}{2} n_i \frac{\partial T_i}{\partial t} = 3 \frac{q_{ij}}{m_i + m_j}\left(T_j - T_i\right), \qquad \frac{3}{2} n_j \frac{\partial T_j}{\partial t} = 3 \frac{q_{ji}}{m_i + m_j}\left(T_i - T_j\right) \qquad (14.1)$$

In this sub-step the ion densities n_i and n_j are fixed only the temperatures T_i and T_j are assumed depend on time. Summing these equations gives their integral (thermal energy conservation):

$$n_i T_i + n_j T_j = \text{const} \qquad (14.2)$$

The equation for the temperature difference follows as

$$\frac{\partial}{\partial t}\left(T_i - T_j\right) = -2 \frac{q_{ij}}{m_i + m_j}\left(\frac{1}{n_i} + \frac{1}{n_j}\right)\left(T_i - T_j\right) \qquad (14.3)$$

Its solution after a time step τ is given by

$$T_i - T_j = \left(T_{i0} - T_{j0}\right)x, \quad x = \exp\left(-\nu_{ij}\tau\right) \quad \nu_{ij} = \frac{2q_{ij}}{m_i + m_j}\left(\frac{1}{n_i} + \frac{1}{n_j}\right) \qquad (14.4)$$

The temperatures with the index 0 correspond to the beginning of the time step. The final temperatures are

$$T_i = T_m + n_j \frac{T_{i0} - T_{j0}}{n_i + n_j}x, \quad T_j = T_m + n_i \frac{T_{j0} - T_{i0}}{n_i + n_j}x, \quad T_m = \frac{n_i T_{i0} + n_j T_{j0}}{n_i + n_j} \qquad (14.5)$$

These formulas give positive temperatures. At infinite time step, i.e. $x = 0$, we get $T_i = T_j = T_m$.

For energy exchange among several different species we have the system of equations:

$$\frac{3}{2} n_i \frac{\partial T_i}{\partial t} = 3 \sum_{j \ll i} \frac{q_{ij}}{m_i + m_j}\left(T_j - T_i\right) \qquad (14.6)$$

Summation of the equations over i results in mutual cancellations of the right hand sides and thus in the thermal energy conservation equation:

$$\sum_i n_i T_i = \text{const} \tag{14.7}$$

At infinite time step all temperatures would acquire common mean value T_m given by

$$T_i(t \to \infty) = T_m = \frac{\sum_i n_i T_i}{\sum_i n_i} \tag{14.8}$$

As T_m does not depend on time, it is a convenient reference point for the temperatures. As it is usual for linear systems with constant coefficients, Eq.(6) is solved seeking the solution as expansion on a number of exponential terms: $T_i \sim \exp(-\nu t)$. Eq.(6) acquires the form:

$$\sum_{j \diamond i} a_{ij} T_j = 0, \quad a_{ij} = \nu_{ij} + \left(\nu - \sum_{j \diamond i} \nu_{ij}\right) \qquad \nu_{ij} = \frac{2}{n_i} \frac{q_{ij}}{m_i + m_j} \tag{14.9}$$

The dispersion equation for ν is $\det|a_{ij}| = 0$. However, it seems too tedious to continue in such way. Therefore currently in TOKES the two-species processes are implemented, and the thermal energy exchange is split into the corresponding number of pair processes: $N(N-1)/2$ sub-steps, where N is the number of different plasma species.

15. Solving of two ion species mix equations

In the ion density evolution equations Eq.(5.6) there are the terms that describe mutual mixing of different ion components as some composition of diffusion and convection processes. The corresponding sub-step deals with two equations for some different ion species (we designate them below with $i = 0$ and $j = 1$). Solving those pairs of sub-step equations for one arbitrary time step τ we assume that x is the index coordinate (i.e. the spatial step $\Delta = 1$), the magnetic configuration fixed in time (i.e. the layer volume G_3 does not depend on t), and ion temperatures T_0 and T_1 are also fixed. In TOKES only the terms with the large parameter $a_{ij}/a_e \gg 1$ are accounted for in the fluxes Π_i Eq.(5.7) (see in Ref.[16]). The split-off pair of equations reads:

$$G_3 \frac{\partial n_0}{\partial t} = \frac{\partial}{\partial x}(A\Pi_0), \qquad G_3 \frac{\partial n_1}{\partial t} = \frac{\partial}{\partial x}(A\Pi_1) \tag{15.1}$$

$$A\Pi_0 z_0 = -A\Pi_1 z_1 = c\left(\frac{n_1}{z_0}\frac{\partial p_0}{\partial x} - \frac{n_0}{z_1}\frac{\partial p_1}{\partial x}\right), \qquad c = AC\frac{a_{01}}{a_e} \qquad (15.2)$$

Due to the anti-symmetry of Eq.(1) on indices permutation, one motion integral is available:

$$N(x) = z_0 n_0 + z_1 n_1 \qquad (15.3)$$

The sum $N(x)$ does not depend on time.

Then we split Eq.(1) into two additional sub-steps, differently selecting the terms in $A\Pi_i$ but keeping the anti-symmetry. First sub-step equations read:

$$z_0\frac{G_3}{T_0}\frac{\partial p_0}{\partial t} = \frac{\partial}{\partial x}\left(\frac{c}{T_1}\frac{p_1}{z_0}\frac{\partial p_0}{\partial x}\right), \qquad z_1\frac{G_3}{T_1}\frac{\partial p_1}{\partial t} = -\frac{\partial}{\partial x}\left(\frac{c}{T_1}\frac{p_1}{z_0}\frac{\partial p_0}{\partial x}\right) \qquad (15.4)$$

The second sub-step is identical but the indices 0 and 1 are permuted. For the analytical form Eq.(4) the motion integral Eq.(3) remains valid. Eq.(4)$_1$ is the diffusion type equation (in respect to p_0) and Eq.(4)$_2$ the 1st order hyperbolic equation (in respect to p_1). In Sec.11 and Sec.13 the stable and conservative solvers for these equations were described. The solvers guarantee positive numerical solution $p_i > 0$ and keeping the sum $\sum_x n_i(x+\frac{1}{2})G(x+\frac{1}{2})$ constant after arbitrary time step.

However, in addition we impose the conservation of $N(x)$ in the numerical solving, which makes calculations more bulky. Eq.(4)$_1$ is rewritten as the diffusion equation:

$$G_0\frac{\partial p_0}{\partial t} = \frac{\partial}{\partial x}\left(D\frac{\partial p_0}{\partial x}\right), \qquad D = \frac{c}{z_0 T_1}p_1, \quad G_0 = z_0\frac{G_3}{T_0} \qquad (15.5)$$

Eq.(4)$_2$ is rewritten as the convection equation with the coefficient D as a flowing substance:

$$G\frac{\partial D}{\partial t} + \frac{\partial}{\partial x}(\upsilon D) = 0, \qquad \upsilon = \frac{\partial p_0}{\partial x}, \qquad G = z_0 z_1\frac{G_3}{c} \qquad (15.6)$$

The values of G_3, c and T_i are assumed given at the cells' centres.

The calculations for the equations Eq.(5) and Eq.(6) are performed in iterative way. Initially Eq.(6) is solved substituting p_0 available at the beginning of the time step. The obtained values of D are then substituted into Eq.(5) and then Eq.(5) solved. The obtained p_0 is used again in Eq.(6), and so forth until the function $N(x)$ obtained after each iteration converges with relative accuracy of 10^{-6} to its initial values. To provide the anti-symmetry, the appropriate values of $D(x)$ are used. According to the rule that provides stability of Eq.(6), if we have last available $p_0(x-\frac{1}{2}) < p_0(x+\frac{1}{2})$ then $D(x-\frac{1}{2})$ otherwise $D(x+\frac{1}{2})$ is substituted instead $D(x)$. Fig. 1 demonstrates the test results for $n_i(x)$ obtained for an impurity of $z_1 = 6$ in the main species of $z_0 = 1$. In this calculation linear dimensionless functions for the

parameters are chosen: $c(x) = T_0(x) = 0.5+1.5x$, $G_3(x) = T_1(x) = 2-1.5x$, and the functions $n_0(x) = \exp(\sin(\pi(x-0.5)))$, $n_1(x) = 0.1 \times \exp(\sin(\pi(0.5-x)))$ as initial densities.
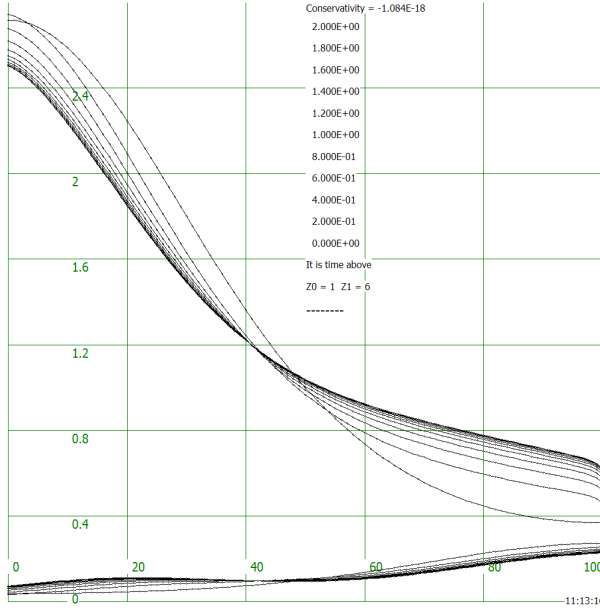
Fig. 15.1. Test calculation for ion-ion mutual mixing with 100 cells ($\Delta x = 10^{-2}$, $\tau = 10^{-2}$).

If the averaging described by Eq.(5.13) was performed (the averaged charge approximation), Eq.(2)$_1$ remains valid, with the meaning that the indices 0 and 1 describe the atomic kinds and the charge states are the averaged charge states, thus z_0 and z_1 are some functions of t and x. From this follows that after the averaging the motion integral $N(x)$ defined by Eq.(3) is not longer valid, because it was obtained multiplying the equations Eq.(1) by constant charge states and then summing them. For numerical solving of Eq.(1) with non-constant charge states we apply the splitting method again, but with some modifications (if not say simplifications). We extract the temperatures T_k from p_k and thus the diffusion sub-step equations take the form:

$$G_3 \frac{\partial n_k}{\partial t} = \frac{\partial}{\partial x}\left(D_k \frac{\partial n_k}{\partial x}\right), \qquad D_k = c\frac{n_{k'}T_k}{z_k^2} \tag{15.7}$$

(Here $k = 0$ or 1 and $k' = 1-k$). The convection sub-step equations take the form:

$$G_3 \frac{\partial n_k}{\partial t} = \frac{\partial}{\partial x}(G_3 \upsilon_k n_k), \qquad \upsilon_k = \frac{c}{G_3 z_k}\left(\frac{n_{k'}}{z_k}\frac{\partial T_k}{\partial x} - \frac{1}{z_{k'}}\frac{\partial p_{k'}}{\partial x}\right) \tag{15.8}$$

Again, to provide the mentioned earlier anti-symmetry, if $\upsilon_k(x) > 0$ was obtained then $D_k(x-\frac{1}{2})$ is used, otherwise $D_k(x+\frac{1}{2})$.

However, it seems that the motion integral $N(x)$ is very important from the viewpoint of separating the slow plasma diffusion itself and the ion-ion transport. The plasma diffusion can be adequately described in the averaged charge approximation. But adequate ion-ion mixing needs more details. Therefore the following compromise way is chosen that provides keeping the motion integral. In the ion-ion transport calculations, for each atomic kind some definite charge states are chosen that represent the ions in the whole vessel. The more precise calculations should be performed the more representative charge states should be chosen. Maximally all ion charge states can be taken: $z = 1..Z_k$, with Z_k the chemical number of the atomic kind k. In a rough ion-ion mixing calculation the representative charge states can be

55

chosen starting from $z = 1$ and then, for example, as it is chosen in the code TOKES, which demonstrates Table 1:

Table 15.1: An example for the representative charge states

Atomic kind	Representative charge states
H (any isotope)	1
He	1, 2
Li	1, 2, 3
Be	1, 2, 3, 4
B	1, 2, 3, 4, 5
C	1, 2, 3, 4, 6
W	1, 2, 3, 4, 6, 9, 13, 18, 28, 38, 46, 56, 64, 74

In TOKES, the charge states $z = 1, 2, 3$ and Z_k are chosen anyway. For light elements the next representative charge state is chosen approximately multiplying the previous one by a factor of 1.5. For heavy elements such as tungsten, at large z those ones are chosen as the representative states that occupy maximum intervals on the logarithmic scale of electron temperature in the Saha ion populations. The populations of other charge states are moved to nearby representative charge states (according to the differences of charge states).

It is to note that for the modelling of multi-fluid plasma with accounting for radiation transport the average charge approximation and the representative charge approximation are too rough. The radiation transport model of TOKES is described in Sec.18.

16. Neutral beams modelling
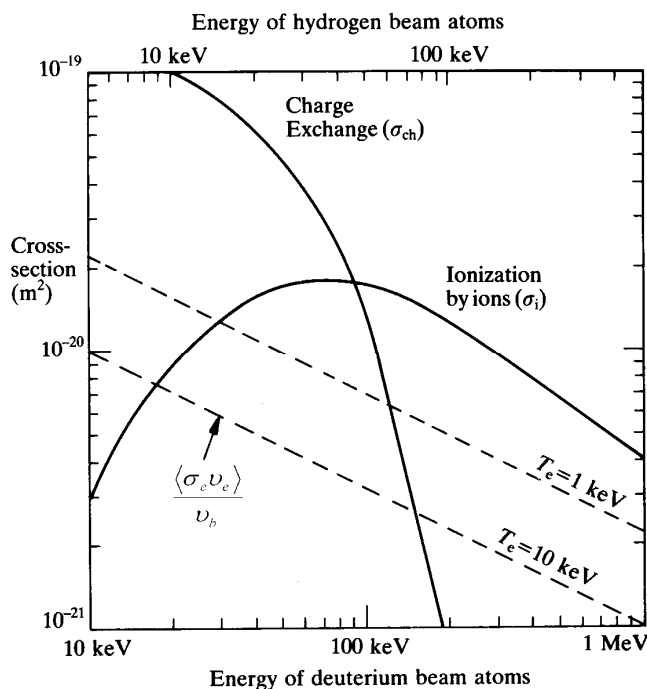
Fig. 16.1. Cross-sections of ionization and CX

Neutral beam (NB) is an important auxiliary heating system of modern tokamak reactors. NB supplies also the D- and T-atoms into the confined plasma. However, in future reactors penetration of single atoms will be not sufficient. Therefore in addition to NB, for achieving deep fuelling the pellet injection and radio-frequency electromagnetic (RF) heating for deep plasma bulk are necessary. In TOKES the pellet injection is so far replaced by spreading DT atoms in the plasma

volume, which provides the fuelling. The RF-heating is not implemented. The implementation of NB and atoms emitted from the wall or gas puffing atoms, as well as other kinds of neutrals (fusion reaction neutrons and plasma emitted photons) is done with the same algorithm described in this section. The NB stopping model follows Ref.[8].

The neutrals travel in straight lines being unaffected by the magnetic field. The atoms become either charge exchanged (CX) with plasma ions or ionized through collisions with the plasma particles, or they strike the wall. The resulting ions of the charge state $z = 1$ are held by the magnetic field and later are further ionized (if the chemical number $Z_m > 1$). The fast DT-ions originated from the neutral beam are slowed down and finally relax to the thermal equilibrium in vicinity of original magnetic surface. The secondary atoms after CX are so slow in comparison with original atoms that are assumed be motionless until the ionization, so that in fact CX is equivalent to the ionization.

The intensity of the beam $I_b = n_b v_b$ where n_b and v_b are the density and the velocity of beam atoms, respectively, decays in plasma obeying the Buger's law:

$$\frac{1}{I_b}\frac{dI_b}{dl} = -\frac{1}{l_b} = -n_e \frac{\langle \sigma_{eb} v_e \rangle}{v_b} - \sum_i n_i \left(\sigma_{ib\mathrm{ch}} + \sigma_{ib} \right)$$

(16.1)

Here l is the length along beam trajectory, l_b the decay length, $\langle \sigma_{eb} v_e \rangle$ the electron ionization rate coefficient, $\sigma_{ib\mathrm{ch}}$ the CX cross-section for inelastic collisions with the ion species i, and σ_{ib} the ionization cross-section. The electron thermal velocity v_{Te} is assumed larger than v_b. Fig. 1 demonstrates the cross-sections. One can see the ionization due to electrons is always negligibly low, CX is most effective when the beam atom energy E_b is below 100 keV and the ionization due to ions at $E_b > 100$ keV. For typical density of 10^{20} m^{-3} and $E_b = 100$ keV the decay length $l_b \approx 0.3$ m follows from Eq.(1). The NB atoms are optimally injected in poloidal plane perpendicularly to the z-axis and with a fixed coordinate $z = z_b$, however for instance with $z_b > z_0$ (z_0 is the magnetic axis elevation) in

Fig. 16.2 Poloidal projections of neutral ray trajectories as they are simulated with TOKES

order to avoid overheating of plasma centre.

The implementation of neutrals propagation through the tokamak vessel is done assuming the toroidal symmetry, which allows the reduction of calculations to one starting toroidal angle ζ. Simulation for one straight trajectory that starts at $\zeta = 0$ and stretches into the vessel (representative ray) describes the whole symmetric set of the trajectories parameterized by ζ. A real NB injected through a localized window in the surface, TOKES simulates also as if the beam would be symmetrically spread over ζ. For the plasma absorption this assumption is adequate, because due to the high thermal velocity of plasma particles the real beam produces negligible non-homogeneity of plasma along each magnetic surface, thus interacting with the plasma like the spread beam (the typical electron temperature non-homogeneity can be estimated as $\Delta T_e/T_e \sim 10^{-9}$). However, the damage the real beam may cause to the opposite wall is also localized on the toroidal angle thus destroying the symmetry. However, in the applications of NB full absorption of the beam in the plasma should be achieved therefore this issue seems not substantial.

Fig.2 demonstrates the poloidal plane projections of the trajectories of neutral rays freely propagating in ITER vessel. The straight rays are seen as the solid curves which are approximated with the chains of lines across the cells of triangle cross-section.

For the wall emitted atoms the Monte-Carlo method is applied. The rays are spread at the wall surface as random beams localized in 2π steradians of solid angle (half-isotropic).

17. Heating by alpha particles

An alpha particle (or simply "alpha") is the nucleus $_2\text{He}^4$ produced in the deuterium-tritium fusion reaction $_1\text{H}^2 + _1\text{H}^3 \rightarrow _2\text{He}^4 + _0\text{n}^1$, with the alpha (of the energy $E_\alpha = 3.5$ MeV) confined and the neutron $_0\text{n}^1$ (14.1 MeV) immediately lost from the hot plasma Ref.[8]. Given equal temperatures T of deuterium and tritium ion species, the reaction rate in the temperature range of interest (about 3 to 30 keV) is well approximated analytically by

$$\langle \sigma v \rangle \left[\text{cm}^3/\text{s} \right] \approx \frac{5 \times 10^{-12}}{T_{\text{keV}}^{2/3}} \exp\left(-\frac{20}{T_{\text{keV}}^{1/3}} \right) \tag{17.1}$$

The alphas slowed down inside the hot plasma remain in the confinement region, which congregates deleterious "ash" (helium ions).

In TOKES we assume that the stopping is due to electrons only and during it the alpha remains at the same magnetic surface. Therefore in each plasma layer the fusion heating is

independent. The calculation of it is some sub-step in which the fusion term is split from the term Q_e of the electron thermal energy transport equation Eq.(5.15):

$$Q_e^{(\alpha)} = E_\alpha n_{H2} n_{H3} \langle \sigma \upsilon \rangle \qquad (17.2)$$

In various cases of plasma dynamics the fusion energy source Eq.(2) can destabilize the confinement by causing uncontrolled rise of plasma temperature. During the DT burning process at the plasma temperature T significantly smaller than that of maximum of the cross-section Eq.(1), e.g. at $T = 15$ keV, the fusion source term can get nevertheless dominating in Eq.(5.15), which would result in a fast and undesirable increase of T up to $20 - 30$ keV.

To control the fusion reaction power the following two procedures are used in TOKES: 1) Automatic variation of deuterium neutral beam power W_b, which can stabilize the fusion reaction at some $W_b = W_{bm}$ below maximum beam power W_{bmax}. The variation of W_b is implemented with fixed atom energy, varying only beam's deuterium inflow. The total deuterium inflow remains constant, being dynamically redistributed between the beam and deuterium pellets.

If the reaction breaks this feedback control, as a consequence W_b soon drops down below some fixed small value W_{b1} which turns on an additional control procedure of the code: 2) Switching off the tritium source: the tritium pellets are replaced by deuterium pellets keeping atom inflow constant. Due to diffusive transport of tritium from the confined region the rise of fusion power gradually ceases and then it decreases.

Meanwhile W_b reached some minimum value W_{b0} (e.g. $W_{b0} = 0$). After the reaction power got low, consequently W_b begins to increase and 1st procedure tries recovering the control. However, without the tritium source the fusion power cannot be controlled. Therefore after W_b exceeded some value W_{b2} (e.g. $W_{b2} = W_{b1}$) tritium source switches on again which finally recovers the feedback control.

To indicate the state of the controlled reaction after each time step τ the feedback control procedure calculates specially averaged temperature:

$$T_a = \eta \frac{1}{N_e} \int_V n_e T_e dV + (1-\eta) \left(\begin{array}{c} \int_0^t T_{max}(t') \exp\left(\dfrac{t'-t}{\Delta t}\right) dt' \\ +T_{max}(0) \exp\left(-\dfrac{t}{\Delta t}\right) \end{array} \right) \qquad (17.3)$$

Here the factor η ($\eta = 2/3$ so far) determines the fractions of 1) the averaging of electron pressure $n_e T_e$ normalized by total number of electrons N_e over the plasma volume V and 2) exponentially weighted time averaging of plasma maximum temperature T_{max} with some

effective period Δt (e.g. $\Delta t = 1$ s). If for example T_a exceeds a fixed value T_m, at the next time step W_b decreases compared to $W_{b\text{max}}$ as describes the formula

$$W_b\left(t + \Delta t\right) = \max\left[W_{b0}, \min\left(W_{b\max}, \left(2 - \frac{T_a(t)}{T_m}\right)W_{b\max}\right)\right]$$

(17.4)

Thus, if e.g. in a stable regime we have $T_a = (3/2)T_m$, it gives $W_{bm} = W_{b\text{max}}/2$. It is worthwhile noting that TOKES easily achieves the exponentially weighted time averaging in Eq.(3): For any function of time $f(t)$ such averaged value $\bar{f}$ is calculated as

$$\bar{f}(t + \Delta t) = \left(1 - \frac{\Delta t}{\tau}\right)\bar{f}(t) + \frac{\Delta t}{\tau}f(t), \quad \bar{f}(0) = f(0)$$

(17.5)

Part IV   Radiation transport

18. Simulation of electron level populations and photons

Usually the calculations of radiation losses and charge states are performed using some tables for the opacities and z_m, for instance for carbon as in the predecessor of TOKES the code FOREV-2D Ref.[17]. However, in tokamak plasma using those tables is not generally justified, and for multi-fluid plasmas the opacity tables with various concentrations of several plasma species m are hardly possible. Therefore in TOKES the calculations of radiation transport and ionization dynamics which consistently influence each other are implemented (see Ref.[18]).

In high temperature plasmas the radiation source usually appears from the free electrons (the bremsstrahlung). However, heavy chemical elements such as tungsten can remain not fully stripped of bound electrons. In such cases the atomic processes that change the state of bound electrons can also contribute to the radiation power by the mechanisms of recombination radiation and line radiation Ref.[23]. At the edge of tokamak plasma contaminated by wall material impurities the contribution of bound electrons to radiation losses can be significant.

The species density n_m and the quasineutral electron density n_e are the sums on the densities n_{mz} of ions with the charge state z, see Eq.(3.1). In turn, n_{mz} is a sum of population densities n_{mzk} of bound electron energy states k:

$$n_m = \sum_{z=z1}^{z2} n_{mz} \ , \qquad n_e = \sum_m \sum_{z=1}^{Z_m} z n_{mz} \ , \qquad n_{mz} = \sum_{k=0}^{K_{mz}} n_{mzk} \qquad (18.1)$$

The minimum charge state z_1 and the maximum charge state z_2 range as $0 \le z_1 \le z_2 \le Z_m$, with Z_m the chemical number of species m. In TOKES, to decrease calculation time the values of z_1, z_2 and the maximum level index K_{mz} are reasonably varied by the code in the course of calculation, in each plasma layer separately.

The densities n_{mzk} are determined in each layer independently by the equations:

$$\frac{dn_{mzk}}{dt} = S_{mzk}^{ed} + S_{mzk}^{ir} \qquad (18.2)$$

The contributions to the time derivative of n_{mzk} are due to changes of energy states k inside the system of bound electrons (S^{ed}) and due to the processes of ionization and recombination (S^{ir}) which change the charge states z. In ionization process one of bound electrons releases and gets belonging to the population of the free electrons. Recombination is the reversed process, i.e. the capture of a free electron by an ion. In the excitation process an (mz)-ion makes a transition to a state with the same z but some larger value of the levels excitation energy, and at the deexcitation it does vice versa.

The changes of the bound electron states occur due to collisions of free electron with ions and due to spontaneous and induced photodeexcitation and photorecombination. Therefore the terms S^{ed} and S^{ir} are separated into two parts:

$$S^{ed} = E^{ed} + P^{ed} \qquad (18.3)$$

$$S^{ir} = E^{ir} + P^{ir} \qquad (18.4)$$

The Greek capital letters indicate the contributions of the electron-ion (E) and photon-ion (P) processes. Both spontaneous and induced photon processes are taken into account in P^{ed} and P^{ir}. The right hand sides of Eq.(3) and (4) can be further expanded in bulky sums of diverse terms, which is done in Sec.19.

The related radiation transport and population dynamics calculations constitute one sub-step of TOKES splitting approach referenced below as the radiation sub-step. All processes that involve the bound electrons are implemented as one algorithm for Eq.(2). The bremsstrahlung is implemented independently however in frame of the radiation sub-step. Numerical integration of Eq.(2) over discrete increasing values of time t_n ($n = 1, 2, \ldots$) is done using the implicit finite-difference scheme:

$$\frac{n_{mzk}\left(t_n\right) - n_{mzk}\left(t_{n-1}\right)}{t_n - t_{n-1}} = S\left(t_n\right) \qquad (18.5)$$

The initial values $n_{mzk}(t_0)$ are assumed given. The right hand side $S = S^{ed} + S^{ir}$ is sufficiently linear in respect to n_{mzk}. This allowed implementation of an algorithm for solving Eq.(5) that is stable for arbitrary time steps $\Delta t_n = t_n - t_{n-1}$.

Neither potential barriers nor magnetic confinement prevent leakage of the photons from plasma. Often plasmas are 'optically thin', what implies unimpeded loss of photons of energy ε emitted inside plasma in any direction $\mathbf{s}$ of photon propagation ($\mathbf{s}$ is unit vector). However, with increasing plasma size the reabsorption becomes more and more important. Plasma of a large size is 'optically thick' if main part of emitted photons undergo reabsorption. If imaginary homogeneous plasma of endless size keeps the thermodynamic

equilibrium with electron temperature T_e, the Planck's function for distribution of photon energy forms. In terms of the spectral intensity $I(\varepsilon,\mathbf{s})$, for any $\mathbf{s}$ the Planck's function reads

$$I^P(\varepsilon) = \frac{2}{c^2}\left(\frac{\varepsilon}{2\pi\hbar}\right)^3 \frac{1}{\exp(\varepsilon/T_e)-1} \qquad [\text{cm}^{-2}\text{s}^{-1}] \qquad (18.6)$$

A thin beam of photons of energy ε can decay due to photoionizations, photoexcitations and inversed bremsstrahlung collisions. Simultaneously the beam can acquire new photons with the same energy ε due to the inversed processes. The absorption and the emission are described with the opacities: absorption coefficient κ [cm^{-1}] (the fraction of beam photons absorbed per 1 cm of the beam's way) and the emission ability β' [cm^{-3}s^{-1}] (the radiation energy flux emitted per steradian of solid angles, erg of photon energies and one cubic cm) that includes the contributions of both spontaneous and induced radiation. The equation describing the photon beam intensity (the Buger's law) reads:

$$\frac{dI}{ds} = \beta' - \kappa I, \qquad I|_{s=0} = 0 \qquad (18.7)$$

The coordinate s determines the positions along the straightforward trajectory of the beam across the plasma volume. Initial value $s = 0$ can be chosen at the crossing point of the emerging beam with plasma boundary. Generally the problem of numerical integrating of Eq.(7) is rather bulky because of a plenty of beams trajectories: specification of one straightforward trajectory needs 5 independent parameters: three initial coordinates $\mathbf{r}|_{s=0}$ and two angles of $\mathbf{s}$.

The numerical integration of Eq.(7) is done splitting the equation into an emission sub-step and a propagation sub-step. The emission sub-step is in fact only storing of radiation produced in the plasma layers in some accumulating structures of the layers. The emitted radiation is given by $\Delta Q = 4\pi\beta(\varepsilon)V\Delta\varepsilon\Delta t$, with V the layer volume, $\Delta\varepsilon$ some range of photon energies specified below, and Δt the time step. On the propagation sub-step the trajectories of the accumulated photons as toroidally symmetric rays across the vessel are calculated. The photon rays are like the atomic rays mentioned in Sec.16, and they are emitted from homogeneously random positions of plasma layers in isotropically random directions $\mathbf{s}$ (the Monte-Carlo method). It is to note that radiation reabsorption option is implemented in TOKES, but the code was applied without it (it is switched off so far), i.e. optically thin plasma was assumed in the performed calculations. However, below we describe the photon reabsorption as well.

The photon ray of initial energy $Q|_{s=0}$ starts from the random point, which empties the corresponding accumulator (i.e. one ray per accumulator per time step is simulated). Eq.(7) of the photon propagation sub-step takes the numerical form:

$$\frac{Q(s_i) - Q(s_{i-1})}{\delta s_i} = -\kappa'_i Q(s_i), \qquad (i = 1, 2, \ldots) \qquad (18.8)$$

The coordinate s_i $(i > 0)$ designates crossing of the interfaces between the layers, $\delta s_i = s_i - s_{i-1} > 0$ are spatial step sizes. Eq.(8) is solved step by step on i:

$$Q(s_i) = \frac{Q(s_{i-1})}{1 + \kappa'_i \delta s_i} \qquad (i = 0, 1, 2, \ldots) \qquad (18.9)$$

As it follows from Eq.(9), at $\kappa' \geq 0$ the radiation Q remains non-negative for arbitrary δs_i. However, in some cases (with "inverted" level populations) κ' can get negative. In such cases Eq.(9) may produce physically wrong result at large δs_i (if the denominator gets negative). To remove this numerical effect, the numerical scheme is modified: if $\kappa'_i < 0$, instead of Eq.(9) the following equation is solved:

$$\frac{Q(s_i) - Q(s_{i-1})}{\delta s_i} = |\kappa'_i| Q(s_{i-1}) \qquad (18.10)$$

The solution for the spatial step with $\kappa'_i < 0$ is given by

$$Q(s_i) = \left(1 + |\kappa'_i| \delta s_i\right) Q(s_{i-1}) \qquad (\kappa'_i < 0) \qquad (18.11)$$

Thus $Q(s_i)$ remains positive at arbitrary δs_i.

In each plasma layer there are many different accumulators of radiation: for the line radiation each line (*mzl*) has one own accumulator, for the recombination radiation each level (*mzk*) has one own accumulator, and for the bremsstrahlung an array of accumulators is available in the layer. That array of a length J (e.g. $J = 16$) accumulates the bremsstrahlung depending on photon energies in some wide range $(\varepsilon_{min}, \varepsilon_{max})$, for instance, $\varepsilon_{min} = 0.1 \times T_{min}$ and $\varepsilon_{max} = 10^2 T_{max}$, with T_{min} and T_{max} the extremes of T_e over the confined plasma. Exponentially rising values of boundary energies ε_j $(j = 0..J)$ of bremsstrahlung accumulators are chosen:

$$\varepsilon_j = \exp\left(\ln \varepsilon_{min} + \frac{j}{J} \ln \frac{\varepsilon_{max}}{\varepsilon_{min}} \right) \qquad (18.12)$$

The recombination radiation Q_k (the leading indices m and z are omitted) is stored assuming one $\varepsilon = \varepsilon_k$ and some $\Delta\varepsilon = \Delta\varepsilon_k$ that are the result of averaging over photorecombination cross-section dependence on ε (as it is explained below). The line radiation Q_l is stored assuming the resonance photon energy: $\varepsilon = E_l$, and $\Delta\varepsilon = \Delta\varepsilon_l$ some

effective line width (as it is also explained below). The bremsstrahlung Q_j ($j = 0..J{-}1$) is stored with the photon energy $\varepsilon_j = \frac{1}{2}\left(\varepsilon_j + \varepsilon_{j+1}\right)$ and the photon energy intervals $\Delta\varepsilon = \varepsilon_{j+1}{-}\varepsilon_j$.

The emitted photons of particular accumulator have some single however random energy value ε_r which is different from the value of ε assumed at the accumulation, but averaged ε_r equals ε. At first the recombination and line photons are emitted and at the second the bremsstrahlung ones. After obtaining the amount of emitted photons $n_{ph} = Q/\varepsilon_r$ of line- and recombination accumulators the frequencies of the transitions, of photodeexcitation and photorecombination respectively, are calculated as $\nu^P = n_{ph}/(V\Delta t)$.

In order to save computer time, if just before particular propagation of a ray its value $Q = Q_k$ or $Q = Q_l$ "seems too small" to the code ($Q < Q_{min}$) (e.g. the threshold $Q_{min} = 1$ J can be assigned.) this 'weak' ray is not emitted. Instead, its accumulator is cleared and its photons of amount N_{ph} are added to the bremsstrahlung j-accumulator of suitable range: $\varepsilon_j \le \varepsilon_r < \varepsilon_{j+1}$. In order to provide energy conservation in the calculations, small excess energy $(\varepsilon_r - (\varepsilon_j + \varepsilon_{j+1})/2)N_{ph}$ (that can be negative) is simultaneously added to some additional energy accumulator Q_e, to be used later for compensating heating of free electrons of the layer.

Thus in the output plots of Monte-Carlo spectrum of emitted radiation, the line and recombination weak contributions can sometimes be seen on the bremsstrahlung background. To resolve more details, the value of Q_{min} should be decreased (thus increasing the computer time). It is also to note that to achieve the energy conservation the radiation stored at the mentioned first sub-step is simultaneously subtracted from the accumulator Q_e, and after calculating the line- and recombination photon amounts N_{ph}, the energy accumulator Q_e is added by $N_{ph}E_l$ and $N_{ph}I_{zk}$, respectively, and thus the changes of N_{zk} with the frequencies ν_{ph} are accounted in the energy balance. Here E_l is the level transition energy: $E_l = E_{k2} - E_{k1}$, with k_1 and k_2 the indices of upper and lower transition levels. The ionization potential I_{zk} determines the energy of transition $(z,k) \to (z{+}1,0)$. The other contribution to the transition frequencies is due to direct impacts of electrons on the ions as it determine Eq.(3) and Eq.(4).

The random photon energy ε_r is generated as follows. For the bremsstrahlung j-accumulator ε_r is uniformly distributed over the interval $(\varepsilon_j, \varepsilon_{j+1})$. The recombination accumulator (mzk) emits all photons at some ε_r in the interval $I_k \le \varepsilon < \min(\varepsilon_{max}, AI_k)$. Here I_k is the ionization potential, ε_{max} the energy used in Eq.(12), and a large numerical factor A determines reasonable energy range of recombination photons (e.g. $A = 10$). The random distribution corresponds to the photorecombination cross-section dependence on ε. The line radiation accumulator (mzl) emits the radiation for one random value ε_r distributed as it is

explained below in the narrow interval $E_l - B\Delta\varepsilon_l/2 < \varepsilon < E_l + B\Delta\varepsilon_l/2$, with a large numerical factor B for the "wings" of the lines.

The total absorption coefficient κ' of Eq.(7) is calculated for the random energies ε_r. The heat $\delta Q = Q(s_i) - Q(s_{i-1})$ produced at the second sub-step is accounted for the different mechanisms proportionally to the fractions ϕ in the absorption coefficients κ'_j κ'_l and κ'_{zk}: the bremsstrahlung sinks $\phi_j\delta Q$ with j for $\varepsilon_j \le \varepsilon_r < \varepsilon_{j+1}$ and $\phi_j = \kappa'_j/\kappa'$, the recombination's sinks $\phi_{zk}\delta Q$ with $I_k < \varepsilon_r < \min(\varepsilon_{\max}, AI_k)$ and $\phi_{zk} = \kappa'_{zk}/\kappa'$, and the line's sinks $\phi_l\delta Q$ with $\phi_l = \kappa'_l/\kappa'$ when ε_r gets into the narrow line shape vicinity of E_l. The absorbed radiations is immediately added to the accumulator Q_e and then, after calculating the absorbed photon amounts n_{ph} for line- and recombination mechanisms, the corresponding photoexcitation and photoionization frequencies $\nu^P = n_{ph}/(V\Delta t)$ are obtained, and Q_e is subtracted by $n_{ph}E_l$ and $n_{ph}E_{zk}$, similarly as it was done at the first sub-step.

19. The algorithm for electron level populations

The system of equations for level population densities Eq.(18.2) is not independent for each atomic kind m, because the equation are coupled due to the electron density n_e. Nevertheless, formally we can focus on only one atomic kind and omit the index m ($n_{mzk} \rightarrow n_{zk}$). Now we explain the TOKES algorithm for the solving of Eq.(1). This is a stable solver that calculates the available transitions (including those among the excited ion states) for arbitrary time step τ. Different processes that drive the populations can be represented in terms of corresponding transition frequencies. The system for the population densities, n_{zk}, acquires the form of a sum on the excitation/deexcitation and ionization/recombination transition rates:

$$\frac{dn_{zk}}{dt} = \sum_{k'=0}^{k-1}\left(\nu_{zk'k}^e n_{zk'} - \nu_{zk'k}^d n_{zk}\right) + \sum_{k'=k+1}^{K_z}\left(\nu_{zkk'}^d n_{zk'} - \nu_{zkk'}^e n_{zk}\right)$$

$$+\nu_{zk}^r n_{z+1,0} - \nu_{zk}^i n_{zk} + \delta_{k0}\sum_{k'=0}^{K_{z-1}}\left(\nu_{z-1,k'}^i n_{z-1,k'} - \nu_{z-1,k'}^r n_{z0}\right)$$

(19.1)

The Kronecker delta $\delta_{k0} = 1$ if $k = 0$ else $\delta_{k0} = 0$. The frequencies, ν, are the sums of electron- and photon impact frequencies ($\nu = \nu^E + \nu^P$). The recombination and ionization transitions between the ground states of each $z+1$-ions and all levels of z-ions are accounted for in the radiation sub-step ($z_1 \le z \le z_2$, $0 \le k \le K_z$). The maximum level population index K_z and the limiting charge state indices z_1 and z_2 are updated after each time step.

Eq.(1) is numerically solved using an implicit scheme with the derivative approximated as $dn/dt \to (n(t+\tau) - n(t))/\tau$. Introducing for the resonance processes square matrices $\mathbf{a}_z$ such that $a_{zkk} = 1$, $a_{zk'k} = \tau v_{zk'k}^e$ $(k' < k)$, $a_{zkk'} = \tau v_{zk'k}^d$ $(k' > k)$, additional designations $r_{zk} = \tau v_{zk}^r$ and $i_{zk} = \tau v_{zk}^i$ for the ionization and recombination processes, designating $n = n(t+\tau)$ and $\widehat{n} = n(t)$, we rewrite Eq.(1) in the rather compact form:

$$-\delta_{k0} \sum_{k'=0}^{K_{z-1}} i_{z-1,k'} n_{z-1,k'} + \left(\begin{array}{c} \sum_{k'=0}^{K_z} a_{zkk'} + i_{zk} \\ + \delta_{k0} \sum_{k'=0}^{K_{z-1}} r_{z-1,k'} \end{array} \right) n_{zk} - \sum_{\substack{k'=0 \\ k' \neq k}}^{K_z} a_{zk'k} n_{zk'} - r_{zk} n_{z+1,0} = \widehat{n}_{zk} \qquad (19.2)$$

Let's now assume the states (zk) in are the states of top charge state $z = z_2$, so that the terms of transitions to $z+1$ are absent or can be neglected. For the top states Eq.(2) takes the form:

$$-\delta_{k0} \sum_{k'=0}^{K_{z-1}} i_{z-1,k'} n_{z-1,k'} + \left(\sum_{k'=0}^{K_z} a_{zkk'} + \delta_{k0} \sum_{k'=0}^{K_{z-1}} r_{z-1,k'} \right) n_{zk} - \sum_{\substack{k'=0 \\ k' \neq k}}^{K_z} a_{zk'k} n_{zk'} = \widehat{n}_{zk} \qquad (19.3)$$

The calculation consists of a sequence of similar steps. At first the higher excited state population density n_{zK} $(K \equiv K_z)$ is eliminated. The equation for n_{zK} reads (assume $K > 0$):

$$n_{zK} \Delta_{zK} - \sum_{k'=0}^{K-1} a_{zk'K} n_{zk'} = \widehat{n}_{zK}, \qquad \Delta_{zK} = \sum_{k'=0}^{K} a_{zKk'} \qquad (19.4)$$

From Eq.(4) we have for n_{zK} the expression in terms of the variables $n_{zk'}$ with $k' < K$:

$$n_{zK} = \frac{\widehat{n}_{zK}}{\Delta_{zK}} + \sum_{k'=0}^{K-1} \frac{a_{zk'K}}{\Delta_{zK}} n_{zk'} \qquad (19.5)$$

We substitute this expression into Eq.(3) at $k < K$:

$$-\delta_{k0} \sum_{k'=0}^{K_{z-1}} i_{z-1,k'} n_{z-1,k'} + \left(\sum_{k'=0}^{K-1} a_{zkk'} + a_{zkK} + \delta_{k0} \sum_{k'=0}^{K_{z-1}} r_{z-1,k'} \right) n_{zk} - \sum_{\substack{k'=0 \\ k' \neq k}}^{K-1} a_{zk'k} n_{zk'}$$

$$-a_{zKk} \left(\frac{\widehat{n}_{zK}}{\Delta_{zK}} + \sum_{\substack{k'=0 \\ k' \neq k}}^{K-1} \frac{a_{zk'K}}{\Delta_{zK}} n_{zk'} + \frac{a_{zkK}}{\Delta_{zK}} n_{zk} \right) = \widehat{n}_{zk} \qquad (19.6)$$

Now we distribute the three terms of substituted n_{zK} over some terms of Eq.(6):

$$-\delta_{k0} \sum_{k'=0}^{K_{z-1}} i_{z-1,k'} n_{z-1,k'} + \left(\sum_{\substack{k'=0 \\ k' \neq k}}^{K-1} a_{zkk'} + a_{zkk} + a_{zkK} \left(1 - \frac{a_{zKk}}{\Delta_{zK}} \right) + \delta_{k0} \sum_{k'=0}^{K_{z-1}} r_{z-1,k'} \right) n_{zk}$$

$$-\sum_{\substack{k'=0 \\ k' \neq k}}^{K-1} \left(a_{zk'k} + \frac{a_{zKk} a_{zk'K}}{\Delta_{zK}} \right) n_{zk'} = \widehat{n}_{zk} + a_{zKk} \frac{\widehat{n}_{zK}}{\Delta_{zK}} \qquad (19.7)$$

67

The negative term a_{zKk}/Δ_{zK} in Eq.(7) cannot change the positive sign of the expression $1 - a_{zKk}/\Delta_{zK}$ in the braces, because we have:

$$1 - \frac{a_{zKk}}{\Delta_{zK}} = 1 - \frac{\displaystyle\sum_{k'=0}^{K} a_{zKk'} - a_{zKk}}{\Delta_{zK}} = \frac{\displaystyle\sum_{\substack{k'=0 \\ k' \neq k}}^{K-1} a_{zKk'} + a_{zKK}}{\Delta_{zK}} \tag{19.8}$$

After distributing the terms of this expression inside the braces, Eq.(7) reads:

$$-\delta_{k0} \sum_{k'=0}^{K_{z-1}} i_{z-1,k'} n_{z-1,k'} + \left(a_{zkk} + \frac{a_{zKK}}{\Delta_{zK}} a_{zkK} + \sum_{\substack{k'=0 \\ k' \neq k}}^{K-1} \left(a_{zkk'} + \frac{a_{zkK}}{\Delta_{zK}} a_{zKk'} \right) + \delta_{k0} \sum_{k'=0}^{K_{z-1}} r_{z-1,k'} \right) n_{zk}$$

$$-\sum_{\substack{k'=0 \\ k' \neq k}}^{K-1} \left(a_{zk'k} + \frac{a_{zk'K}}{\Delta_{zK}} a_{zKk} \right) n_{zk'} = \widehat{n}_{zk} + a_{zKk} \frac{\widehat{n}_{zK}}{\Delta_{zK}} \tag{19.9}$$

In the calculations the values stored in $a_{zkk'}$ and $\widehat{n}_{zk}$ are then modified at $k < K$ as

$$a_{zkk'} + \frac{a_{zkK}}{\Delta_{zK}} a_{zKk'} \rightarrow a_{zkk'} \qquad (k \neq k'), \qquad a_{zkk} + \frac{a_{zKK}}{\Delta_{zK}} a_{zkK} \rightarrow a_{zkk}, \tag{19.10}$$

$$\widehat{n}_{zk} + a_{zKk} \frac{\widehat{n}_{zK}}{\Delta_{zK}} \rightarrow \widehat{n}_{zk} \tag{19.11}$$

Thus Eq.(9) acquired the form of Eq.(3):

$$-\delta_{k0} \sum_{k'=0}^{K_{z-1}} i_{z-1,k'} n_{z-1,k'} + \left(\sum_{k'=0}^{K-1} a_{zkk'} + \delta_{k0} \sum_{k'=0}^{K_{z-1}} r_{z-1,k'} \right) n_{zk} - \sum_{\substack{k'=0 \\ k' \neq k}}^{K-1} a_{zk'k} n_{zk'} = \widehat{n}_{zk} \tag{19.12}$$

We conclude that after eliminating n_{zK} the other equations of z acquired the form which is the form of initial equations as if the number of excited states would be one state less than we actually have, but with the modifications Eq.(10) and Eq.(11).

Those calculations are done by the code as the first step of the iterative process of sequential elimination of n_{zk}. As a result of such iterations the equation of z at $k = 0$ (so that with $K = 1$ from previous iteration) follows as

$$-\sum_{k'=0}^{K_{z-1}} i_{z-1,k'} n_{z-1,k'} + \left(a_{z00} + \sum_{k'=0}^{K_{z-1}} r_{z-1,k'} \right) n_{z0} = \widehat{n}_{z0} \tag{19.13}$$

Eq.(13) allows elimination of n_{z0} and thus the continuation for the charge states of $z-1$:

$$n_{z0} = \frac{\widehat{n}_{z0}}{D_z} + \sum_{k'=0}^{K_{z-1}} \frac{i_{z-1,k'}}{D_z} n_{z-1,k'}, \qquad D_z = a_{z00} + \sum_{k'=0}^{K_{z-1}} r_{z-1,k'} \tag{19.14}$$

For the states of $z-1$, Eq.(2) reads (after the elimination of n_{z0}):

$$-\delta_{k0} \sum_{k'=0}^{K_{z-2}} i_{z-2,k'} n_{z-2,k'} + \left(\sum_{k'=0}^{K_{z-1}} a_{z-1,kk'} + i_{z-1,k} \left(1 - \frac{r_{z-1,k}}{D_z} \right) + \delta_{k0} \sum_{k'=0}^{K_{z-2}} r_{z-2,k'} \right) n_{z-1,k}$$

$$-\sum_{\substack{k'=0 \\ k' \neq k}}^{K_{z-1}} \left(a_{z-1,k'k} + \frac{r_{z-1,k} i_{z-1,k'}}{D_z} \right) n_{z-1,k'} = \widehat{n}_{z-1,k} + r_{z-1,k} \frac{\widehat{n}_{z0}}{D_z} \tag{19.15}$$

The expression $1 - r_{z-1,k}/D_z$ remains positive:

$$1 - \frac{r_{z-1,k}}{D_z} = \frac{a_{z00}}{D_z} + \sum_{\substack{k'=0 \\ k' \neq k}}^{K_{z-1}} \frac{r_{z-1,k'}}{D_z} \tag{19.16}$$

Eq.(15) acquires the form:

$$-\delta_{k0} \sum_{k'=0}^{K_{z-2}} i_{z-2,k'} n_{z-2,k'} + \left(\begin{array}{c} a_{z-1,kk} + \dfrac{i_{z-1,k}}{D_z} a_{z00} + \displaystyle\sum_{\substack{k'=0 \\ k' \neq k}}^{K_{z-1}} \left(a_{z-1,kk'} + \dfrac{r_{z-1,k'} i_{z-1,k}}{D_z} \right) \\[2mm] + \delta_{k0} \displaystyle\sum_{k'=0}^{K_{z-2}} r_{z-2,k'} \end{array} \right) n_{z-1,k}$$

$$-\sum_{\substack{k'=0 \\ k' \neq k}}^{K_{z-1}} \left(a_{z-1,k'k} + \frac{r_{z-1,k} i_{z-1,k'}}{D_z} \right) n_{z-1,k'} = \widehat{n}_{z-1,k} + r_{z-1,k} \frac{\widehat{n}_{z0}}{D_z} \tag{19.17}$$

Then at the beginning of the step for $z-1$ we make the following modifications:

$$a_{z-1,k'k} + \frac{r_{z-1,k} i_{z-1,k'}}{D_z} \to a_{z-1,k'k} \quad (k' \neq k), \qquad a_{z-1,kk} + \frac{i_{z-1,k}}{D_z} a_{z00} \to a_{z-1,kk} \tag{19.18}$$

$$\widehat{n}_{z-1,k} + \frac{r_{z-1,k}}{D_z} \widehat{n}_{z0} \to \widehat{n}_{z-1,k} \tag{19.19}$$

After these modifications Eq.(17) acquires the form as if would be no transitions to the higher charge state (z), which we can see comparing it with Eq.(3):

$$-\delta_{k0} \sum_{k'=0}^{K_{z-2}} i_{z-2,k'} n_{z-2,k'} + \left(\sum_{k'=0}^{K_{z-1}} a_{z-1,kk'} + \delta_{k0} \sum_{k'=0}^{K_{z-2}} r_{z-2,k'} \right) n_{z-1,k} - \sum_{\substack{k'=0 \\ k' \neq k}}^{K_{z-1}} a_{z-1,k'k} n_{z-1,k'} = \widehat{n}_{z-1,k} \tag{19.20}$$

Then the code repeats the described calculations for the remaining charge states and finally the calculation arrives at the last state with $z = Z \equiv z_2$ and $k = 0$. As we can conclude from Eq.(20), the last equation reads:

$$a_{Z00} n_{Z0} = \widehat{n}_{Z0} \implies n_{Z0} = \frac{\widehat{n}_{Z0}}{a_{Z00}} \tag{19.21}$$

Having obtained n_{Z0} the code performs the reverse process: it calculates iteratively all n_{zk} using Eq.(5) and Eq.(14).

It is worthwhile noting that the described algorithm does not use the subtraction operation. All summed terms are non-negative therefore degradation of accuracy is avoided,

which provides absolute stability and maximal accuracy. In particular, this algorithm embraces the three-diagonal matrix problems of plasma diffusion and thermal conductivity which are explained in Sec.11. That equations are the case of $K_z = 0$ for all z, where z indices the plasma layers.

20. Collisions of free electrons with ions and neutral atoms

The contributions to E^{ed} and E^{ir} of Eq.(18.3) and Eq.(18.4) which are shown with Eq.(19.1) describe the processes of excitation, deexcitation, ionization and recombination. Now we describe the terms due to the collisions of free electrons with ions and neutral atoms.

Resonance transitions: For an ion (or neutral atom) to emit a photon the transition energy $E_{mzl} = E_{mzk'} - E_{mzk}$ should be provided by some previous electron-ion excitation collision with the frequency v^{Ee}, and the reversed process implies the deexcitation frequency v^{Ed}. The frequencies are proportional to n_e. In the code TOKES as a basis for the collisional excitation frequencies a popular semi-empirical formula by van Regemorter is applied:

$$v_{mzl}^{Ee}\Big|_{\text{van Regemorter}}\left[\text{s}^{-1}\right] = F \times 3.2 \times 10^{-7}\, n_e f_{mzl} \frac{\text{Ry}}{E_{mzl}} \sqrt{\frac{\text{Ry}}{T_e}} \exp\left(-\frac{E_{mzl}}{T_e}\right) \qquad (20.1)$$

The factor F is a semi-empirical coefficient, f_{mzl} the oscillator strength of transition l and Ry the Rydberg constant. Below we usually omit some obvious indices such as m or z.

Applying such kind of data one should be sure that their accuracy is sufficient for adequate investigation of problem in question. Eq.(1) with the factor $F = 1$ doesn't guarantee the accuracy even of several tenth percent, but nevertheless for many applications this is appropriate information. The value $F = 1$ is recommended to use only for the collisions with neutral atoms ($z=0$) and for the ions ($z>0$) $F = 0.2$ seems most suitable Ref.[19]. In TOKES the values of F are obtained fitting the radiation losses of the corona model to the popular dependencies by D. Post (see Ref.[20]) as it is demonstrated in Sec.24.

For the deexcitation frequencies, due to the principle of detailed balance for the corresponding cross-sections (the Klein-Rosseland formula) additional data is not needed:

$$g_k \sigma_l^{Ee}(\varepsilon_e)\varepsilon_e = g_{k'}\sigma_l^{Ed}(\varepsilon_e - E_l)(\varepsilon_e - E_l) \qquad (20.2)$$

Here g_k are the statistical weights of the involved levels. Beneath the excitation threshold E_i of the impact energy ε_e the excitation cross-section σ_i equals zero. In TOKES models the free

electrons are always assumed to obey the Maxwell's distribution. The Maxwell's distribution function is given by

$$f_e^M(\varepsilon_e) = \frac{2}{\sqrt{\pi}} \frac{n_e}{T_e} \sqrt{\frac{\varepsilon_e}{T_e}} \exp\left(-\frac{\varepsilon_e}{T_e}\right)$$

(20.3)

In this case Eq.(2) gives the following relation between the frequencies ν^{Ed}_l and ν^{Ee}_l:

$$\nu_l^{Ed} = \int_0^\infty \sigma_l^{Ee}(\varepsilon_e) \sqrt{\frac{2\varepsilon_e}{m_e}} f_e^M(\varepsilon_e) d\varepsilon_e = \nu_l^{Ee} \frac{g_k}{g_{k'}} \exp\left(\frac{E_l}{T_e}\right)$$

(20.4)

If only the electron impact excitation and deexcitation processes are involved, from Eq.(4) at the stationary regime for Eq.(19.1) the Boltzmann's distribution for n_k follows:

$$\frac{n_{k'}^B}{g_{k'}} \exp\left(\Delta E_{k'}/T_e\right) = \frac{n_k^B}{g_k} \exp\left(\Delta E_k/T_e\right)$$

(20.5)

Here we used the symbol $\Delta E_{zk} = E_{zk} - E_{z0}$ for the transitions that involve the ion ground state.

Non-resonance transitions: The frequencies of ionizations and deexcitations are also related due to the detailed balance principle. With the Maxwellian electrons, the Saha formula for thermodynamic equilibrium levels populations expresses the detailed balance principle:

$$\frac{n_{z+1,0}^S n_e^S}{n_{zk}^S} = n^S \frac{g_{z+1,0}}{g_{zk}} \exp\left(-\frac{I_{zk}}{T_e}\right)$$

(20.6)

The upper index S denotes the equilibrium populations ('Saha populations'). The ionization potential for arbitrary level $I_{zk} = E_{z+1,0} - E_{zk}$. We term N^S the Saha density:

$$N^S = \frac{1}{4\pi^{3/2}} \frac{1}{r_B^3} \left(\frac{T_e}{\text{Ry}}\right)^{3/2}$$

(20.7)

Because of small Bohr radius $r_B = 5.29\times10^{-9}$ cm, N^S is large and fits to solid body density.

From Eq.(6) follows that at thermodynamic equilibrium actual ion distribution in the tokamak plasma reduces to a few charge states (the main ions). The main ions have the potentials I_{z0} significantly exceeding T_e: Indeed, if assuming in Eq.(6) both z- and $(z+1)$-ions to be the only main ions having comparable densities, the inequality $I_z/T_e \approx \ln(N^S/N_e^S) >> 1$ follows. If in Eq.(5) $k' = 0$ and $\Delta E_k \sim I_z$, then we get $n_{zk}^B << n_{z0}^B$ and $n_{z+1,k}^B << n_{z+1,0}^B$.

Eq.(6) provides a relation between the ionization and recombination frequencies. Assuming only ionization and recombination in the stationary regime for Eq.(19.1) and using Eq.(6) for elimination of $n_{z+1,0}$ and n_{z0}, we come to the equality:

$$\nu_{zk}^{Er} n^S \frac{g_{z+1,0}}{g_{zk}} \exp\left(-\frac{I_{zk}}{T_e}\right) = \nu_{zk}^{Ei} n_e$$

(20.8)

This formula is valid without assuming the Saha and Boltzmann distributions of n_{zk}. Thus, the electron collision ionization frequency only should be given. In TOKES the semi-empirical formula by Lotz for the excitation frequencies that comprises most important experimental information is basically applied:

$$\nu_{zk}^{\mathrm{Ei}}\Big|_{\mathrm{Lotz}}\left[\mathrm{s}^{-1}\mathrm{cm}^3\right] = 6\times10^{-6}\,\upsilon_z\left(\frac{1\,\mathrm{eV}}{I_{zk}}\right)^{3\!/\!2}\sqrt{\frac{T_e}{I_{nk}}}\exp\left(-\frac{I_{zk}}{T_e}\right)F\left(\frac{I_{zk}}{T_e}\right) \tag{20.9}$$

The parameter υ_z is the valence and the function $F(x)$ is a certain slowly varying function implemented in the code. At $x \ll 1$ we have $F(x) \to -x\ln x$ and at $x \gg 1$ we have $F(x) \to 1$. Alternative choice is the formula from Ref.[19]:

$$k_{zk}^{\mathrm{Ei}}\Big|_{\mathrm{NRL}}\left[\mathrm{s}^{-1}\mathrm{cm}^3\right] = \frac{10^{-5}}{6+T_e/I_{zk}}\left(\frac{1\,\mathrm{eV}}{I_{zk}}\right)^{3\!/\!2}\sqrt{\frac{T_e}{I_{zk}}}\exp\left(-\frac{I_{zk}}{T_e}\right) \tag{20.10}$$

In TOKES the geometric mean value $k^{\mathrm{Ei}} = (k_{\mathrm{Lotz}}k_{\mathrm{NRL}})^{1/2}$ is currently used.

Not only Eq.(1), Eq.(9) and Eq.(10) are employed. The database of TOKES contains the constants E_{mzk}, g_{mzk}, the oscillator strengths f_{mzl} ($l = kk'$) and the transition frequencies ν_{mzl} for resonance excitations and ν_{mzk} for the ionizations of atoms and ions by electron and photon collisions, which was collected using diverse sources and approximations. Some of the data sources are mentioned in Sec.22.

21. Photon-ion processes and bremsstrahlung radiation

In this section the spontaneous and induced radiation probabilities, the opacities and the photon relevant transition frequencies are explained, at first for the line- and recombination radiations. The detailed balance principle that relates the photodeexcitation and photorecombination frequencies is discussed. Also the bremsstrahlung and the cyclotron radiation are considered.

For any kind of photons involving transitions, there is a fundamental relation by Einstein between the probabilities w of emission and absorption of a photon in presence of some number N of identical photons of the transition: $w^{\mathrm{emi}}/w^{\mathrm{abs}} = (N+1)/N$. The number N expresses also the ratio $w^{\mathrm{ind}}/w^{\mathrm{spt}} = N$ of induced decay of excited quantum state followed by photon emission with some probability w^{ind} and the spontaneous decay with some probability w^{spt}. As we have $w^{\mathrm{emi}} = w^{\mathrm{spt}} + w^{\mathrm{ind}}$, it follows $w_{\mathrm{abs}} = w_{\mathrm{ind}} = w_{\mathrm{spt}}N$: Expressing the radiation flux

$I(\varepsilon,\mathbf{s})d\varepsilon d\Omega$ in terms of N for a unit volume cube oriented along the direction $\mathbf{s}$, one comes to the equality:

$$N = 4\pi \frac{\pi^2 c^2 \hbar^3}{\varepsilon^3} I(\varepsilon,\mathbf{s}) \qquad (21.1)$$

The number of different quantum states per 1 cm^3 is equal to n_k/g_k with n_k population density and g_k statistical weight of the state k. For the lower and upper states of the transition under consideration the rates r [cm^{-3}s^{-1}steradian^{-1}erg^{-1}] of the photo-processes follow as

$$r^{abs} = w^{abs} \frac{n_{low}}{g_{low}}, \qquad r^{spt} = w^{spt} \frac{n_{upp}}{g_{upp}}, \qquad r^{ind} = w^{ind} \frac{n_{upp}}{g_{upp}} \qquad (21.2)$$

The Einstein relations give the detailed balance principle:

$$\frac{g_{low} n_{upp}}{g_{upp} n_{low}} r^{abs} = r^{ind} = a^{spt} n_{upp} \frac{\pi^2 c^2 \hbar^3}{\varepsilon^3} I(\varepsilon,\mathbf{s}) \qquad (21.3)$$

The coefficient $a^{spt} = 4\pi r^{spt}/n_{upp}$ [s^{-1}erg^{-1}] is the spontaneous emission coefficient, which is the spontaneous emission rate for unit population density and the whole solid angle 4π. Thus, the absorption rate and induced emission rate are expressed in terms of the emission coefficient and the radiation intensity. The latter determines the angle distribution of induced photons and angle dependence of absorption. The introduced rates relate with the radiation flux emission coefficient β and the emission ability β' as

$$\beta = \frac{1}{4\pi} \varepsilon a^{spt} n_{upp}, \qquad \beta' = \beta + \varepsilon r^{ind} \qquad [\text{cm}^{-3}\text{s}^{-1}] \qquad (21.4)$$

For the absorption coefficient κ we have $\kappa I = \varepsilon r^{abs}$ and thus from Eq.(3) follows:

$$\kappa = a^{spt} \frac{\pi^2 c^2 \hbar^3}{\varepsilon^2} \frac{g_{upp}}{g_{low}} n_{low} \qquad [\text{cm}^{-1}] \qquad (21.5)$$

The integrals over photon energies involving the opacities allow obtaining the photon relevant transition frequencies of photoexcitation (v^{Pe}), photodeexcitation (v^{Pd}), photoionization (v^{Pi}) and photorecombination (v^{Pr}) as showed below for different kinds of radiation.

Line radiation: For the radiation lines indexed by $l \leftrightarrow (k_1,k_2)$, with k_1 the lower and k_2 the upper transition states, Eq.(3) takes the form:

$$\frac{g_{k1}}{g_{k2}} \frac{n_{k2}}{n_{k1}} r_l^{abs} = r_l^{ind} = A_l L_l(\varepsilon) n_{k2} \frac{\pi^2 c^2 \hbar^3}{E_l^3} I(\varepsilon,\mathbf{s}) \qquad (21.6)$$

The absorption and emission rates are expressed in terms of total probability of line spontaneous emission A_l (the Einstein A coefficient is the frequency of the acts of photon emission). There is a general relation between A_l and the oscillator strength f_l (see Ref.[21]):

$$A_l = 2\frac{c}{r_B}\frac{g_{k1}}{g_{k2}}\left(\frac{E_l}{m_e c^2}\right)^2 f_l \qquad\qquad [\text{s}^{-1}] \qquad\qquad (21.7)$$

The reference value (A_l with $E_l =$ Ry, $f_l = 1$ and $g_{k1} = g_{k2}$) reads $A_{\text{ref}} = 0.803 \times 10^{10}$ s^{-1}. It is worthwhile noting a sharp dependence of A_l on the ion charge state z: e.g. for hydrogen-like ions ($E_l \propto z^2$) we have $A_l \propto z^4$ for the same transitions ($f_l =$ constant).

The function $L_l(\varepsilon)$ [erg^{-1}] is the line shape normalized on 1 that describes the distribution of emission and absorption probabilities over the photon energy in some interval containing the excitation energy E_l. The line radiation opacities β, and κ' follow as

$$\beta_l = \frac{1}{4\pi} A_l L_l(\varepsilon) E_l n_{k2} \qquad\qquad [\text{cm}^{-3}\text{s}^{-1}] \qquad\qquad (21.8)$$

$$\kappa'_l = A_l \left(\frac{\pi c\hbar}{E_l}\right)^2 \hbar L_l(\varepsilon)\left(\frac{g_{k2}}{g_{k1}} n_{k1} - n_{k2}\right) \qquad\qquad [\text{cm}^{-1}] \qquad\qquad (21.9)$$

The frequencies of resonance processes read:

$$\nu_l^{\text{Pe}} = \frac{1}{N_{k1}}\int r_l^{\text{abs}} d\varepsilon d\Omega = \frac{g_{k2}}{g_{k1}}\frac{A_l}{E_l}\left(\frac{\pi c\hbar}{E_l}\right)^2 \int d\varepsilon \hbar L_l(\varepsilon)\int_{4\pi} I(\varepsilon,\mathbf{s})d\Omega \qquad\qquad (21.10)$$

$$\nu_l^{\text{Pd}} = A_l + \frac{1}{N_{k2}}\int r_l^{\text{ind}} d\varepsilon d\Omega = A_l + \frac{g_{k1}}{g_{k2}}\nu_l^{\text{Pe}} \qquad\qquad (21.11)$$

Eq.(11) gives the detailed balance relation for the line radiation. The Monte-Carlo approach of TOKES for radiation transport described in Sec.18 allows obtaining ν_l^{Pe} (and thus ν_l^{Pd}) because the random photon rays bring in the plasma layers the information for updating the frequencies. The rays simultaneously influence the level populations, which is most important for the resonance transitions in optically thick plasmas.

Photoionization and photorecombination: The recombination radiation opacities as well as ionization (ν^{Pi}) and recombination (ν^{Pr}) frequencies are obtained in terms of photoionization and spontaneous photorecombination cross-sections. These cross-sections are related due to the detailed balance principle (the Miln formula):

$$g_{z+1,0} m_e^2 |\mathbf{v}(\varepsilon_e)|^2 \sigma_{zk}^{\text{spt}}(\varepsilon_e) = g_{zk}\frac{\varepsilon^2}{c^2}\sigma_{zk}^{\text{Pi}}(\varepsilon) \qquad\qquad (21.12)$$

The electron velocity $\mathbf{v}$ relates with non-relativistic kinetic energy ε_e as $|\mathbf{v}| = (2\varepsilon_e/m_e)^{1/2}$. The index k in the cross-sections of photoionization (σ^{Pi}) and spontaneous photorecombination (σ^{spt}) indicates the participating energy state of less charged ion. The spontaneous photorecombination frequency reads:

$$v_{zk}^{\mathrm{spt}} = \int\limits_{0}^{\infty} d\varepsilon_e \sigma_{zk}^{\mathrm{spt}}(\varepsilon_e)(2\varepsilon_e/m_e)^{1/2} f_e^{M}(\varepsilon_e) \qquad [\mathrm{s}^{-1}] \qquad (21.13)$$

The photoionization frequency v^{Pi} is given by a similar formula but with speed of light c instead $\mathbf{v}$ and the photon distribution function f_{ph} instead the electron Maxwell's function f_e. The photon energy exceeds the ionization energy I_{zk}:

$$v_{zk}^{Pi} = \int\limits_{0}^{\infty} d\varepsilon \int\limits_{4\pi} d\Omega \sigma_{zk}^{Pi}(\varepsilon) c f_{ph}(\varepsilon, \mathbf{s}) = \int\limits_{I_{zk}}^{\infty} \sigma_{zk}^{Pi}(\varepsilon) \frac{d\varepsilon}{\varepsilon} \int\limits_{4\pi} I(\varepsilon, \mathbf{s}) d\Omega \qquad (21.14)$$

Using the Miln formula, the spontaneous photorecombination frequency Eq.(13) is also transformed to an expression containing σ^{Pi}:

$$v_{zk}^{\mathrm{spt}} = B_{zk} \int\limits_{I_{mzk}}^{\infty} \sigma_{zk}^{Pi}(\varepsilon) \varepsilon^2 \exp(-\varepsilon/T_e) d\varepsilon \qquad (21.15)$$

The coefficient B_{zk} is given by

$$B_{zk} = \frac{1}{\pi^2 c^2 \hbar^3} \frac{g_{zk}}{g_{z+1,0}} \frac{n_e}{n^S} \exp\left(\frac{I_{zk}}{T_e}\right) \qquad (21.16)$$

The induced emission becomes substantial in optically thick plasmas in which the photons approach the Planck's distribution Eq.(18.6) (it is to note that this case is far from tokamak plasmas). The recombination radiation absorption coefficient and emission ability follow as

$$\kappa_{zk} = \sigma_{zk}^{Pi}(\varepsilon) N_{zk}, \quad \beta'_{zk} = \beta_{zk} + B_{zk} N_{z+1,0} \sigma_{zk}^{Pi}(\varepsilon) \varepsilon^3 \exp\left(-\frac{\varepsilon}{T_e}\right) \frac{\pi^2 c^2 \hbar^3}{\varepsilon^3} I(\varepsilon, \mathbf{s}) \quad (21.17)$$

The induced photorecombination frequency can be obtained as:

$$v_{zk}^{\mathrm{ind}} = \frac{1}{N_{z+1,0}} \int r_{zk}^{\mathrm{ind}} d\varepsilon d\Omega = \int a_{zk}^{\mathrm{spt}} \frac{\pi^2 c^2 \hbar^3}{\varepsilon^3} I(\varepsilon, \mathbf{s}) d\varepsilon d\Omega \qquad (21.18)$$

The total photorecombination frequency $v^{Pr} = v^{\mathrm{spt}} + v^{\mathrm{ind}}$ then follows:

$$v_{zk}^{Pr} = B_{zk} \int\limits_{I_{mzk}}^{\infty} d\varepsilon \sigma_{zk}^{Pi}(\varepsilon) \varepsilon^2 \exp\left(-\frac{\varepsilon}{T_e}\right)\left(1 + \frac{\pi^2 c^2 \hbar^3}{\varepsilon^3} \int\limits_{4\pi} I(\varepsilon, \mathbf{s}) d\Omega\right) \qquad (21.19)$$

The photoionization cross-sections $\sigma^{Pi}(\varepsilon)$, which are used in the general expressions for v^{Pi} and v^{Pr}, have to be given for all energy levels (mzk). In TOKES diverse tabulated data are available, however for rather selected cases. Basically the Kramers' formula is used:

$$\sigma_{mzk}^{Pi}\Big|_{\mathrm{Kramers}} \left[\mathrm{cm}^2\right] = 7.9 \times 10^{-18} \frac{\upsilon_{mz}}{(z+1)^2} \left(\frac{I_{mzk}}{\varepsilon}\right)^3 \theta(\varepsilon - I_{mzk}) \qquad (21.20)$$

This expression is valid only for hydrogen atoms and the ions having one bound electron (hydrogen-like ions). Nevertheless, if the tabulated data are not available, the Kramers formula is used for other kinds of ions.

The induced recombination frequency allows closing the system of radiation transport equations. In particular, we checked the limit of thermodynamic equilibrium and indeed obtained the Boltzmann-Saha distribution for n_{mzk} and the Planck's distribution for $I(\varepsilon)$. It is also to note that the Kirchhoff's law (that is valid at the thermodynamic equilibrium) can be expressed in terms of the ratio β/κ. In case of line radiation we have then:

$$\frac{\beta_l}{\kappa_l} = \left(1 - \exp\left(-E_l/T_e\right)\right)I^P\left(E_l\right) \tag{21.21}$$

In case of recombination radiation we have similar expression:

$$\frac{\beta_{zk}}{\kappa_{zk}} = \left(1 - \exp\left(-\varepsilon/T_e\right)\right)I^P(\varepsilon) = \frac{2}{c^2}\left(\frac{\varepsilon}{2\pi\hbar}\right)^3 \exp\left(-\frac{\varepsilon}{T_e}\right) \tag{21.22}$$

The issue of dielectronic recombination: Thus far we dealt with the three-particle recombination $e+e+i_z \rightarrow i_{z-1} + e$. The probability of meeting two free electrons in a small vicinity of ion characterizes this process. In rare plasma this probability becomes small. It is worth noting that the decay $e+i_z \rightarrow i_{z-1}$ generally is not possible because of violating the law of momentum conservation. However, a special process of such type called dielectronic recombination (DR) Ref.[22] may provide a significant rate exceeding in rare plasma the three-particle recombination rate. At DR only two particles are initially involved: a slow free electron and an ion with at least one bound electron. (Thus fully stripped ions cannot acquire a bound electron due to DR).

The dielectronic recombination occurs as follows. At approaching to the attractive ion, the kinetic energy of initially slow free electron is significantly increasing, so that it can make an excitation of the ion. Due to this energy loss the electron becomes bound. Then the spontaneous photodeexcitation of the ion is fast occurring in which the emitted photon being the third particle provides the momentum conservation. Finally the ion remains in a state with the acquired bound electron. As the photon can take away only rather small momentum, the acquired electron occupies a rather highly excited energy level.

It reality DR is significant for plasmas being far from the thermodynamic equilibrium. Therefore the detailed balance ionisation process reversed to DR is not important and TOKES does not deal with. For more simplicity, DR (both the recombination frequency and the taken away photons) is implemented as an additional factor $(1+f_{DR})$ to the spontaneous photoionization cross-section σ^{Pi}. Due to this trick in the case of optically thick plasmas the

Saha equilibrium is still provided. Moreover, in TOKES the DR factor f_{DR} is used for fitting our radiation model to available exemplary results, which is demonstrated in Sec.24.

The bremsstrahlung radiation: The bremsstrahlung appears because the electrons elastically colliding with each other and the ions change their velocities. As it follows from the electromagnetic field theory, their accelerations (and slowing down) by ions are accompanied by emission or absorption of electromagnetic waves. At elastic collisions the internal states of ions do not change, and the free electrons are the only plasma component explicitly emitting and absorbing the photons. As a matter of fact, at non-relativistic electron velocities and not fully stripped ions the bremsstrahlung contributes negligibly in comparison with the recombination and line radiations (it contributes by a factor of order α^3, where $\alpha = e^2/\hbar c \approx 1/137$ is the fine structure constant). Nevertheless we account for it, because at large temperatures when the plasma becomes fully ionized (at $T_e > z^2 Ry$) in not magnetized plasma the bremsstrahlung remains the only radiation source.

The Maxwell's distribution of free electrons provides the validity of Kirchhoff's law for the bremsstrahlung opacities of formally isolated electron-photon subsystem:

$$\frac{\beta_B}{\kappa_B} = \left(1 - \exp\left(-\varepsilon/T_e\right)\right) I^P(\varepsilon) \tag{21.23}$$

For β_B we use the known expression:

$$\beta_B(\varepsilon) = \frac{16(\alpha r_B)^3}{3^{3/2}\sqrt{\pi}} \frac{Ry}{\hbar}\left(\frac{Ry}{T_e}\right)^{1/2} \exp\left(-\frac{\varepsilon}{T_e}\right) n_e \sum_{mz} z^2 g_{ff}(x) n_{mz} \tag{21.24}$$

The Gaunt factor $g_{ff} \sim 1$ s a slowly varying function of dimensionless parameter $x = z^2 Ry/T_e$ implemented in TOKES according to Ref.[23].

The cyclotron radiation: In magnetized plasma there is also the cyclotron radiation (CR) that in tokamaks can contribute approximately as the bremsstrahlung. So far we assumed the radiation to be the photons. However, at small photon energies of CR, electromagnetic wave model is most suitable. But for rough estimations the photon based approach can also be useful. The plasma with a constant temperature T is optically thin above photon energies ε exceeding some value ε_0 and optically thick at $\varepsilon < \varepsilon_0$. The radiation losses in the photon energy range $\varepsilon < \varepsilon_0$ per unit area of plasma surface are given by

$$q_r^P = \pi \int_0^E I^P(\varepsilon) d\varepsilon, \qquad q_r\big|_{\varepsilon < \varepsilon_0} = \frac{2\pi}{3}\frac{T}{c^2}\left(\frac{\varepsilon_0}{2\pi\hbar}\right)^3 \tag{21.25}$$

The upper limit $E = \varepsilon_0$, and Eq.(18.6) gives I^P. Eq.(25)$_2$ follows at $\varepsilon_0 \ll T$. For CR we can assume $\varepsilon_0/\hbar = \omega_{ce}$, where $\omega_{ce} = eB/m_e c$ the electron gyro-frequency.

For example, with $B = 5\,\text{T}$ and $T = 10\,\text{keV}$ we obtain $\omega_{ce} \approx 10^{12}\,\text{s}^{-1}$ (i.e. $\varepsilon_0 \sim 10^{-3}\,\text{eV} << T$) and $q_r|_{\varepsilon \propto \varepsilon_0} \approx 0.1\,\text{kW/m}^2$. In ITER the vessel surface area is about $850\,\text{m}^2$, which is larger than plasma area, so that we estimate the total losses from the optically thick region as $W_{\text{rad,thick}} < 0.1\,\text{MW}$, which is negligibly small, especially if taking into account wall reflection. This rough estimation guarantees small contribution of at least first order cyclotron modes, as well as all other modes of plasma oscillations with the frequencies that do not significantly exceed ω_{ce}, in particular the ion cyclotron harmonics. Assuming also the plasma density $n_e = 10^{20}\,\text{m}^{-3}$, we obtain the plasma frequency $\omega_{pe} = (4\pi n_e e^2/m_e)^{1/2} \approx 6 \times 10^{11}\,\text{s}^{-1}$. Thus near thermodynamic equilibrium, collective modes contribute negligibly to radiation losses.

In spite of expected small role of CR in ITER, CR is implemented in TOKES based on Ref.[24]. The synchrotron power without reabsorption is given by

$$\frac{dW_{\text{CR}}}{dt} = -\frac{\omega_{pe}^2 \omega_{ce}^2}{3\pi c^3} T_e \varphi, \qquad \varphi \approx \min\left(120\frac{t_e^{7/4}}{\sqrt{p_a}}, 1\right) \qquad (21.26)$$

The parameters are: $t_e = T_e/m_e c^2$, $p_a = (s\omega_{pe}/c)(\omega_{pe}/\omega_{ce})$, and $s \sim a$ (plasma minor radius).

22. Radiation database and level group approximation

The ground state ionization potentials $I_{nz} = E_{m,z+1,0} - E_{m,z,0}$ (with n the chemical number of isotope m) are available for all needed m and z (see Fig.1) Ref.[25]. However, only the data for the transitions from ground state to excited states of neutral atoms ($z = 0$) are usually known. The atomic data on resonance transitions (E_{mzk}, g_{mzk}, $E_{mzl'}$ and f_{mzl}) are taken from the database Ref.[26], but much is missing there even at $z = 0$. E.g. those of calcium to tantalum are hardly present but 74 (W), despite that that source seems most abundant and adequate. Therefore the lacking data of chemical numbers n' are obtained by extrapolations from available numbers n. At first, for ions ($z > 0$) scaling laws on the ratios $I_{n+z,z}/I_{n0}$ are applied along the isoelectronic sequences $n - z = \text{const}$ as recommended in Ref.[27] and, secondly, the same transition structure within a periodic group is assumed for the ionization potential scaled for all z along the isoelectronic sequences.
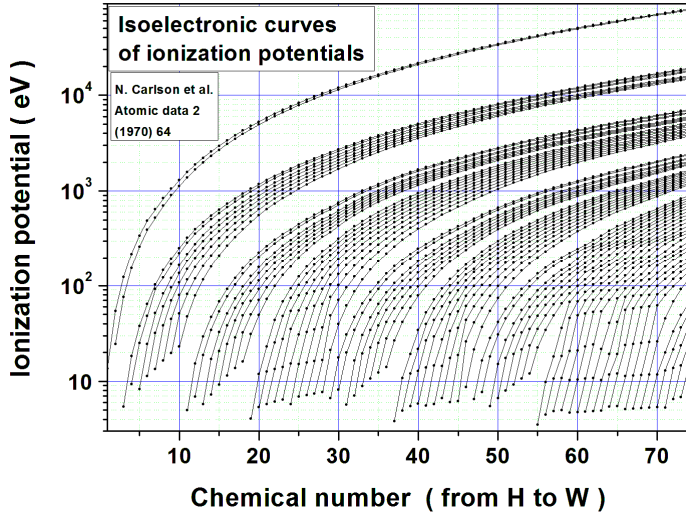
Fig. 22.1 Ionization potentials from H to W

It is stated in Ref.[27] that the ionization scaling $\sigma' = \sigma I^2$ can be used with σ the ionization cross section and I the ionization potential, and also the scaled energy $u = E/I$ can be introduced, where E is incident electron energy. At high energy the ionization cross section scales as $\sigma \propto u^{-1} \log u$. The normalized by $1/I^2$ ionization cross-sections y are plotted in Fig.2 and Fig.3. The interpolation by the formula shown in Fig.3 (where y is designated as σ) used the maximum ionization cross-section y_{max} that is revealed from Fig.2. Linear dependence of y_{max} on the isoelectronic index n: $n = 0, 1, 2$ etc. for H-like, He-like, Li-like ions etc., respectively, is assumed (see another formula on Fig.3). The coefficients $\sigma_{max}(0)$ and k on Fig.3 are obtained linearly fitting the available maximums of $y(n;\varepsilon)$ on Fig.2. The normalized electron impact energy ε_{max} at the maximums of $\sigma(n;\varepsilon)$ is obtained solely averaging ε_{max} of the cross-sections $y(n;\varepsilon)$.

The complexity of atomic data (see Fig.4) with characteristic level maximum index $K > 10^2$ prevents in reality direct multi-species self-consistent radiation transport simulations, and so many details may be not necessary in needed results. Simplification of the data is meaningful before performing radiation transport calculations. Therefore in TOKES the data is reduced Ref.[3].
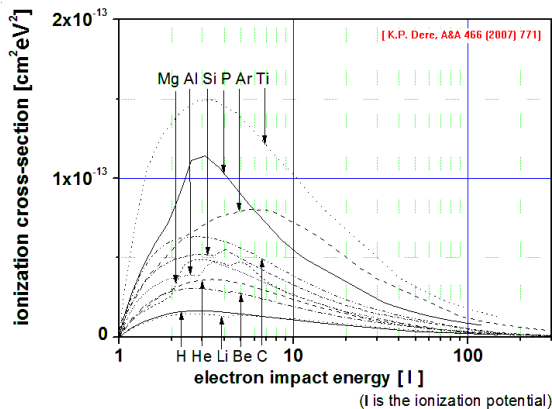
Fig. 22.2 Available ionization cross-sections normalized on the ionization potentials (eV) of isoelectronic sequences.
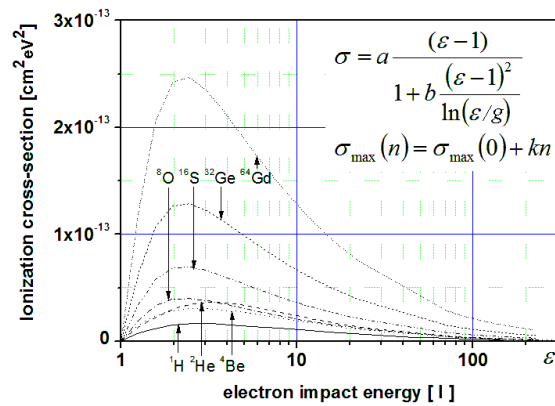
Fig. 22.3 Interpolated normalized ionization cross-sections for some isoelectronic sequences and their comparison with available cross-sections
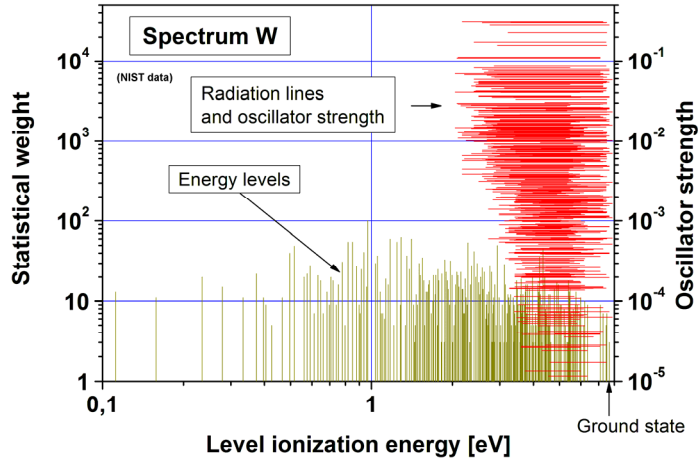
Fig. 22.4 Spectrum of tungsten (z = 0).

For each m and z, near energy levels k are grouped and a level group q $(q = 0..Q)$ is considered as one level of k in some range $k_{1q} \leq k \leq k_{2q}$. In the iterations the groups are built with the rule 'near levels are attracted and far levels are repulsed'.

Initially each level is one group, so that $Q = K$ and $k_{1q} = k_{2q} = k$. Then, the minimum 'distance' $\Delta E_k = |E_{k+1} - E_k|(g_{k+1} + g_k)$ between neighbour levels is determined and the two nearest levels (k and $k+1$) are joined in one group, thus $k_{1q} = k$, $k_{2q} = k + 1$ (for this group) and $Q = K-1$. This procedure is repeated for neighbouring groups, and the two next nearest groups merge until the needed reduction of Q. The 'distance' is defined as the product of the energy difference between the closest levels of neighbour groups, and the sum of the total weight of the levels of the neighbour groups, which prevents too large $k_{2q} - k_{1q}$. The numerous transitions among the levels are then reduced to a moderate number of most strong transitions among different groups. Final value of Q is chosen e.g. as $Q = [\sqrt{K}]$ ($[x]$ gives integer part of x). Finally the radiation transport equations are similarly reduced. The group statistical weight, the group centre E_q and the group width γ_q read:

$$ g_q = \sum_{k=k1q}^{k2q} g_k \,, \quad E_q = g_q^{-1} \sum_{k=k1q}^{k2q} g_k E_k \,, \quad \gamma_q = \left(g_q^{-1} \sum_{k=k1q}^{k2q} g_k \left(E_k - E_q \right)^2 \right)^{1/2} \quad (22.1) $$

The value of the group centre is used as the group level energy and, in particular, as the threshold of recombination radiation. The group width are used calculating the line shapes on the groups, by adding $\gamma_{qq'} = \gamma_q + \gamma_{q'}$ to the Doppler broadening γ_D of line radiation for a grouped resonance transition $q' \to q$. Thus at $\gamma_{qq'} > \gamma_D$ such the broadening sinks in relevance to the Doppler broadening and characterizes only the numerical grouping. At given group population density n_g, the level populations n_k inside this group are assumed to obey the Boltzmann's distribution, however in the limit $T_e \to \infty$, therefore $n_k = (g_k/g_q)n_q$ follows. Thus in TOKES algorithms the levels are in fact the groups.

After a grouping that involves the ground state (that of $k=0$), the 'ground state' group appears ($q = 0$). If several levels are grouped into the ground state group, it results in some change of the ionization potential because of a difference between E_q at $q = 0$ and E_k at $k = 0$;

thus in the group level approximation we generally assume $E_0 \neq 0$. Furthermore, we assume that the ionization and the recombination transitions occur not only between the ground state $(z+1,0)$ and any level (z,k) as it was assumed earlier, but they also involve any level of the ground state group, so that the ionization/recombination occurs between the levels (z,k) and $(z+1,k')$ at $k' = 0..k_{2g}$ and $g = 0$.

The level population equations Eq.(18.2) are grouped as

$$\frac{dN_{zq}}{dt} = \sum_{k=k1q}^{k2q} \left(S_{zk}^{ed} + S_{zk}^{ir} \right) \tag{22.2}$$

Summing the collisional and radiation transition frequencies as $\nu = \nu^E + \nu^P$ we obtained the averaged frequencies of the right hand side of Eq.(2). We assume a fast collisional process inside the groups and neglect radiative processes among the levels of same group, so that the balance principle would result in mutual cancelling those contributions. The group excitation-, deexcitation-, ionization- and recombination frequencies are given by

$$\nu_{qq'}^e = \frac{1}{g_q} \sum_{k=k1q}^{k2q} g_k \sum_{k'=k1q'}^{k2q'} \nu_{kk'}^e \;, \qquad \nu_{qq'}^d = \frac{1}{g_{q'}} \sum_{k'=k1q'}^{k2q'} g_{k'} \sum_{k=k1q}^{k2q} \nu_{kk'}^d \tag{22.3}$$

$$\nu_{zq}^i = g_{zq}^{-1} \sum_{k=k1q}^{k2q} g_{zk} \sum_{k'=0(z+1)}^{k2(q'=0)} \nu_{zkk'}^i \;, \qquad \nu_{zq}^r = g_{z+1,q'=0}^{-1} \sum_{k'=0(z+1)}^{k2(q'=0)} g_{z+1,k'} \sum_{k=k1q}^{k2q} \nu_{zkk'}^r \tag{22.4}$$

In Eq.(3), g' is the higher energy. The group averaged oscillator strength is given by

$$f_{qq'} = \sum_{k'=k1q'}^{k2q'} \left(\frac{1}{g_q} \sum_{k=k1q}^{k2q} g_k f_{kk'} \right) \tag{22.5}$$

We obtained also the detailed balance relations for the group collisional excitation- and deexcitation frequencies. (they are identical to the original formulas after substituting $k \rightarrow q$).

Radiation transport is also adapted to the grouped energy levels and the grouped resonance transitions, summing corresponding contributions to get the grouped opacities. The recombination radiation transport grouping resulted in formulas identical to the original ones (after the substitution $k \rightarrow q$) The grouped resonance emission and absorption coefficients are:

$$\beta_{qq'}(\varepsilon) = \sum_{k=k1q}^{k2q} \sum_{k'=k1q'}^{k2q'} \beta_{kk'} = \frac{1}{4\pi} A_{qq'} E_{qq'} n_q L_{qq'}(\varepsilon) \qquad [\text{cm}^{-3}\text{s}^{-1}] \tag{22.6}$$

$$\kappa_{qq'}' = \sum_{k=k1q}^{k2q} \sum_{k'=k1q'}^{k2q'} \kappa_{kk'}' = A_{qq'} \left(\frac{\pi c \hbar}{E_{qq'}} \right)^2 \hbar L_{qq'}(\varepsilon) \left(\frac{g_{q'}}{g_q} n_q - n_{q'} \right) \qquad [\text{cm}^{-1}] \tag{22.7}$$

The only what remains to be adapted to the grouped resonance transitions is the line shape. The requirement that $L_{qq'}(\varepsilon)$ doesn't depend on particular elementary transitions $(k' \rightarrow k)$ of

the groups q and q' means that the parameters of group line shape have to be all constructed from the group averaged parameters only. This averaging is also done in TOKES.

Simulating the radiation losses from the plasma, the bound electron levels ought to be grouped anyway, because of huge nomenclature of different lines which otherwise prevents 'finite time simulations' with conventional computers. However, it is worthwhile noting that the line averaging can completely deteriorate the shape function. Thus the level groups can be acceptable only for the problems in which the line shape profile is not principally important. For instance, for diagnostic purpose (the line spectroscopy) the grouping is not adequate. If the plasma in the line shape range becomes optically thick, this may also prevent the use of level groups, but the losses of radiation by the optically thin line wings can significantly improve the sense of using the averaged opacities. Finally, in the tokamak plasma only highly charged impurity ions remain not stripped of all electrons. Due to the strong dependence of the Einstein A coefficient Eq.(21.7) on z ($A_l \propto z^4$) the population densities of the excited levels become so low that the line radiation can be expected to be optically thin, which again justifies the level group approximation.

23. The shape functions of radiation lines

The theory of radiation line shapes is rather complex containing many different broadening mechanisms. It seems that this topic is still far from canonical forms, and an appropriate source remains an issue. Therefore for implementation in TOKES some limited approach is chosen. The code calculates the shifts energies ε of the line centre E_l for radiated photons. The physical effects of the line broadening are as follows.

1. **The Doppler broadening.** It appears due to thermal motion of the radiator (ion or neutral atom). The Doppler broadening width is $\gamma_D = (\upsilon_T/c)E_l$. The line shape function reads

$$L_D(\varepsilon) = \frac{1}{\sqrt{\pi}} \frac{1}{\gamma_D} \exp\left(-\frac{\varepsilon^2}{\gamma_D^2}\right) \tag{23.1}$$

Thermal velocity of ions $\upsilon_T = (2T/M)^{1/2}$ with T and M the temperature and mass of the ions.

2. **The natural broadening** due to finite lifetimes of the ionic states. It bases on the Heisenberg's quantum uncertainty principle applied for the energy states. The energy E_l presents with some uncertainty δE determined according to the estimation $\tau \delta E \sim \hbar$ by the time

τ of keeping the transition relevant levels k_1 and k_2. The natural broadening results in the profile described with the Lorentz function (here without the Stark effect):

$$L_L(\varepsilon) = \frac{\delta E_l}{2\pi} \frac{1}{\varepsilon^2 + (\delta E_l/2)^2} \tag{23.2}$$

The electron-ion and photon-ion collisions contribute to the natural broadening changing E_l. For example, the spontaneous photodeexcitation occurs with the frequency equal to the Einstein A coefficient A_l. If ignoring the contributions of the other processes, lifetime of the excited level is equal to $\tau = 1/A_l$, and thus the natural broadening is characterized by the line width $\delta E_l \sim \hbar A_l$. Generally all processes that can terminate given state contribute, with the frequencies of the states k_1 and k_2 including free electron and photon impacts. The terms which 'begin the life' of a state k don't influence δE_l. Thus it follows:

$$\delta E_{zl} = \hbar \sum_{k=k1,k2} \left(\sum_{k''=0}^{k-1} v_{zk''k}^d + \sum_{k''=k+1}^{K_z} v_{zkk''}^e + v_{zk}^i + \delta_{k0} \sum_{k''=0}^{K_{z-1}} v_{z-1,k''}^r \right) \tag{23.3}$$

3. **The Stark broadening** due to the influence of oscillating electromagnetic field upon bound electrons. Local electric field **D** itself accelerates the considered ion without influencing the transitions. The Stark effect is the splitting of degenerated energy levels $\Delta_S E$ because of lower atom symmetry in the field. It is so that either the splitting energy $\Delta_S E \propto D^2$ (the quadratic Stark effect) or $\Delta_S E \propto D$ (the linear Stark effect, for H-like ions only in the rare plasma typical of tokamaks). At the wings only ($\varepsilon \gg \delta E_S$) the line shape acquires the Lorentz profile: $L_S \propto 1/\varepsilon^2$. However in TOKES Eq.(2) is applied for the whole Stark broadening, after the modification $\varepsilon \to \varepsilon - \Delta E_{Sl}$. The dipole momentum of the radiator results in the shift $\delta E = \hbar C_2/r^2$ at the linear or $\delta E = \hbar C_4/r^4$ at quadratic Stark effect. The constant C_2 is approximately equal to $zn(n-1)e^2 r_B/\hbar$ with n the principal quantum number of H-like ion state, and the constants C_4 of different transitions are usually from 10^{-15} to 10^{-12} cm^4/s. At the quadratic Stark effect the line regular shift and the width are given by

$$\Delta E_{Sl} = 11.4 \hbar C_4^{2/3} v^{1/3} n, \qquad \delta E_{Sl} = \frac{\sqrt{3}}{2} \Delta E_{Sl} \tag{23.4}$$

with v the relative velocity of the interacting particles and n the projectile density.

For the TOKES applications the plasma parameters are always in the range of validity of these expressions as long as the quadratic Stark effect is involved. As to the linear Stark effect, there is no room for this approach which is based on binary collisions. In the opposite case an approach implying the collective electric field is appropriate, however it varies

stochastically and its distribution is hardly known. Therefore the linear Stark broadening is not implemented in TOKES so far.

4. **The Holtsmark broadening** (for H-like radiator ions) due to a quasistationary influence of ions surrounding the radiator. Direct calculations of local electric field from H−like ions of a charge z and density n on the radiator result in the symmetrical (on shift energy ε) distribution function $f_H(D)$ (the Holtsmark line shape):

$$L_H\left(\varepsilon\right) = \frac{C}{B_{zl}D_0}T_H\left(\beta\right), \qquad \beta = \frac{\varepsilon}{B_{zl}D_0}, \qquad B_{zl} \approx \frac{\hbar^2}{2zm_e e}\left(n_{k'}^2 - n_k^2\right) \qquad (23.5)$$

Here C is normalization constant, $D_0 = 2.60 \times zen^{2/3}$, $n_{k'}$ and n_k the principal quantum numbers of H-like radiator and z charge state of surrounding ions. The profile $T_H(\beta)$ is available in TOKES as a table for $\beta < 20$ and as $T_H = 1.771 \times |\beta|^{-5/2}$ for larger β.

Often several of these broadening mechanisms form the line profiles. If neglecting the correlations between the influencing effects, the convolution of different shapes can be used for obtaining final line shape. The natural and Stark broadening are the cases of the Lorentz broadening with corresponding resonance widths, γ_n and γ_S [erg] respectively. The resulting Lorentz width follows as the sum: $\gamma_L = \gamma_n + \gamma_S$. The Doppler and Lorentz broadening profiles, $L_D(\varepsilon)$ and $L_L(\varepsilon)$ respectively, are then convoluted:

$$L_V\left(\varepsilon\right) = \{L_L L_D\} = \int_{-\infty}^{+\infty} L_L\left(x\right)L_D\left(\varepsilon - x\right)dx \qquad (23.6)$$

Here ε is the photon shift energy coordinate with the origin at the line centre. The result (called the Voigt profile) is the real part of the Kramp function $w(z) = \exp(-z^2)\mathrm{erfc}(-\mathrm{i}z)$ with $z = x+\mathrm{i}y$, $x = \varepsilon/\gamma_D$ and $y = \gamma_L/(2\gamma_D)$. The Holtsmark profile $L_H(\varepsilon)$ is then convoluted with the Voigt profile resulting in the needed radiation line shape $L(\varepsilon) = \{L_V L_H\}$. Finally, some regular shift of the transition energy ΔE_S that appears in the Stark effect is to be taken into account, which additionally shifts the whole resulting profile.

In TOKES for the photon emission the Monte-Carlo approach explained in Sec.18 is applied. It allows the integrations Eq.(6) limited by some value a that depends on the resulting width: $-a < \varepsilon < a$ and $-a < x < a$. The generation of random ε with the final distribution functions $L(\varepsilon)$ is done. This technique demonstrates the convenience of random generators, and the shift ΔE_S is also included. At first four independent random numbers: ξ_n, ξ_S, ξ_D and ξ_H, homogeneously distributed over the interval $0 < \xi < 1$ are generated using the built-in random generator. The second, these numbers are used for producing random energies ε_n, ε_S, ε_D and ε_H for four mentioned line broadenings. Finally, the required random shift energy is

obtained by the summing: $\varepsilon = \varepsilon_n + \varepsilon_S + \varepsilon_D + \varepsilon_H$. The generation of the random contributions ε_A ($A = n, S, D, H$) is achieved solving the equations $F_A(\varepsilon_A) = \xi_A$, with $F_A(\varepsilon) = \int L_A(x)dx$ the integral distribution functions ($-a < x < \varepsilon$).

The energy level grouping introduced in Sec.22 is also applied for the line shapes, separately for each of considered broadening types. The Doppler broadening for the level groups q and q' consists of three contributions: two ones, γ_q and $\gamma_{q'}$, described by Eq.(22.1)$_3$ and the third one the conventional Doppler broadening Eq.(1). Thus, the whole group Doppler broadening takes the form:

$$L_{Dqq'}\left(\varepsilon\right) = \frac{1}{\sqrt{\pi}\gamma_{qq'}}\exp\left(-\frac{\varepsilon^2}{\gamma_{qq'}^2}\right), \qquad \gamma_{qq'} = \frac{\upsilon_T E_{q'q}}{c} + \gamma_q + \gamma_{q'} \tag{23.7}$$

The natural broadening Eq.(2) takes the form:

$$L_{Lqq'}\left(\varepsilon\right) = \frac{\delta E_{qq'}}{2\pi}\frac{1}{\varepsilon^2 + \left(\delta E_{qq'}/2\right)^2} \tag{23.8}$$

Respectively, Eq.(3) is correspondingly modified to use only group averaged parameters. The Stark broadening doesn't contain the parameters of involved levels so far therefore its averaging is not required until such parameters are applied. Finally the group Holtsmark broadening is based on the group averaged effective principal numbers n_q and $n_{q'}$ introduced by Eq.(5) in terms of corresponding level's parameters.

24. Validation of radiation model

For validations of the implemented radiation model, we used in TOKES so far the well known dependencies on electron temperature of radiation parameter, R, and ion mean charge produced by D. Post Ref.[20]. The code calculates the radiation power in a configuration with only one plasma unit and two magnetic layers, one of which has closed contour of $w = const$
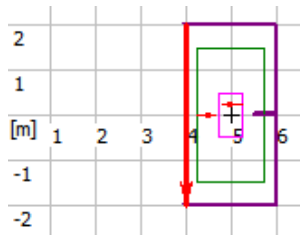
Fig. 24.1 The simple plasma configuration for TOKES validation

that carries the plasma unit, and the other layer does not carry plasma, because it ends at a special 'tooth' of the wall surface ('Tooth box' tokamak configuration, see Fig.1; the tooth is seen as the horizontal ledge at the right part of the wall.) Radiation power from the plasma and the mean charge of an isotope of interest are compared with the Post's data. Fig.2 shows such comparisons in case of carbon impurity.
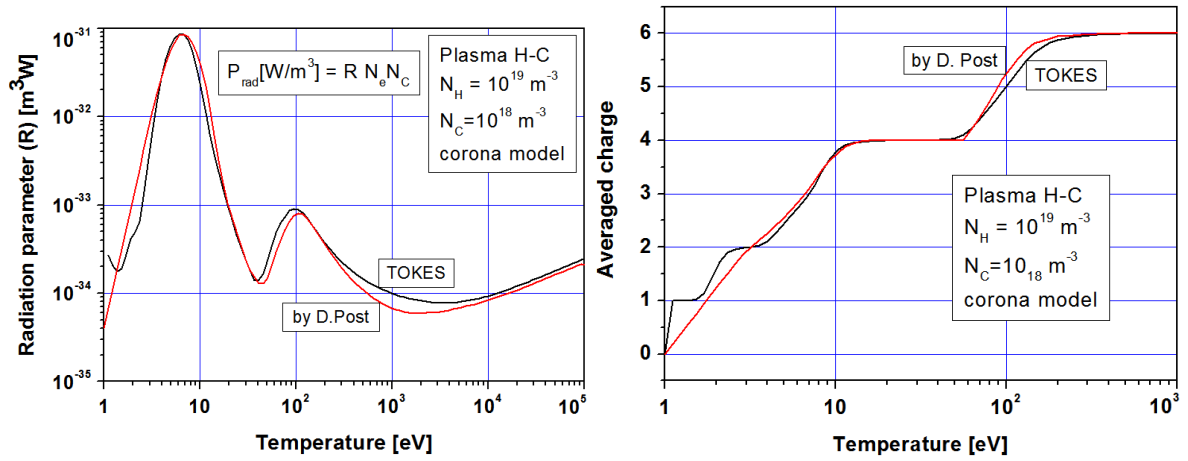
Fig. 24.2. Left: Fitting of radiation parameter of TOKES model. Right: Fitting of mean charge state. The good fitting was achieved with $F^{Ee}(C,z=0..5) = (5, 10, 12, 2, 1, 0.2)$.

The code calculates the total radiation power P_{rad} and divides it by the product of electron and isotope densities $N_e N_C$, which gives R (see Fig.2, left). The radiation due to H-ions is not subtracted, but N_H is taken small enough for neglecting the contribution of H.

The small difference between Post's data and TOKES results was achieved after some fitting of the collision excitation frequencies $\nu^{Ee}(m,z)$ (see Eq.(20.1)) and modelling parameters for dielectronic recombination, differently for each atom kind m and atom's charge state z, but equally for every bound electron level k.. In case of light atoms (from He up to C) only fitting for ν^{Ee} is sufficient, which is done multiplying the oscillator strength $f_{kk'}$ of Eq.(20.1) by additional factors $F^{Ee}(m,z)$, see in the caption of Fig.2. The particular fitting factors were found in not formal way, after many comparisons and testing of different values of $F^{Ee}(m,z)$ near those z at which the fitting was not yet satisfactory, until some 'visually acceptable' fitting achieved.

The atoms of atomic number larger than 6 (that of C), in addition require a fitting of dielectronic recombination effect. This was done only for Ne, Ar and W so far. It is to note that in the calculations the effect of dielectronic recombination was simulated simply increasing the photoionization cross-section by some factors $F_{DR}(m,z)$ as mentioned in Sec.21. As long as reabsorption of recombination radiation is not accounted for, this seems an acceptable simulation approach. It seems that this effect is unclear described (with the semi-empirical Burgess' formula, Ref.[22]) therefore we have feeling of free use of factors F_{DR} as the fitting factors.

At first for each m, $F_{DR}(m,z)$ were adjusted in the way similar to finding $F^{Ee}(m,z)$ however aiming only good fitting of the mean charge temperature dependence and not that of the radiation factor. As the second fitting step the factors F^{Ee} have been adjusted as well. During the 2nd step, the mean charge fitting can get worse, and it should be immediately

Fig. 24.3 Left: The fitting of radiation parameter for tungsten. Right: Fitting of mean charge state

improved with newly obtained and fixed values of F^{Ee}, after which 2nd step can be continued. Fig. 3 demonstrates the results for tungsten.

It is to note that the fitting factors can vary in very large range. Tables 1 and 2 demonstrate the fitting factors for those atoms in TOKES database for which the fitting was done so far. It is also to note that the Post's results for W are available only for rather high temperature range ($T \geq 100$ eV). For lower temperatures, we have 'extrapolated' the Post's curves in some as it seems reasonable way, aiming only to demonstrate that the fitting varying F^{Ee} and F_{DR} can be feasible in full required temperature range. Certainly, instead of Post's data some other exemplary data can be used for validation of TOKES radiation transport

Table 24.1   Fitting factors $f^{Ee}(m,z)$

N, atom number	M, atom symbol	$f^{Ee}(m,z)$ for $Z = [0..N-1]$
2	He	[0.2, 0.2]
3	Li	[1, 0.5, 0.2]
4	Be	[0.5, 0.6, 1, 0.2]
5	B	[3, 6, 4, 0.5, 0.3]
6	C	[5, 10, 12, 2, 1, 0.2]
10	Ne	[5, 10, 100, 50, 50, 15, 1.5, 0.2, 1.5, 0.2]
18	Ar	[5, 20, 200, 200, 200, 25, 3, 10, 10, 10, 20, 15, 5, 7, 5, 1, 1, 1]
74	W	[0.1, 0.2, 0.2, 0.4, 1.5, 0.3, 0.1, 0.2, 0.5, 2, 0.1, 0.2, 0.2, 0.005, 0.2, 0.2, 0.03, 0.03, 1, 5, 20, 50, 50, 50, 50, 50, 50, 50, 50, 20, 10, 5, 2, 1, 1, 0.15, 9.9, 9.9, 9.9, 9.9, 9.9, 9.9, 9.9, 9.9, 9.9, 9.9, 9.9, 7, 7, 7, 7, 7, 7, 0.05, 10, 10, 10, 10, 10, 10, 10, 10, 10, 10, 10, 20, 20, 20, 20, 20, 2, 1, 0.2, 0.2]

model.

Table 24.2   Fitting factors $f_{DR}(m,z)$

N, atom number	M, atom symbol	$F_{dr}(m,z)$ for $Z = [0..N{-}1]$
10	Ne	$[1, 10^2, 10^3, 200, 300, 10^2, 3.5, 10, 1, 1]$
18	Ar	$[1, 2, 10, 10^2, 10^3, 10, 2{\times}10^3, 10^3, 10^3, 500, 30, 30, 10^2, 10, 10, 1, 1, 1]$
74	W	$[2{\times}10^3, 10^3, 10^2, 10, 30, 20, 3, 30, 50, 10^2, 10^4, 2{\times}10^5, 5{\times}10^5, 5{\times}10^5,$ $10^5, 10^2, 3{\times}10^3, 600, 10^3, 5{\times}10^3, 10^3, 10^3, 2{\times}10^3, 5{\times}10^3, 7{\times}10^3, 10^4,$ $6{\times}10^3, 500, 200, 10^2, 10^2, 10^2, 200, 200, 10^2, 10^2, 500, 500, 500, 200,$ $200, 200, 200, 200, 200, 200, 50, 50, 50, 10, 5, 5, 20, 10^2, 50, 50,$ $50, 20, 10, 10, 10, 10^2, 300, 10^2, 300, 1, 1, 1, 1, 1, 1, 1, 1]$

Part V Processes in Scrape-Off Layer

25. Implementation of gyro-motion guiding centre model

Implementing the gyro-motion of charged particles (ions only so far) in TOKES we pursue the aim of the development of the code in the direction of kinetic plasma description, which should be important for simulation of alpha particle losses and for processes in SOL after ELMs in which the MHD model of Sec.3 is not adequate. The charged particles can be well described as toroidally symmetric 'gyro-rays' in the guiding centre approximation. (The atomic rays and photon rays are explained in Sec.16.) In TOKES the gyro-motion in the magnetic field $\mathbf{B}(x,y)$ is simulated calculating the path of charged particle across sequence of adjoined toroidal cells of triangle cross-section as one numerical step of the Monte-Carlo test for this particle. The particle of mass m and charge q enters some triangle, traverses it, enters next triangle and so continues the motion (particle-in-cell method). The crossing triangle sides takes into account such guiding centre model features as conservation of the leading centre coordinate x_c and motion integrals the adiabatic invariant I and the kinetic energy H (the Hamiltonian), which keeps the particle in small vicinity of a magnetic surface.

We follow the approach based on the Hamilton method for the magnetic flux frame (see Ref.[28]) but deduced necessary formulas assuming at the beginning the toroidal symmetry about the axis z. In the cylindrical coordinates the Hamiltonian has the form:

$$H\left(t,r,z,p_r,p_z,p_\zeta\right) = \frac{1}{2m}\left(\left(p_r - \frac{q}{c}A_r\right)^2 + \left(p_z - \frac{q}{c}A_z\right)^2 + \left(\frac{p_\zeta}{r} - \frac{q}{c}A_\zeta\right)^2\right) + q\varphi \quad (25.1)$$

The canonical momentum component p_ζ is the motion integral: along particle trajectory $p_\zeta =$ const. The canonical transformation formulas to moving curvilinear magnetic flux coordinates (x,y,ζ) with x a magnetic surface label and y a poloidal coordinate read:

$$p_1 = p_r \frac{\partial r}{\partial x} + p_z \frac{\partial z}{\partial x}, \qquad p_2 = p_r \frac{\partial r}{\partial y} + p_z \frac{\partial z}{\partial y}, \qquad H = H' + \frac{\partial \Phi}{\partial t} \quad (25.2)$$

Here new (covariant) momentums are p_1 and p_2, Φ is the generation function, and H' the new Hamiltonian (the designation nomenclature see in Sec.2, the apostrophe is omitted):

$$H = \frac{1}{2m}\left(\left(p_1 - \frac{q}{c}A_1\right)\left(p^1 - \frac{q}{c}A^1\right) + \left(p_2 - \frac{q}{c}A_2\right)\left(p^2 - \frac{q}{c}A^2\right) + \left(\frac{p_\zeta}{r} - \frac{q}{c}A_\zeta\right)^2\right) \quad (25.3)$$

$$+ q\varphi(t,x,y) - p_1 u^1 - p_2 u^2$$

With the magnetic potential of Sec.2: $\mathbf{A} = (0,\sqrt{g^{22}}A_2, w/r)$, Eq.(3) takes the form:

$$H = \frac{1}{2m}\left(\begin{array}{c} g^{11}(p_1)^2 + 2g^{12}p_1\left(p_2 - \frac{q}{c}A_2\right) \\ + g^{22}\left(p_2 - \frac{q}{c}A_2\right)^2 + \frac{1}{r^2}\left(p_\zeta - \frac{q}{c}w\right)^2 \end{array}\right) + q\varphi - p_1 u^1 - p_2 u^2 \quad (25.4)$$

The guiding centre model assumes small ratio of particle's gyro-radius ρ_g and the plasma size R ($\rho_g/R \ll 1$). All terms in Eq.(4) would have the same order of value, mv^2, if assuming the large variables A_2 and w be well compensated by p_2 and p_ζ: $p_2 \approx qA_2/c$ and $p_\zeta \approx qw/c$. The equation $p_\zeta = qw(t,x)/c$ gives the root $x = x_c(t)$ and thus at each moment the motion is localized in small vicinity of the magnetic surface of $w = (c/q)p_\zeta$. The point (x_c,y,ζ) is 'the leading centre'. The momentum p_2 is localized in small vicinity of the function $p_{2c}(t,y) = qA_2(t,x_c(t),y)/c$. The small deflections ξ and κ are introduced using symbolic factor $\varepsilon \equiv 1$ for small dimensionless terms: $x = x_c + \varepsilon\xi$ and $p_2 = p_{2c} + \varepsilon\kappa$. Expanding Eq.(4) on the powers of ε results in the guiding centre Hamiltonian (the term of H of zeroth order on ε):

$$H_0 = \frac{1}{2m}\left(\begin{array}{c} g^{11}(p_1)^2 + 2g^{12}p_1\left(\kappa - m\omega_g b_\zeta\sqrt{g}\xi\right) \\ + g^{22}\left(\kappa - m\omega_g b_\zeta\sqrt{g}\xi\right)^2 + \frac{g}{g_{22}}(m\omega_g b_y\xi)^2 \end{array}\right) + H_0^{(1)} \quad (25.5)$$

$$H_0^{(1)}(t,y) = q\left(\varphi - \int E_2 dy\right) + \frac{\partial x_c}{\partial t}\int m\omega_g b_\zeta\sqrt{g}\,dy - \frac{q}{c}A_2 u^2 \quad (25.6)$$

Here b_y and b_ζ are the components of unit vector $\mathbf{b} = \mathbf{B}/B$; the gyro-frequency $\omega_g = qB/(mc)$ and the poloidal electric field $E_2 = -(1/c)\partial A_2/\partial t$. The canonical pair (p_1,ξ) enters in H_0 as a quadratic form, which enables to transform H_0 to the phase-action canonical variables ϕ and I:

$$\phi = \omega_g t + \phi_0, \qquad I = \frac{1}{2\pi}\oint P dX \quad (25.7)$$

The integration is performed along the trajectory for one oscillation period in which ϕ increments by 2π. The transformation formulas read:

$$\xi = \frac{b_\zeta}{m\omega_g\sqrt{g}}\kappa + \sqrt{\frac{2Ig^{11}}{m\omega_g}}\sin\phi \quad (25.8)$$

$$p_1 = b_y^2\frac{g_{12}}{g_{22}}\kappa + \sqrt{\frac{2m\omega_g I}{g^{11}}}\left(\cos\phi - b_\zeta\frac{g_{12}}{\sqrt{g}}\sin\phi\right) \quad (25.9)$$

The Hamilton equations $dy/dt = \partial H_0/\partial \kappa$ and $d\kappa/dt = -\partial H_0/\partial y$ take the form:

$$\frac{dy}{dt} = \frac{\kappa}{\mu}, \qquad \frac{d\kappa}{dt} = -I\frac{\partial \omega_g}{\partial y} + \frac{1}{2}\left(\frac{\kappa}{\mu}\right)^2 \frac{\partial \mu}{\partial y}, \qquad \mu = \frac{g_{22}m}{b_y^2} \qquad (25.10)$$

Here μ describes the effective inertia of the particle in terms of metrics tensor component g_{22}.

In each triangle the local Cartesian rectangular frame (x,y) with x proportional to w as $w = w_c - hx$ is chosen, where h is a coefficient available as a constant in the particular triangle, and $w_c = w(x_c)$. The field **B** in the triangle in terms of $\omega = rB_\zeta$ reads:

$$b_y = \frac{h}{\sqrt{h^2 + \omega^2}}, \qquad b_\zeta = \frac{\omega}{\sqrt{h^2 + \omega^2}} \qquad B = \frac{1}{r}\sqrt{h^2 + \omega^2} \qquad (25.11)$$

The components g_{ik} in the triangle are: $g_{12} = 0$, $g_{11} = g_{22} = 1$, and $x_c = 0$. Both x and y are linear functions of r and z. During passing the triangle the point (x_c,y) remains inside the triangle, but the code does not check if the gyrating particle position (x,y) and the guiding centre position (x_d,y) are also inside, so that the visible particle trajectory can have some discontinuities at the moments of crossing triangle sides.

Eq.(11) shows that over the triangle b_y and b_ζ are constant, but $B \propto 1/r$. However, in the numerical step the constant value $r = r_c$ at the midst of the linear segment with $x = x_c$ inside the triangle is chosen and thus the integration of motion across the triangle corresponds to the constant B and ω_g. It is to note that in the x–points of tokamak separatrix the poloidal component b_y is vanishing and thus $h \to 0$ there, which is still a problem in TOKES, because in vicinity of extremes the mentioned discontinuities of trajectory become too large.

In the phase-action variables we have $H_0 = \omega_g(y)I + \kappa^2/2\mu(y)$. The particle coordinate x and the guiding centre x_d are given by (these formulas were used in Ref.[29]):

$$x = x_d + \rho_g\sqrt{\frac{g_{22}}{g}}\sin\phi, \qquad x_d = x_c + \frac{b_\zeta}{m\omega_g\sqrt{g}}\kappa, \qquad \rho_g = \sqrt{\frac{2I}{m\omega_g}} \qquad (25.12)$$

Eq.(10)$_1$ is integrated from the triangle entry position $\mathbf{p}_a$ as

$$y = y_a + (\phi - \phi_a)\frac{\kappa}{\omega_g\mu} \qquad (25.13)$$

Passing the triangle provides the triangle exit position $\mathbf{p}_b$, which does the routine of TOKES for contours of $w = $ const. In particular, this step results in corresponding phase difference $\phi_b - \phi_a$ and the length $l = |\mathbf{p}_b - \mathbf{p}_a|$ of leading centre path. Calculating gyro-oscillations we assume that ϕ is continuous across the border. The particle's toroidal angle ζ follows from the Hamilton equation $d\zeta/dt = \partial H_0/\partial p_\zeta$ in the form:

91

$$\frac{d\zeta}{d\phi} = \frac{1}{mr^2\omega_g}\left(p_\zeta - \frac{q}{c}w\right) \quad \Rightarrow \quad \zeta = \zeta_a + (\phi - \phi_a)\frac{b_\zeta b_y \kappa}{m\omega_g r_c} \tag{25.14}$$

If ω_g increases entering the next triangle, κ^2 can get negative (i.e. the inequality $\omega_g > H_0/I$ can be met), which means that the particle cannot enter the next triangle (magnetic mirror at the border). In this case the particle reverses the motion: $\kappa \rightarrow -\kappa$.

26. Simulation of stochastic perturbations of gyro-motion

When interactions of magnetized confined particle with other particles or collective plasma perturbations are taken into account, the gyro-motion parameters the energy H_0, the adiabatic invariant I and the toroidal canonical momentum p_ζ become not constant along the trajectory. In tokamak plasma those interactions cause relatively slow stochastic evolution of the motion integrals on the time scale Δt of one revolution of guiding centre trajectory on the poloidal plane (the banana period). However, after many poloidal cycles the small perturbations can change particle trajectory drastically. Due to the evolution of p_ζ the leading centre coordinate w_c 'diffuses' across the magnetic surfaces to the periphery region where the magnetic field line crosses the wall. That doesn't necessarily result in striking the wall, because the particle can still remain trapped due to the magnetic mirrors. As the ratio I/H_0 changes stochastically as well, eventually the mirror would get into the wall and then the particle contacts the wall within next cycle.

We assume that at each magnetic surface w the particle interacts with some thermostat of local temperature $T(w)$ that causes gradual approaching of the particle velocity distribution function to the local Maxwell's function Eq.(20.3). Characteristic time of the relaxation is assumed given as a function of w and the velocity: $\tau(w,\upsilon)$. In the core the thermostat represents the whole plasma including both transit and trapped ions and electrons, and on the periphery only other trapped particles, because they remain in SOL for relatively long time there (in comparison with the passing time).

After the numerical integration described in Sec.25 the poloidal period Δt becomes known ($\Delta t << \tau$). In the following stochastic motion modelling, the change of motion integrals is happening only ones during this small time step. To get the changes of H_0, I and p_ζ, new position $\mathbf{p} = (x,y,\zeta)$ and the velocity $\mathbf{v} = \upsilon_b\mathbf{b} + \upsilon_n\mathbf{n} + \upsilon_w\mathbf{w}$ of the particle are obtained after each poloidal cycle during which the motion is assumed without the interactions. (The orts $\mathbf{b}$,

n and **w** are introduced in Sec.4) Then the Gaussian random generator produces the 'destination Maxwell's velocity' $\mathbf{u} = (u_b, u_n, u_w)$, and **v** is updated as

$$\left(1 - \frac{\Delta t}{\tau}\right)\mathbf{v} + \frac{\Delta t}{\tau}\mathbf{u} \rightarrow \mathbf{v} \tag{26.1}$$

With given **p** and the corrected **v**, new motion integrals are calculated finalizing the cycle. If the new value of w_c does not remain inside the final triangle, the code tries to find the next triangle that contains w_c, seeking it as closer as possible to the direction of ∇w. If such a triangle is found but it adjoins the wall so that the contour $w = w_c$ ends at the wall, it means the end of calculation (the particle strikes the wall). Sometimes (near an extreme of $w(r,z)$) the required triangle is not found. This case the code interprets as a 'reflection' from the extreme: it inverts the signs of u_b and u_w and recalculates Eq.(1) which reproaches w_c from the extreme.

27. Simulation of processes in scrape-off layer

The model does not include transversal electric field therefore simple averaging over plasma species is undertaken as temporary solution. Both lost plasma and wall emitted atoms are important in SOL. These procedures are shortly described in Ref.[3]. The following features form the implementation.

Plasma buffers of x-points: As it is mentioned in Sec.10, at each numerical time step τ (e.g. $\tau = 0.01$ s) the amounts of multi-species plasma and the plasma energy to be dumped into SOL are temporarily accumulated in special numerical 'buffers' attached at each x-point that bound the plasma. Three buffers (A, B and C) associate with the x-point:

A) The buffer for collisional diffusion/thermoconductivity dumps at the plasma edge. This buffer is emptied after each time step.

B) The buffer for 'MHD activity' dumps of excess plasma when the beta limit (see Sec.7) is exceeded at some of plasma layers. This case represents the attempt to simulate ELMs that can appear as a result of violating the beta-limit. This buffer does not spend the accumulated plasma until the specified 'ELM energy' (one of TOKES input data) is accumulated. Then the time step reduces abruptly to $\tau = 0.01$ ms and the buffer is gradually ('droplet by droplet') emptied during a large amount of gradually increasing time steps within the specified 'ELM time' (then τ increases again up to 0.01 s).

C) The buffer that contains the plasma of the layer that was earlier looped but in the evolving magnetic field now contacts the wall. Getting not looped, the layer did not dump the

plasma it contains onto the wall. To avoid numerical effects of wall overheating, the plasma is moved into this buffer. After the next time steps the buffer is emptied during the long time $\delta t = (dw/dt)^{-1} \delta w$ ($\delta t \gg \tau$) with the derivative dw/dt at the x-point and δw the layer's width.

Simplified species model: The plasma 'droplets' which should be dumped after the time step from three buffers appear in SOL as the amounts N_m of atoms of kind m. The thermal and ionization energy of original plasma ions and electrons constitute the thermal energy E_m of these atoms. The electron thermal energy $(3/2)n_e T_e$ is distributed proportionally to the averaged charge states z_m of the original ions.

By this way we assume that when an atom m impacts on the wall it brings the kinetic energy E_m/N_m that contains already a) the contribution of electrons (this contribution the atom gains crossing a thin pre-surface sheath as explained in Sec.28) and b) the recombination contribution (the internal energy heats the wall surface).

The amount N_m is divided into a large number K (e.g. $K = 50$) of equal pieces. The pieces are distributed in front of the separatrix surface randomly and homogeneously on the poloidal Euclidian coordinate at some small distance from the separatrix (presently within 3 local gyro-ion radius of the averaged particles). The piece emerges in SOL as a gyro-particle with the leading centre at the random point, some random phase (from 0 to 2π), and the isotropic distribution on the velocity vector.

Species averaging: This gyro-particle comprises all ion species. The simulation of atom motion in SOL is performed with using the TOKES gyro-motion algorithm and assuming the atoms as charged particles of some averaged atomic mass M and the charge state Z (averaging is weighted proportionally to $\Delta N_m = N_m/K$ over m). The averaging aims for simulation of joined species dynamics in SOL, which without transversal electric field seems reasonable. The kinetic energy of the gyro-particle is equal to the sum (on m) of $\Delta E_m = E_m/K$ divided by $\sum_m \Delta N_m$. If in the course of the gyro-motion simulation a banana orbit is obtained, the code returns the piece $\{\Delta N_m, \Delta E_m\}$ for the next time step adding it into the buffer A. Otherwise the particle reaches the wall, heats it and vanishes at the surface in some special wall buffers for the species m, for following surface processes described in Sec.30.

Statistical description of SOL ions and SOL neutrals: In each triangle specially averaged neutral atom densities and temperatures and ion densities and temperatures are available, obtained accumulating the statistics of neutral atoms and ions passing the triangle in previous time steps. The statistics for SOL ions is done as follows. The gyro-particle tests allow calculation of averaged SOL plasma density. The particle passing time $\Delta\tau$ of a triangle is multiplied for each m by ΔN_m and the product $\Delta N_m \Delta\tau$ is accumulated in special triangle

associated accumulator. After the time step τ the accumulated product is divided by $V\tau$, with $V = rs$ the cell volume, r major radius of triangle centre and s the triangle's area.
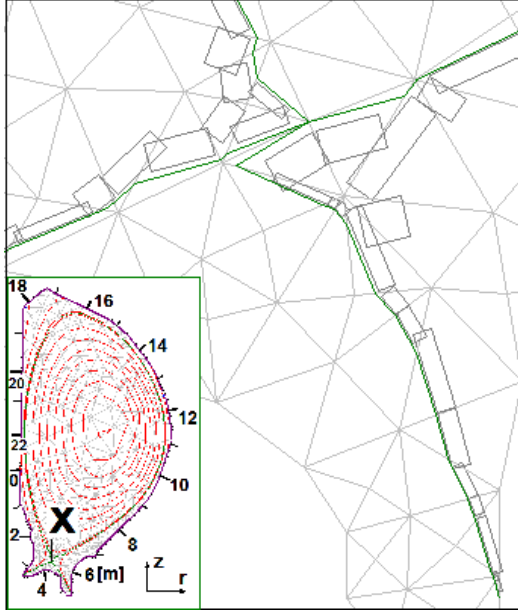

Fig.27.1 SOL in TOKES as rectangles attached to triangle meshes

We interpret the result as the actual ion density n_m in the triangle during the time step. The n_m is a stochastic parameter therefore some averaging over a number of time steps is reasonable. The averaged ion density $\bar{n}_m$ is updated after each time step as $(1 - \varepsilon)\bar{n}_m + \varepsilon n_m \rightarrow \bar{n}_m$ and saved also 'in the triangle'. For example, average period 1 s and $\tau = 0.01$ s corresponds to $\varepsilon = 10^{-2}$.

Also the similarly averaged values of energy density $(3/2)\bar{T}_m$, leading centre poloidal flux $\bar{w}_c$, length $\bar{L}$ and width $\bar{W}$ of SOL for the triangle are calculated. The $\bar{L}$ and $\bar{W}$ allow e.g. to plot SOL on the poloidal plane as a set of rectangular fragments over the triangles (see Fig.1).

Charge-exchanges and ionizations in SOL: The statistics for the rays of neutral atoms traversing the vessel is quite similar to the ion statistics. The availability of the averaged atomic densities $\bar{n}_a$ and atomic temperatures $\bar{T}_a$ in the triangles allows calculations of mutual transformations of ions of the piece $\{\Delta N_m, \Delta E_m\}$ and atoms of the ray $\{\Delta N_a, \Delta E_a\}$ due to the ionizations and charge-exchanges in SOL.

The charge-exchange (CX) in each triangle is simulated in the following way. The CX algorithm consists of two parts. First part calculates CX rate in terms of amount of ray atoms ΔN_a and the averaged ion densities $\bar{n}_m$. The atom ray passes through a triangle for a while $\Delta \tau_a$, meeting there the SOL ion density. The number of CX events follows as $\Delta N_{CX}^{(1)} = \frac{1}{2} k_{CX}\left(\bar{T}_m, \bar{T}_a\right)\Delta \tau_a \bar{n}_i \Delta N_a$, with k_{CX} the charge-exchange rate from TOKES database. Second part does similarly in terms of gyro-particles amount and the atom density $\bar{n}_a$: $\Delta N_{CX}^{(2)} = \frac{1}{2} k_{CX}\left(\bar{T}_a, \bar{T}_m\right)\Delta \tau \bar{n}_a \Delta N_m$ Physically both these contributions describe the same physical process of CX, therefore in each algorithm the factor ½ appears in the CX rate and their results are summed.

The ionization in SOL is also similarly modelled: the atom ray passes through a triangle meeting there quasineutral electron density $\bar{n}_e$. The number of ionization events is given by $\Delta N_{ion} = \frac{1}{2} k_{ion}\left(\bar{T}_e, \bar{T}_a\right) \Delta \tau_a \bar{n}_e \Delta N_a$, with k_{ion} the ionization rate from TOKES database. The $\bar{n}_e$ is constructed from the averaged ion densities and the electron temperature $\bar{T}_e$ is assumed as an averaged ion temperature. (The expected large difference between $\bar{T}_m$ and $\bar{T}_e$ is not yet accounted for in TOKES).

The new ions and the new atoms appeared after those events are accumulated (alone with their energy and momentum) in special buffers of triangle. At the end of time step the buffers are cleared in each triangle by emitting new atomic rays and the gyro-particle 'bunches'. The conservation of particle number for each kind m and a, energy and the toroidal momentum of neutral atoms is observed.

28. Plasma losses along magnetic field lines

In the course of the diffusion across a magnetic field B, confined plasma particles (ions and electrons) reach the plasma edge where field lines cross the vessel's surface. Let's consider how the particles are lost along magnetic field lines to the wall, We neglect the longitudinal electric field and the longitudinal electric current. In TOKES, a particle that escapes from the confinement region is assumed to have in average some kinetic energy E_a ($a = i$, e) at the edge. The velocity is thus given by $\upsilon_a = (2E_a/m_a)^{1/2}$. Given the length of the field line L, the ion escape time follows as $\tau_i = L/\upsilon_i$. Given averaged ion density n_i along the field line, the escape flux per unit volume there follows as $j_i = n_i/\tau_i$. Before entering the electric sheath (as discussed below), the ion comes in vicinity of wall keeping its energy E_i.

Alone with each ion of charge state z_i, the number of electrons z_i escapes from the confinement region and then arrives also at the wall vicinity. This number follows from the plasma quasineutrality, and for simplicity we do not account for the electrons emitted by the surface, which would typically require a large surface temperature. Due to large thermal velocity $\upsilon_e \gg \upsilon_i$ the electrons would try to come to the wall much faster than the ions. However, to maintain the quasineutrality of plasma bulk, a narrow electrostatic potential barrier (electric sheath) of a value $e\varphi$ in front of the wall surface prevents their fast escape at the 'ends' of field line on the wall surface, with φ the potential drop of the barrier. This potential difference accelerates positively charged ions, increasing their energy by $z_i e\varphi$.

As the result, the electron bounces many times ($\sim v_e/v_i$) along the field line in the potential well. Finally, after stochastic collisional increase of energy the electron overcomes the barrier and by this way penetrates through the sheath, to be absorbed by the wall. Thus the electron escape flux is due to the Fokker-Plank diffusion on their kinetic energy. The bouncing electrons can stochastically change energy by small portions after mutual collisions which occur with some frequency ν_e. We assume the electron free path $\lambda_e = v_e/\nu_e$ much larger than L. As the electrons are exchanging energy mutually colliding many times during the bouncing, they acquire some temperature T_e (i.e. $E_e = (3/2)T_e$). At $e\varphi \gg T_e$ the electron flux per unit volume into the energy region above $e\varphi$, which provides immediate escaping, can be estimated as $j_e = \nu_e n_e \exp(-e\varphi/T_e)$. The quasineutrality equation takes the form $j_e = \sum_i z_i j_i$. This is the equation for φ:

$$\exp\left(-\frac{e\phi}{T_e}\right) = \frac{\lambda_e}{L} \frac{1}{n_e} \sum_i \frac{v_i}{v_e} z_i n_i \,, \qquad n_e = \sum_i z_i n_i \qquad (28.1)$$

We see in Eq.(1) two dimensionless parameters ($\lambda_e/L \gg 1$ and $v_i/v_e \ll 1$) the magnitudes of which tend to compensate each other.

If the smallness of v_i/v_e dominates, the potential barrier exceeds T_e for a few times. The amount of energy which one escaping electron takes in the bulk from the bouncing electrons is approximately equal to $e\varphi$. However, mainly the accelerated ions bring the energy to the surface, because the escaping electrons after crossing the sheath arrive at the wall with small energies compared to E_e. If neglecting the small impact energy of electrons at the surface, we see that the electron energies are transferred into the escaping ion energies: the ion impact energy is equal to $E_i + z_i e\varphi$. This approach is applied in TOKES.

It is to note that in a very short system ($L \ll \lambda_e v_i/v_e$ or $\nu_e \tau_i \ll 1$) Eq.(1) cannot be applied because it would result in $e\varphi < T_e$ and thus in not dominating electron bounces. This means that in reality only the relation $\nu_e \tau_i \sim 1$ is feasible. The physical reason is development of electrostatic instabilities at the plasma edge which increases ν_e keeping some minimum $e\varphi_{min}$. We continue assuming $e\varphi_{min} \gg T_e$. In a tokamak namely this case is most typical, but a correct calculation of $e\varphi_{min}$ seems hardly possible. Therefore in TOKES we assume currently φ as given parameter (e.g. $e\varphi_{min}/T_e = 3$).

29. Kinetics of ionizations of neutral atoms

Implementing the ionization process in TOKES, we assume that a compact group of N_0 atoms traverses for some given time period τ a plasma cell of a volume V. The number N of atoms decreases due to ionizations by electron impacts. The multi-charge ionization rate $\langle\sigma_i\upsilon_e\rangle$ determines simultaneous ionization of Z electrons after impact of single electron on one atom, which results in producing one ion with the charge state Z. Here σ_i is the ionization cross-section and υ_e thermal velocity of electrons. The equations describing the dynamics of the populations read:

$$\frac{dN_e}{dt} = Z\frac{\langle\sigma_i\upsilon_e\rangle}{V}N_e\eta(N), \qquad N_e\big|_{t=0} = N_{e0}, \qquad \eta(x) = \begin{bmatrix} x, x > 0 \\ 0, x < 0 \end{bmatrix} \qquad (29.1)$$

$$N = N_0 - \frac{1}{Z}(N_e - N_{e0}) \qquad (29.2)$$

It follows that *rhs* Eq.(2) remains positive when the atoms traverse the cell. The electrons, if having sufficient temperature T_e, spend certain energy E_i per ionization of Z new electrons being cooled down as

$$\frac{d}{dt}\left(\frac{3}{2}N_eT_e\right) = -\frac{E_i}{Z}\frac{dN_e}{dt} \qquad \Rightarrow \qquad T_e = \frac{N_{e0}}{N_e}\left(T_{e0} + \frac{2}{3}\frac{E_i}{Z}\right) - \frac{2}{3}\frac{E_i}{Z} \qquad (29.3)$$

From Eq.(3) follows that while N_e rises in time T_e decreases. We approximate the ionization rate with a linear function of T_e determined in terms of initial temperature T_{e0} and some final temperature T_{e1} ($T_{e1} < T_{e0}$):

$$\langle\sigma_i\upsilon_e\rangle = \langle\sigma_i\upsilon_e\rangle_{Te0} + \frac{\langle\sigma_i\upsilon_e\rangle_{Te1} - \langle\sigma_i\upsilon_e\rangle_{Te0}}{T_{e1} - T_{e0}}(T_e - T_{e0}) \qquad (29.4)$$

In particular, at $T_e < E_i$ the ionization rate becomes exponentially vanishing function of T_e and can be zeroed at some $T_e = T_{ethr}$ (the ionization threshold). In such case, choosing T_{ethr} as T_{e1}, we get

$$\langle\sigma_i\upsilon_e\rangle = \langle\sigma_i\upsilon_e\rangle_{Te0}\frac{\eta(T_e - T_{ethr})}{T_{e0} - T_{ethr}} \qquad (29.5)$$

Below we take care of keeping T_e in the range (T_{e1}, T_{e0}) and $N > 0$ thus omit η from formulas.

Substituting T_e Eq.(3)$_2$ into Eq.(4) and $\langle\sigma_i\upsilon_e\rangle$ Eq.(4) into Eq.(1), and integrating gets

$$\frac{N_e - N_{e0}}{N_0} = Za_e(1 - \exp(-b_eY)), \qquad Y = \int_0^t \frac{N}{N_0}dt \qquad (29.6)$$

$$a_e = \frac{N_{e0}}{N_0}\frac{1}{g}, \qquad b_e = \langle \sigma_i \upsilon_e \rangle_{Te0} \frac{N_0}{V} g \qquad (29.7)$$

$$g = \frac{1-q}{1-s}\left(\frac{2}{3}\frac{E_i}{T_{e0}} + Z\right) - Z, \quad q = \frac{\langle \sigma_i \upsilon_e \rangle_{Te1}}{\langle \sigma_i \upsilon_e \rangle_{Te0}}, \qquad s = \frac{T_{e1}}{T_{e0}} \qquad (29.8)$$

Choosing for instance $T_{e1} = (2/3)E_i$ and $q = 0$ (ionization threshold in rough approximation) results in $g = (Z+1)/(A-1)$, with $A = (3/2)T_{e0}/E_i > 1$. We assume $s < 1$ but q can get larger than 1 and in this case the exponent in Eq.(6) will be rising in time. As a_e becomes negative, N_e remains increasing.

Eq.(2) becomes the equation for dY/dt:

$$\frac{dY}{dt} = 1 - a_e\left(1 - \exp(-b_e Y)\right), \qquad Y|_{t=0} = 0 \qquad (29.9)$$

It is to note that Eq.(9) permits analytical solution. However, as the ionization is implemented in the integration modelling with a poor feasible accuracy, the following way is chosen aiming at avoiding accuracy overestimation and further work in a complicated numerical environment. If we have $b_e > 0$, the exponent in Eq.(6) is linearly approximated but fixing the whole *rhs* at large Y:

$$1 - \exp(-b_e Y) \rightarrow \begin{bmatrix} b_e Y, & b_e Y < 1 \\ 1, & b_e Y \geq 1 \end{bmatrix}, \qquad (b_e > 0) \qquad (29.10)$$

At $b_e < 0$ the linear approximation at small Y is also employed, but at $|b_e|Y$ reaching some acceptable value ε the calculation is assumed limited by the time interval at which $|b_e|Y < \varepsilon$ remains. The same limitation can also be applied in case of $b_e > 0$ if increased accuracy is required.

The integration of Eq.(9) uses Y as independent variable on the interval bounded by the value $Y_1 = 1/b_e$ ($b_e > 0$) or $Y_1 = \varepsilon/|b_e|$ ($b_e < 0$). At $Y < Y_1$ the *rhs* Eq.(9) linearly rises with time:

$$\frac{dY}{dt} = 1 - SY, \qquad Y|_{t=0} = 0, \qquad S = a_e b_e \qquad (29.11)$$

We obtain $Y(t)$ as

$$Y = \frac{1 - \exp(-St)}{S}, \qquad (Y_0 \leq Y < Y_1) \qquad (29.12)$$

If at the required interaction time $t = \tau$ the obtained Y did not reach the limit Y_1, the results for $t = \tau$ get available in accordance with Eq.(12), Eq.(6) and Eq.(2) (in Eq.(6) the approximation Eq.(10) must be applied). If we got $Y(\tau) > Y_1$, the time interval corresponding Y_1 is calculated:

$$t_1 = -\frac{1}{S}\ln(1 - SY_1) \tag{29.13}$$

The calculation is stopped returning the results for $t = t_1$ ($t_1 < \tau$) If $b_e > 0$, these results correspond in fact to the moment $t = \tau$, because N and N_e keep constant at $t > t_1$, which follows from Eq.(9) having acquired the form $N/N_0 = 1 - a_e$.

The requirement $T_e > T_{e1}$ can also limit the time interval. Combining Eq.(3)$_2$ and Eq.(6) we write this requirement as the last alternative for Y_1.

$$Y_1' = \frac{T_{e0} - T_{e1}}{ZT_{e1} + (2/3)E_i} \frac{N_{e0}}{N_0} \frac{1}{a_e b_e} \tag{29.14}$$

To test this formula, the condition $Y < Y_1'$ is compared with the condition $b_e Y < 1$ for the mentioned case of rough ionization threshold, which resulted in $b_e Y_1' = 1$ thus confirming that the calculations are correct.

Part VI   Vessel wall processes

30. Simulation of sputtering and vaporization at the wall

So far, in TOKES only the physical sputtering is implemented, simulating the emission of surface atoms due to the impacts of energetic particles. In theory we follow the review Ref.[30], in particular the backscattering of impacting atoms is also implemented using the formulas mentioned on p.98 there. An impacted target atom can leave the surface if its energy exceeds the surface binding energy E_S, which is close to the sublimation energy (E_S decreases with increasing target temperature). The most important sputtering parameter is the sputtering yield Y, which is averaged number of emitted atoms per one incident particle; Y depends on the incident energies E and it seems obvious that $Y = 0$ at $E < E_S$.

For most important wall materials to be used in ITER, which are beryllium, graphite and tungsten, TOKES uses the experimental dependences $Y(E)$ from Ref.[31]. If some of needed sputtering data is not available there, an analytical model of physical sputtering Ref.[32] is used. The following formula for the normal incidence is implemented:

$$Y(E)\big|_{\text{norm}} = Q_y s_n \left(1 - \left(\frac{E_{th}}{E}\right)^{2/3}\right)\left(1 - \frac{E_{th}}{E}\right) \qquad (Y = 0 \text{ at } E < E_{th}) \qquad (30.1)$$

Here s_n is the nuclear stopping cross-section and E_{th} the sputtering threshold energy. The fitting parameter Q_y is to be specified for each particular pair (1,2) where the index 1 stays for the incident particle and 2 for the target material atoms. From Eq.(1), $Y \propto (E - E_{th})^2$ at $E \to +E_{th}$ follows. The following expressions for s_n and E_{th} are used:

$$s_n(\varepsilon) = \frac{\ln(1 + 1.2\varepsilon)}{2\varepsilon + 0.34\sqrt{\varepsilon} + 0.016\varepsilon^{0.15}} \qquad (30.2)$$

$$E_{th} = E_S \times \left[\begin{array}{ll} \gamma_k^{-1}(1 - \gamma_k)^{-1}, & m_2 \geq 5m_1 \\ 8(m_1/m_2)^{2/5}, & m_2 < 5m_1 \end{array}\right. \qquad (30.3)$$

The parameter $\varepsilon = E/E_{TF}$. The parameter γ_k and the 'Thomas-Fermi' energy E_{TF} are given by

$$\gamma_k = \frac{4m_1 m_2}{(m_1 + m_2)^2}, \qquad E_{TF} = 1.13\frac{e^2}{r_B}\left(1 + \frac{m_1}{m_2}\right)z_1 z_2 \sqrt{z_1^{2/3} + z_2^{2/3}} \qquad (30.4)$$

The parameters z_1, m_1 and z_2, m_2 are the charge states and the masses of incident and target atom, respectively. Table 1 gives the binding energies E_S and the parameter Q_y for some target atoms and incident atoms (the figures in braces are commented below in the text):

Table 30.1 Binding energies for incident − target atomic pairs

Target material atom:		Be	C	W
	E_S [eV]:	3.38	7.42	8.68
Incident atom	*H/D/T*	0.07/0.11/0.14	0.05/0.08/0.1	0.04/0.07/0.1
	He	0.28 (0.5)	0.2	0.2
	Self-sputtering	0.67	0.75 (2.5)	33
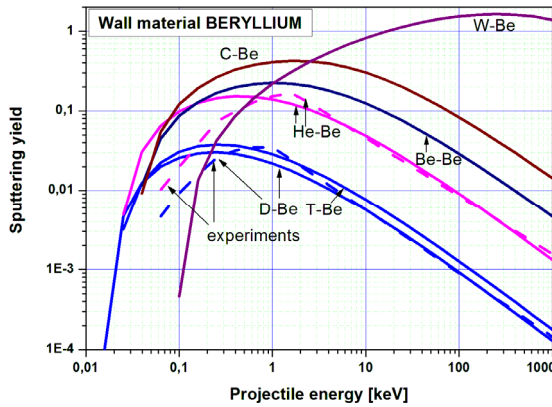
Fig. 30.1 Sputtering yields for Be target
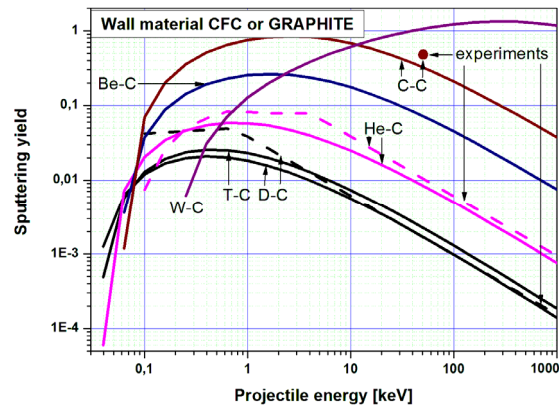
Fig. 30.2 Sputtering yields for carbon based target materials
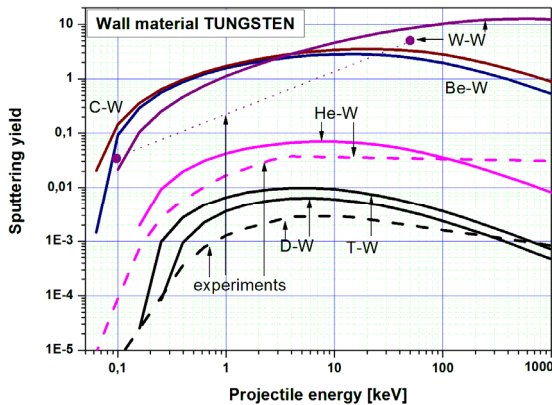
Fig. 30.3 Sputtering yields Y for the target material tungsten.

After some minor modifications this data is used in TOKES for simulations of consequences of ELM impacts below the vaporization threshold Ref.[29]. The resulting sputtering yields Y are shown in Fig.1, Fig.2 and Fig.3. In cases when the experimental data is available, it is used in the range of availability. Outside the range the logarithm of Y is approximated linearly, trying to fit the analytical dependences at the projectile energy $E = 1$ MeV. The Q_y was sometimes modified to approach the available experimental information as seems reasonable.

Those modifications of Q_y concerned the cases D-W ($Q_y = 0.02$), D-W ($Q_y = 0.03$) and the values of Q_y in the braces of Table 1, which are those finally used. For the other cases not

mentioned in Table 1 (in which other chemical elements than the mentioned ones participate in the interactions), $Q_y = (z_1/z_2)^{1/2}$ is used. (In Fig.3 the dotted line that connects two available experimental points for W does not present information, serving only for plot interpretation.)

The vaporization is implemented following Ref.[11]. The vaporized number N_{vap} of material atoms per unit area of the surface during time step τ is calculated using data Ref.[33] on saturated vapour pressure $p_{sat}(T_s)$ as a function of surface temperature T_s (the calculation of T_s is considered in Sec.31). We have $N_{vap} = \frac{1}{4} n_{vap} \upsilon_T \tau$, with the surface vapour density $n_{vap} = p_{sat}/T_s$ and averaged velocity of vaporized atoms $\upsilon_T = (8T/\pi m)^{1/2}$. As p_{sat} depends strongly on T_s, at the end of time step the drop of T_s would drastically decrease N_{vap}, which after the next time step can cause very large N_{vap}. To overcome this numerical instability, a simplified energy balance equation for only the first few meshes is solved before each time step in order to adjust T_s and N_{vap} to each other, assuming the same temperature T_s of these meshes. The vaporized atoms are emitted with the energy $(5/2)T_s$.

The numbers N_a and energies E_a of the atoms to be emitted from each wall segment are in advance accumulated as data pairs $(N_a, N_a E_a)$, separately for the scattered, sputtered and vaporized atoms. When N_a exceeds some given minimum value, or the accumulation period exceeds some given maximum time, the next ray of N_a atoms in the ground state of their bound electrons and with kinetic energy E_a per atom is produced. The corresponding data pair is then zeroed, and a new accumulation cycle starts. After many emissions the half-isotropic ray's distribution is achieved at each wall segment. The values of N_a and $N_a E_a$ should be as small as available computer speed allows (presently $N_a = 10^{17}$ and $N_a E_a = 1$ J are chosen).

31. Wall heat transport

One important process in the vessel wall is the thermal conduction of the plasma heat and the radiation load through the armour material to some cooling equipment in wall bulk. In TOKES this process is simulated with one-dimensional thermal conductivity equation for the wall bulk temperature T (as in Ref.[11]):

$$c \frac{\partial T}{\partial t} = \frac{\partial}{\partial x}\left(k \frac{\partial T}{\partial x}\right) + Q, \qquad k \frac{\partial T}{\partial x}\bigg|_{x=0} = -q_0, \qquad T(x_c) = T_c \qquad (31.1)$$

Introducing the coordinate x into the depth of the wall, with $x = 0$ at the vessel surface, we assume fixed temperature T_c at the cooling equipment situated at some $x = x_c > 0$ in the bulk. The heat capacity c and the thermal conductivity k of wall material are some given functions

of T. The volumetric heating term Q in Eq.(1) foresees that some part of wall load energy can penetrate into depth in some other way (not by the heat conduction, for example due to stopping of runaway electrons in the material). The other part of load is applied as the surface heat flux q_0, which describes Eq.(1)$_2$. We have $q_0 = (Q_w - N_{vap} E_{subl})/\tau S$, where Q_w is the impacting plasma energy, N_{vap} the number of wall material atoms vaporized during the time step τ, E_{subl} the sublimation energy and S the area of the surface segment.

The problem Eq.(1) is numerically solved approximating the equation by the finite-difference scheme for some number I of numerical cells separated at some coordinates x_i. The approximation equations for the scheme index $i = 1..I-1$ and the boundary equations read:

$$c_i \frac{T_i - \hat{T}_i}{\tau} = \frac{1}{x_{i+1} - x_i}\left((k_i + k_{i+1})\frac{T_{i+1} - T_i}{x_{i+2} - x_i} - (k_{i-1} + k_i)\frac{T_i - T_{i-1}}{x_{i+1} - x_{i-1}} \right) + Q_i, \qquad (31.2)$$

$$(k_0 + k_1)\frac{T_1 - T_0}{x_2 - x_0} = -q_0, \qquad\qquad T_I = T_c \qquad (31.3)$$

Eq.(2) and Eq.(3) satisfy the energy conservation sum:

$$\sum_{i=1}^{I-1} c_i (T_i - \hat{T}_i)(x_{i+1} - x_i) = \tau(q_0 - q_c) + \tau\sum_{i=1}^{I-1} Q_i (x_{i+1} - x_i) \qquad (31.4)$$

$$q_c = -(k_{I-1} + k_I)\frac{T_I - T_{I-1}}{x_{I+1} - x_{I-1}} \qquad (31.5)$$

The heat flux q_c into the cooling system is calculated at each time step after solving the system Eq.(2) and Eq.(3). The same diffusion algorithm that TOKES applied for plasma cross-transport is used (see Sec.11). The three-diagonal matrix equations read:

$$-A_i T_{i-1} + (B_i + A_i + C_i)T_i - C_i T_{i+1} = F_i, \qquad\qquad i = 0..I \qquad (31.6)$$

The coefficients follow as

$$A_0 = 0, \qquad B_0 = 0, \qquad C_0 = k_0 + k_1, \quad F_0 = q_0(x_2 - x_0) \qquad (31.7)$$

$$A_i = \tau\frac{k_{i-1} + k_i}{x_{i+1} - x_{i-1}}, \qquad B_i = c_i(x_{i+1} - x_i), \qquad C_i = \tau\frac{k_i + k_{i+1}}{x_{i+2} - x_i} \qquad (31.8)$$

$$F_i = c_i \hat{T}_i (x_{i+1} - x_i) + \tau Q_i (x_{i+1} - x_i), \qquad (i = 1..I-1) \qquad (31.9)$$

$$A_I = 0, \qquad B_I = 1, \qquad C_I = 0, \qquad F_I = T_c \qquad (31.10)$$

Usually we work with $x_c = 4$ cm and $I = 20$. The discrete coordinate x_i is assigned very close values near the surface and rather rare values near the cooling system: the cell sizes $\Delta x_i = x_{i+1} - x_i$ increase as geometrical progression from 15 µm at $x = 0$ up to 1.2 cm at $x = x_c$.
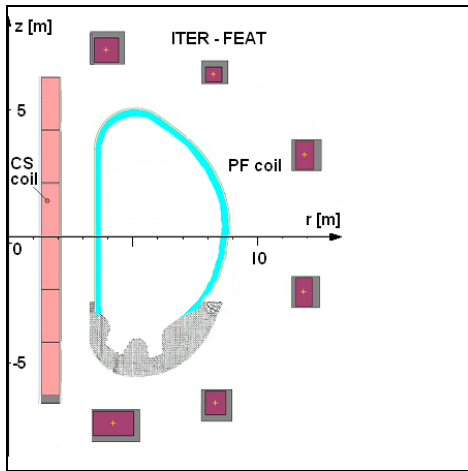
32. How to start working with TOKES

Fig. 32.1 Layout of tokamak ITER

The work with TOKES starts after you draw some design of poloidal cross-section of a tokamak configuration in a bitmap file, like that shown in Fig.1. To do this, some conventional graphical tool which is available on your computer can be used. The sizes (in pixels) of the bitmap file are restricted (in the current version of TOKES as 450×450), which is equal to the layout image sizes on the TOKES window on the computer display (that graphical image occupies only a part of TOKES window). That image can show different pictures you dynamically choose to be produced by the code being updated after each time step of running simulation.

The left-bottom (r_{min},z_{min}) and right-top (r_{max},z_{max}) corner positions that correspond to the image corners should be chosen (in meters) so that the width and the height of the rectangle are equal: $z_{max} - z_{min} = r_{max} - r_{min}$, and you write this data into the special initial file 'Start.txt' as the data line 'Layout sizes'. PF coils data are saved in advance in another text file the name of which is also mentioned in the text of the start-file. Some other data files should also be available, for instance some data containing information about plasma and neutral species, and neutral beams data. Such auxiliary files are, like the start-file, some texts that can be created with the names you prefer and modified using any available plain text editor. The start-file can also have arbitrary name (the name Start.txt is the default name).
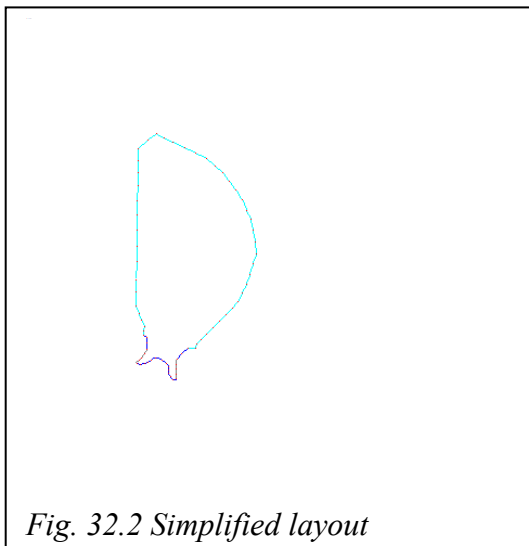
Fig. 32.2 Simplified layout

In the simulations with calculation of PF coil currents, the coils are seen on the image like in Fig.1, and the coil positions can determine the physical sizes of the square. Without the current calculation, TOKES does not show the coils, which allow a significant magnification of the vessel image, also as you choose. Thus you write into the start-file both sets of corner positions.

It seems reasonable to have a copy of the design bitmap, and you are not required to draw many details. For example it would be completely

sufficient to draw only the vessel surface poloidal projection (see Fig.2). The surface contour should then be marked with a number of points using some unique colours, in order to provide the recognition of the surface contour by TOKES' automatic scanner of the bitmap. You choose those marking colours as you want, excepting the black colour, and at first assign with the unique colours several left-top pixels of the bitmap (the pixels (i,j) = (0,0), (0,1), …), as shown in Fig.3 in which two small parts of Fig.2 are shown. (In Fig.2 these pixels, at the left-top corner, are hardly seen.) The pixel (0,0) represents the colour of triangle mesh nodes that will lay on the surface, and you decide now how they will do. The following several pixels (in Fig.3 three ones: (0,1), (0,2), and (0,3)) represent the colours of different wall materials (meaning e.g. Be, C and W). The last pixel of this array must be the black colour, which the scanner recognises as the end of the sequence of unique colours, and thus by this way TOKES gets from you the number of different wall materials.

Fig 32.3 Marking of surface

Then you mark the surface contour itself (with the unique colours) like that of Fig.3. The correspondingly coloured lines that connect the nodes of surface contour segments provide the code with the information about the locations of the wall materials. From this bitmap file the code gets the information about the shape of vessel surface. The surface contour can be arbitrary, being limited only by the requirement of topological identity to the circle. As to the chemical elements of the wall materials, they are not specified here. However, their specification (in the start-file) should be compatible with the number of wall materials of the bitmap file. It is to note that the surface is recognized as a counter-clockwise oriented contour. The surface segment nodes are indexed starting from zero at the node position before which one pixel of wall material should be 'missed' (find it in Fig.3).

Then you submit the code in order to produce a file that should contain the vessel surface information in textual format, for future use without the bitmap file. To do that, after the TOKES window appeared at the display, you may read some notices about the work with the code, after which click on the button "Task", which enables to browse for the start-file. The start-file contains preliminary input data for the next calculation. We assume that some of required files are already available (at least the start-file itself and the bitmap file, e.g. Start.txt

and Layout.bmp). The start-file contains the diverse options (see Fig.4) together with some short comments for them.

The contents of Start.txt can be immediately edited in the TOKES window, for instance updating the layout corners data, and then one clicks the button "Start". The code loads data mentioned in Start.txt and gets ready for some jobs. The work with TOKES begins sequentially creating the text files mentioned in Start.txt as the data "Boundary", "Triangle grid", "Plasma toroidal currents" and "Magnetic layers". At each step the data indicated in Start.txt are used as soon as they become available. Further work does not repeat these steps.
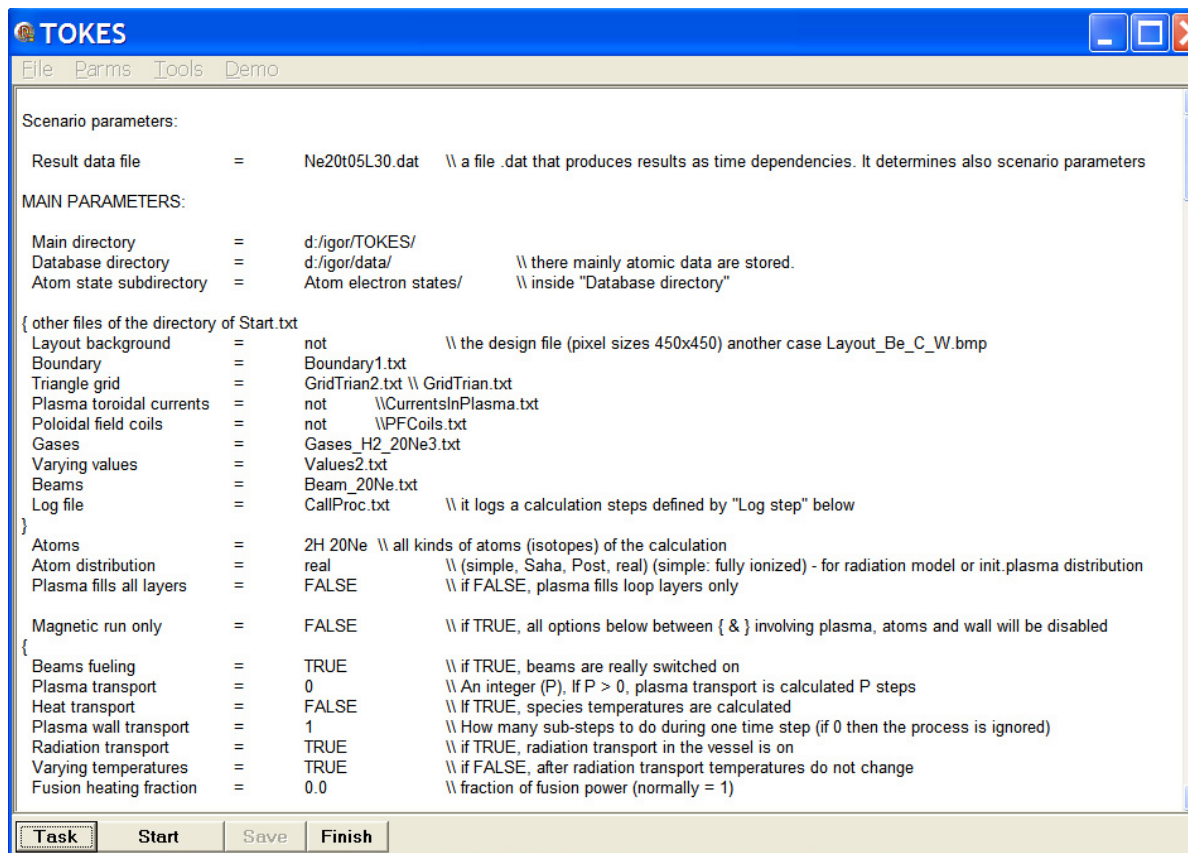

Fig. 32.4 Initial part of the file Start.txt

In the main menu item "Tools" on TOKES panel you see the option "Vessel surface". Click it and you get the opportunity to pick up the mentioned marked bitmap. (If the bitmap file is not available or you would like to produce a default tokamak configuration, simply refuse from picking up the file, and then TOKES suggests you to produce a default tokamak boundary.) The bitmap file will be read, the boundary created as some internal data structure of the code, and the textual information saved in some text file (choose its name when TOKES will ask you about) as a sequence of physical coordinates (in m) of marked points. In that file some information about the wall materials will also be saved (to see the details, look into the file). You should then leave TOKES clicking the button "Finish". Then submit

TOKES again, assign the "Boundary" line the name of the file produced, and afterwards make the next step as follows.

Click "Tools/Triangle grid" in order to produce the corresponding data using a boundary contour. To make operation with TOKES more flexible, the bitmap file will be requested, but you may ignore this request, which (after the question 'Continue?') loads the "Boundary" file specified in the Start.txt. The grid will be automatically produced and saved in a text file of your choice in a special format. Then again leave and submit TOKES, and assign the "Triangle grid" with the name of that file. It is to note that sometimes it is better to prepare a simple triangle grid file manually, as it is described in the end of this section.

The next step is the generation of a file that contains some preliminary 'plasma currents' (despite of the fact that you didn't create the plasma yet). The preliminary currents are toroidal currents through the triangle centres. They are necessary for calculation of initial magnetic field and thus for building magnetic layers and then the plasma before starting some tokamak simulation. The triangle's preliminary currents are equally proportional to their triangle area, inversely proportional to the triangle's centre radius r, and in addition the currents contain some decreasing Gaussian factor, depending on the triangle centre's distance to some 'centre' of the vessel surface poloidal cross-section (TOKES itself calculates the domain centre). The full preliminary current (the sum of the triangle's currents) is normalized to the value of the total current. The total current (e.g. 15 MA) is assigned in the Start.txt (the "Plasma current" line). To produce the initial plasma currents, click "Tools/Plasma currents" and the current file will be produced 'as usually'. (Don't forget afterwards to assign the 'Plasma toroidal currents' line with the name of the produced file.)

The magnetic layers are also produced in the 'semi-automatic' way, using the plasma currents and arbitrary coil currents and the triangle grid. By the way, you may, with already produced layers, immediately update the currents. Simply use again the option "Plasma currents" and the currents will be updated in the following way: the whole current remains equal to the "Plasma current" assigned in the Start.txt, but the current density becomes constant over the looped magnetic layers and equal to zero on the layers ending at the surface. The resulting currents remain be prescribed to the triangles' centres.

On the opened layers the plasma density will be small in comparison with that on the closed layers, but TOKES calculates it as well. In each layer (for plasma) or triangle (for neutrals) the densities n_g and temperatures T_g of species ($g = i$, n and e, i.e. ions, neutrals and electrons) are constant. An ions species is described with the symbol <atomic

weight><chemical symbol><charge state>, for instance 4He1 (helium four once charged ions). For neutrals, <charge state> is omitted. For electrons the symbol "eln" is employed.

It is assumed that the densities and temperatures of plasma species are initially constant over the vessel, and this simple set of values of n_g [m^{-3}] and T_g [eV] is assigned in the file named in the "Gases" line of the file Start.txt. The electrons must be the first 'gas' in that file. Electron density is in fact not used, being calculated from ion densities and charge states (plasma quasineutrality is assumed). Therefore initially it doesn't matter what electron density is assigned. The electron density can however be of interest when such file is produced in the calculations. Therefore for each magnetic layer, the plasma file of the code contains after the calculation all temperatures T_g and all densities, which are n_e and the populations n_{mzk}, for the ion species m, accounted ion charge states z and electron levels k.

Manual preparation of triangle grid: Sometimes, e.g. for testing with a trivial boundary, we prefer to construct the triangle grid manually (without using the grid generator of TOKES as it is mentioned). To create the grid file manually, we may use as an example some already available file of triangle grid data, or the following example for the boundary in form of a box Fig.5. The contents of corresponding grid file are shown in Fig.6 (omitting for shortening the field "Value" that follows in the file the field "Position" in each TPeak). The grid nodes („peaks") at the boundary are indexed by 0, 1, 2, 3 and that at the centre by 4. Their (r,z)-positions [m] are determined in t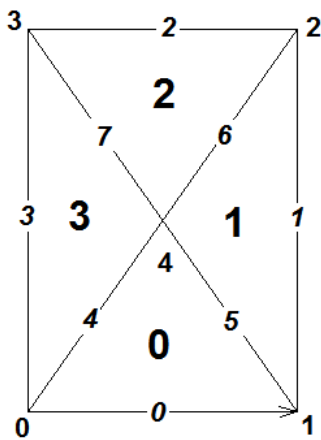he file. The sides of triangles are indexed from 0 to 7, and four triangles are indicated in Fig.5 with the large digits. A side by the sequence of peak indices in the line "Peak = (a,b)" (a → b). The next line "Wing" is arbitrarily oriented (like an arrow) from its one peak (a) to another (b), which determines two neighbouring triangles of the side: 1st triangle from the left and 2nd triangle from the right in respect to the side (1st ↑ 2nd). For 'not-existing triangles' outside the grid the name 'nil' is used.

Fig. 32.5 Simple triangle meshes

```
TTrianMesh 0:
Peaks number = 5
Sides number = 8
Trians number = 4
TPeak 0:
Position = ( 4.0 -
2.0)
TPeak 1:
Position = ( 6.0 -
2.0)
TPeak 2:
Position = ( 6.0  2.0)
TPeak 3:
Position = ( 4.0  2.0)
TPeak 4:
Position = ( 5.0  0.0)
TSide 0:
Peak = (0 1)
Wing = (0 nil)
TSide 1:
Peak = (1 2)
Wing = (1 nil)
TSide 2:
Peak = (2 3)
Wing = (2 nil)
TSide 3:
Peak = (3 0)
Wing = (3 nil)
TSide 4:
Peak = (0 4)
Wing = (3 0)
TSide 5:
Peak = (1 4)
Wing = (0 1)
TSide 6:
Peak = (2 4)
Wing = (1 2)
TSide 7:
Peak = (3 4)
Wing = (2 3)
TTrian 0:
Side = (0 5 4)
TTrian 1:
Side = (1 6 5)
TTrian 2:
Side = (2 7 6)
TTrian 3:
Side = (3 4 7)
```

Fig. 32.6

33. Conclusions

Recently developed integrated tokamak code TOKES is described. The code can simulate different tokamak processes as with nominal time step of a few ms as with small time step suitable for ELMs. Different plasma and vessel surface shapes can be simulated. The magnetic field can evolve together with the confined plasma and electric currents updated after each time step. Poloidal field coils can automatically control plasma shape. The Pfirsch-Schlüter multi-fluid plasma model with charge state grouping for ion species and the gyro-Bohm cross-transport is implemented. In the confined region, the fluids are from hydrogen isotopes to tungsten multi-charged ions of grouped bound electron excitation states. This allowed full radiation transport model that includes calculations of level populations. The fluxes of neutrals (atoms, neutrons and photons) propagating through the vessel are simulated with toroidally symmetric big particles ('rays') that are coupled with the plasma. The coupling is achieved by building the magnetic surfaces on toroidal cells with triangular cross-sections in the whole vessel volume. The SOL transport is implemented based on the guiding centre model for the magnetized ions. The Monte-Carlo technique for propagation of the rays and the gyro-particles is applied. The main wall processes including surface sputtering and evaporation as well as bulk heat transport are also implemented. The code allows controlled fusion power and feedbacks on the beam heating. By this, TOKES acquired major features necessary for tokamak modelling.

However, plasma transport modelling can be improved. In particular, the thermoforce contributions should be implemented. The SOL modelling is in rather preliminary state: non-complete ionization in SOL is not available and plasma temperature is prescribed to the fully ionized ions, so that the difference between the temperatures of ions and electrons in SOL is not accounted for. The radiation-population model is developed only for the confined plasma. The radiation losses from SOL are not available. In the regime with evolving magnetic field, there is no automatic feedback for keeping the confinement in the window of MHD stability. Only the neutral beam heating is implemented, there is no the RF heating yet.

Therefore TOKES cannot yet be introduced as some finished integrated tokamak code. Its capabilities are not yet acquired mature stage. More work is needed for further development of the code in order to reach reliable integrated modelling. In particular, TOKES needs validations, which can demand significant elaborations of some its models.

Acknowledgements

References

1. G.V. Pereversev et al., ASTRA: Rep. IPP 5/42, Max-Planck-Institute für Plasmaphysik, Garching (1991)

2. I.S. Landman, G. Janeschitz, Contamination and radiation losses in post-ELM tokamak plasma, 32nd EPS, Tarragona, Spain, June 27 – July 1 (2005) CD, ECA, V.29C, P1.003, http://eps2005.ciemat.es/papers/pdf/P1_003.pdf

3. I.S. Landman, G. Janeschitz, Modelling of SOL transport and radiation losses for ITER with the integrated tokamak code TOKES, J. Nucl. Mater. 390–391 (2009) 384

4. L.A. Artsimovish, Tokamak devices, Nucl. Fusion 12 (1972) 215

5. V.D. Shafranov, in Reviews of Plasma Physics, Vol. 2 (Consultants Bureau, New York, 1966)

6. L.D Landau, E.M. Lifshitz, Course of theoretical physics, Vol. 8, (Oxford u.a. Butterworth-Heinemann, 2000)

7. S.I. Braginskij, in Reviews of Plasma Physics, Vol. 1 (Consultants Bureau, New York, 1965)

8. J. Wesson, Tokamaks, third ed., International Series of Monographs on Physics, Clarendon Press, Oxford, 2004

9. A.A. Galeev, R.Z. Sagdeev, JETP 26 (1968) 223

10. I.S. Landman, G. Janeschitz, Plasma transport modelling with multiple-mapping magnetic surfaces. 33rd EPS, Rome, Italy, June 19-23 (2006) CD, ECA, V. 30I, P5.165

11. I.S. Landman, G. Janeschitz, Numerical simulations of plasma wall interactions for ITER, J. Nucl. Mater. 363 (2007) 1061

12. I.S. Landman, G. Janeschitz, Calculation of poloidal magnetic field in tokamak code TOKES, 35th EPS, Hersonissos, Crete, Greece, June 9-13 (2008) CD, ECA, V.32D, P5.057

13. R. Kochergov, I.S. Landman, G. Janeschitz, "Implementation of plasma diffusion models in the code TOKES", 33rd EPS, Rome, Italy, June 19-23 (2006) CD, ECA, V. 30I, P5.166

14. I.S. Landman, G. Janeschitz, Plasma convection in ITER integrated modelling with the code TOKES, 34th EPS, Warszawa, Poland, July 2-6 (2007) CD, ECA, V. 31F, P4.116

15. G.A. Korn, T.M. Korn, Mathematical handbook for scientists and engineers, 2nd edition, p. 788 (McCraw-Hill Book Company, 1968)

16. S. Pestchanyi, I. Landman, ELM induced carbon contamination of ITER core, J. Nucl. Mater. 363-365 (2007) 1081

17. S. Pestchanyi, I. Landman, Experimental verification of FOREV-2D simulations for the plasma shield, J. Nucl. Mater. 390–391 (2009) 822

18. I.S. Landman, G. Janeschitz, Modelling of radiation impact on ITER beryllium wall, J. Nucl. Mater. 386–388 (2009) 915–918

19. D.L. Book, NRL Plasma Formulary (Revised edition, 1990, Washington, DC 20375)

20. D.E. Post et al., Atomic Data and Nuclear Data Tables, 20 (1977) 397

21. W.L. Wiese et al., Atomic Transition Probabilities, Vol. 1, NSRDS-NBS 4 (1966)

22. A. Burgess, Astrophys. J. 141 (1965) 1588

23. H.R. Griem, Radiation processes in plasmas, Handbook of plasma physics, Eds. M.N. Rosenbluth and R.Z. Sagdeev, V.1 (1983) 73

24. B.A. Trubnikov, in Reviews of Plasma Physics, Vol. 7 (1979) 345

25. N. Carlson et al., Atomic data 2 (1970) 64.

26. [Ralchenko] Yu. Ralchenko et al. NIST Atomic Spectra Database: http://physics.nist.gov/asd3.

27. K.P. Dere, Ionization rate coefficients for the elements hydrogen through zinc, Astronomy and Astrophysics (A&A), 466 (2007) 771

28. R.B. White, The theory of toroidally confined plasmas (Imperial College Press, 2006)

29. I.S. Landman, G. Janeschitz, Contamination of ITER core by impurities of tungsten and carbon, Fus. Eng. Des. 83 (2008), 1797

30. D. Naujoks, Plasma-Material Interaction in Controlled Fusion (Springer Series on atomic, optical, and plasma physics, Springer-Verlag, Berlin, Heidelberg, 2006)

31. H.H. Andersen, H.L. Bay, Sputtering Yield Measurements, Topics in Applied Physics Vol. 47 (Springer-Verlag, 1981)

32. P. Sigmund, Sputtering by Ion Bombardment: Theoretical concepts, Topics in Applied Physics Vol. 47 (Springer-Verlag, 1981)

33. B.N. Bazylev et al. Fus. Eng. Des. 75-79 (2005) 407